

**TURBOMACHINERY CASCADE AND WAKE CALCULATION FOR TWO-DIMENSIONAL
COMPRESSIBLE LAMINAR AND TURBULENT FLOW**

by

Gerald J. Micklow

Dissertation submitted to the Faculty of the
Virginia Polytechnic Institute and State University
in partial fulfillment of the requirements for the degree of

DOCTOR OF PHILOSOPHY

in

Mechanical Engineering

Approved:

W. F. O'Brien, Chairman

J. Moore

H. L. Moses

E. F. Brown

G. W. Swift

June 1989

Blacksburg, Virginia

**TURBOMACHINERY CASCADE AND WAKE CALCULATION FOR TWO-DIMENSIONAL
COMPRESSIBLE LAMINAR AND TURBULENT FLOW**

by

Gerald J. Micklow

ABSTRACT

A method is presented for the efficient analytical prediction of the two dimensional laminar or turbulent compressor or turbine cascade blade-to-blade flow field and wake. The scheme utilizes a viscous-inviscid interaction routine combining a two-dimensional full potential cascade flow solver with a two-dimensional compressible boundary layer analysis. The boundary layer analysis can compute in the direct mode with pressure gradient specified or in the inverse mode with "boundary layer mass flux" specified. When calculating with the inverse mode, flow separation can be handled easily. Turbulent flow is treated using an algebraic eddy viscosity model with the modified Levy-Lees transformation applied to capture the growth of laminar and turbulent boundary layers. The boundary layer solution is fully implicit and formally second order accurate. The viscous inviscid coupling is performed utilizing thin airfoil theory. Numerical solutions are presented for several numerical test cases and compared with published test data.

ACKNOWLEDGMENTS

I would like to thank Dr. John Moore and Dr. Walter O'Brien for their help and guidance over the past five years. I would also like to thank Dr. G. W. Swift for his help in the code development and for his help and instruction in his classes in computational fluid dynamics. I would also like to thank Dr. Hal Moses for his help and suggestions in the development of the boundary layer analysis. And last but not least, I would like to thank _____ for her help in preparing this manuscript and her support over the past six years. She is by far the best secretary that I have ever met.

TABLE OF CONTENTS

	Page
ABSTRACT	ii
LIST OF FIGURES	vi
NOMENCIATURE	x
CHAPTER 1 Introduction	1
CHAPTER 2 Inviscid Flow Field Modelling	12
2.1 Introduction	12
2.2 Two-Dimensional Compressible Potential Flow for Cascades	13
2.2.1 Finite Area Mass Balance and Grid Generation . .	15
2.2.2 Resulting System of Equations and Solution Technique	18
2.2.3 Extension to Transonic Flow	22
2.3 Sample Calculations	24
CHAPTER 3 Viscous Flow Field Modelling	27
3.1 Equations for Laminar and Turbulent Compressible Boundary Layer	27
3.2 Turbulent Transport Models	45
3.2.1 Transition from Laminar to Turbulent Flow	48
3.3 Formulation of the Finite Difference Representation of the Compressible Boundary Layer Equations	49
3.4 Direct Mode Calculation Technique	57
3.5 Inverse Mode Calculation Technique	59
3.5.1 Introduction	59
3.5.2 Calculation Procedure	60
3.6 Viscous-Inviscid Calculation Procedure	68
3.6.1 Introduction	68
3.6.2 Viscous-Inviscid Matching Procedure for Subsonic Flow	69
3.7 Wake Calculation Procedure	75

TABLE OF CONTENTS (continued)

	Page
3.7.1 Turbulence Modeling	75
3.7.2 Calculation Procedure	78
3.8 Sample Calculation	81
CHAPTER 4 Numerical Results and Comparison with Experimental Data	86
4.1 1968 Stanford Conference Data	86
4.2 Flat Plate Symmetric Turbulent Wake Data	86
4.3 Supercritical Cascade Builds 1 and 2	87
CHAPTER 5 Summary and Recommendations	93
CHAPTER 6 Conclusions	96
REFERENCES	97
APPENDIX I Solution of Block Tridiagonal Set of Equations	183

LIST OF FIGURES

Figure		Page
1	Sample Compressor Grid	102
2	Grid Triangulation	103
3	Construction of Mesh Polygons	104
4	Local Grid Construction	105
5	First Upstream Grid Line	106
6	Gostelow Compressor Cascade	107
7	Pressure Coefficient Comparison for Gostelow Cascade	108
8	Hobson Impulse Turbine Cascade	109
9	Mach Number Comparison for Hobson Turbine Cascade	110
10	Korn Compressor Cascade	111
11	Mach Number Comparison for Korn Compressor Cascade	112
12	Eddy Viscosity Regions for Wall and Wake Flows	113
13	Howarth Flow Edge Velocity Profile	114
14	Laminar Flow Velocity Profile for Howarth Flow	115
15	Laminar Flow Velocity Profile for Howarth Flow	116
16	Skin Friction Coefficient for Howarth Flow	117
17	Displacement Thickness for Howarth Flow	118
18	Gostelow Cascade Edge Mach Number	119
19	Gostelow Cascade Turbulent Flow Velocity Profile	120
20	Gostelow Cascade Turbulent Flow Velocity Profile	121
21	Gostelow Cascade Turbulent Flow Velocity Profile	122
22	Gostelow Cascade Turbulent Flow Velocity Profile	123
23	Gostelow Cascade Turbulent Flow Velocity Profile	124
24	Gostelow Cascade Turbulent Flow Velocity Profile	125

LIST OF FIGURES (continued)

Figure		Page
25	Gostelow Cascade Turbulent Flow Velocity Profile	126
26	Gostelow Cascade Turbulent Flow Velocity Profile	127
27	Gostelow Cascade Turbulent Flow Velocity Profile	128
28	Gostelow Cascade Turbulent Flow Velocity Profile	129
29	Gostelow Cascade Displacement Thickness Distribution . .	130
30	Gostelow Cascade Skin Friction Coefficient Distribution	131
31	Gostelow Cascade Edge Mach Number	132
32	Gostelow Cascade Turbulent Flow Velocity Profile	133
33	Gostelow Cascade Turbulent Flow Velocity Profile	134
34	Gostelow Cascade Turbulent Flow Velocity Profile	135
35	Gostelow Cascade Turbulent Flow Velocity Profile	136
36	Gostelow Cascade Turbulent Flow Velocity Profile	137
37	Gostelow Cascade Turbulent Flow Velocity Profile	138
38	Gostelow Cascade Turbulent Flow Velocity Profile	139
39	Gostelow Cascade Skin Friction Coefficient Distribution	140
40	Gostelow Cascade Displacement Thickness Distribution . .	141
41	Gostelow Cascade Wake Edge Mach Number	142
42	Gostelow Cascade Wake Mass Flux Parameter	143
43	Gostelow Cascade Turbulent Flow Wake Velocity Profile .	144
44	Gostelow Cascade Turbulent Flow Wake Velocity Profile .	145
45	Gostelow Cascade Turbulent Flow Wake Velocity Profile .	146
46	Gostelow Cascade Turbulent Flow Wake Velocity Profile .	147
47	Gostelow Cascade Turbulent Flow Wake Velocity Profile .	148

LIST OF FIGURES (continued)

Figure		Page
48	Gostelow Cascade Turbulent Flow Wake Velocity Profile .	149
49	Gostelow Cascade Turbulent Flow Wake Velocity Profile .	150
50	Gostelow Cascade Turbulent Flow Wake Velocity Profile .	151
51	Gostelow Cascade Turbulent Flow Wake Velocity Profile .	152
52	Gostelow Cascade Turbulent Flow Wake Velocity Profile .	153
53	1968 Stanford Conference Skin Friction Data	154
54	Centerline Velocity for Flat Plate Turbulent Wake . . .	155
55	Supercritical Cascade Build 1	156
56	Supercritical Cascade Build 1 Edge Mach Number	157
57	Supercritical Cascade Build 1 Edge Mach Number	158
58	Supercritical Cascade Build 1 Turbulent Velocity Profile	159
59	Supercritical Cascade Build 1 Turbulent Velocity Profile	160
60	Supercritical Cascade Build 1 Turbulent Velocity Profile	161
61	Supercritical Cascade Build 1 Turbulent Velocity Profile	162
62	Supercritical Cascade Build 1 Turbulent Wake Profile . .	163
63	Supercritical Cascade Build 1 Turbulent Wake Profile . .	164
64	Supercritical Cascade Build 1 Turbulent Wake Profile . .	165
65	Supercritical Cascade Build 1 Turbulent Wake Profile . .	166
66	Supercritical Cascade Build 1 Turbulent Wake Profile . .	167
67	Supercritical Cascade Build 1 Turbulent Wake Profile . .	168
68	Supercritical Cascade Build 1 Turbulent Wake Profile . .	169
69	Supercritical Cascade Build 2	170

LIST OF FIGURES (continued)

Figure		Page
70	Supercritical Cascade Build 2 Edge Mach Number	171
71	Supercritical Cascade Build 2 Edge Mach Number	172
72	Supercritical Cascade Build 2 Turbulent Velocity Profile	173
73	Supercritical Cascade Build 2 Turbulent Velocity Profile	174
74	Supercritical Cascade Build 2 Turbulent Velocity Profile	175
75	Supercritical Cascade Build 2 Turbulent Velocity Profile	176
76	Supercritical Cascade Build 2 Turbulent Wake Profile . .	177
77	Supercritical Cascade Build 2 Turbulent Wake Profile . .	178
78	Supercritical Cascade Build 2 Turbulent Wake Profile . .	179
79	Supercritical Cascade Build 2 Turbulent Wake Profile . .	180
80	Supercritical Cascade Build 2 Turbulent Wake Profile . .	181
81	Supercritical Cascade Build 2 Turbulent Wake Profile . .	182

Nomenclature

a_0, a_1, a_2	Interpolating polynomial coefficients
A, B, C	coefficient matrices for finite difference calculations
c	blade chord
C_p	constant pressure specific heat
F	non-dimensional boundary layer streamwise velocity
f	stream function
h	enthalpy
k	thermal conductivity
L	characteristic length
l	mixing length
M	Mach number
Pr	Prandtl number
p	pressure
Q	non-dimensional boundary layer temperature
R	gas constant
r	modified density ratio
Re	Reynolds number
T	temperature
t	time
u	axial velocity
v	tangential velocity
V_1	relative inlet velocity
x	axial coordinate
y	tangential coordinate

Greek symbols

β	pressure gradient
δ	boundary layer thickness
δ^*	displacement thickness
ϵ	turbulent eddy viscosity
ξ	Levy-Lees streamwise coordinate
γ	ratio of the specific heats
λ	bulk viscosity
η	Levy-Lees normal coordinate
ρ	density
ϕ	potential function
τ	shear stress
μ	viscosity
ω	relaxation parameter
χ	artificial compressibility parameter

Subscripts

BL	boundary layer
c	displacement thickness correction
e	boundary layer edge
ep	pressure side wake edge
es	suction side wake edge
i	inner layer
inv	inviscid
o	outer layer
tr	transition
T	total condition

x axial direction derivative
y tangential direction derivative
w wall value
0 initial inviscid value
lp wake centerline property for the pressure side
ls wake centerline property for suction side
 ξ Levy-Lees streamwise derivation
 η Levy-Lees normal derivative

Superscripts

i axial grid point location
n iteration level
* dimensional quantity

CHAPTER 1

Introduction

The accurate prediction of the blade-to-blade flow field and the ensuing blade wake is of paramount importance in the design of advanced axial flow compressors and turbines to insure structural integrity, quiet engine operation and good aerodynamic performance.

It has long been recognized that airfoils arranged in rotating and stationary blade rows in axial flow turbomachinery do not operate in steady flow. From the structural standpoint, the effects of unsteadiness of the flow is of great important with respect to the excitation of blade vibrations and sound generation. It is clear that when the blade rows are closely spaced, the structural performance of the airfoils will be strongly influenced by the blade row interaction of which a major contribution is the blade wake. Modern technology designs, with higher loadings, lower aspect ratios and axial gaps between the blade rows on the order of $1/4$ to $1/2$ of the airfoil chord to minimize overall engine length and weight, will tend to amplify the interaction effects.

The main sources of blade row interaction are as follows:

1. Potential flow interaction
2. Viscous wake from the upstream blade row

The potential flow interactions extend both upstream and downstream of the blade row. The potential flow effects decrease exponentially away from the blade row with a length scale approximately equal to the blade chord.

The viscous wake interaction is of the same order of magnitude as

the potential flow interaction, for small axial gaps between the blade rows. However, as the axial gap increases, the viscous wake interaction far outweighs the potential flow interaction. The potential flow interactions decrease much more rapidly with axial distance than those induced by the viscous wake. The wake interaction can be present several chord lengths downstream of a blade row.

One of the first attempts to analyze the blade row interaction problem was conducted by Sears and Kemp [1]. A linearized incompressible potential flow solution for thin airfoils with small turning was obtained. The analysis showed that for close axial spacing of the blade rows, the unsteady lift could be as much as 18% of the steady value. In a later report [2], the same authors developed a model to consider the viscous wakes separately. It was concluded that for axial gaps typical of those for compressor blade rows, the unsteady forces arising from the viscous wakes are of the same order of magnitude as the potential flow interaction effects. One major restriction to this analysis was the modelling of the viscous wake. The data of Silverstein et al. [3], based on symmetric isolated airfoils, was used. A typical modern compressor or turbine cascade will have a highly asymmetric wake which will have a major influence on the unsteady pressures exhibited on the downstream blade row.

In a more complete work by Kaji and Okazaki [4], compressibility effects were included and both the potential and viscous wake effects were calculated. However, once again the data of Ref. [3] was used for the wake model, imposing a severe restriction on the calculation. The reasoning behind this choice was the sparcity of cascade wake data or models.

Gallus [5,6] performed a number of experiments utilizing a low speed rig to study the interaction between an IGV row, a rotor blade row, and a downstream stator row. The results showed that the fluctuating pressures on the blades due to the potential flow interaction was on the same order of magnitude as the viscous wake interactions for small axial distances between the blade row. For large axial distances, the wake effect would clearly dominate. His studies showed that throttling the flow leads to increasing wake sizes and stronger fluctuation forces. The data showed the wakes to be asymmetric with the slope of the velocity decrease within the wake being steeper on the pressure side. He compared the data with the theoretical predictions of several authors [7,8]. The conclusion was reached that the severest restrictions of the generally valid theory was related to the incompressible flow assumption and the modelling of the viscous wake. Once again the data of Ref. [3] was used as the viscous wake model. Also investigated in these tests was the influence of axial distance and blade number ratio on noise generation. It was seen that the discrete tone levels could be reduced considerably by slight increases in axial gap. This is related to the viscous wake as the shape influences the intensity of various harmonics. Also by choosing suitable blade number ratios, a reduction of discrete blade passing frequency tones could be obtained. Walker [9] carried out an experiment on the effect of blade row interaction on the noise generated in an axial flow compressor. He found that the interaction of the wakes of successive blade rows could be used to reduce the velocity deficiency within the wakes thereby reducing the noise generated by reducing the blade pressure

fluctuations. To utilize this phenomenon in an actual compressor design would require an accurate modelling of the viscous flow field and blade wake.

For good aerodynamic performance and efficient operation of modern axial flow compressors and turbines, accurate total pressure loss coefficients and downstream flow angles must be obtained for the desired operating conditions. Compressor airfoil sections of current production compressor and many advanced compressors are derived from related families of airfoils such as NACA 65 series, the NACA 400 series and the double circular arc series. Extensive plane cascade tests have been conducted on these families of cascade sections, and their performance has been correlated against their specific geometry, Mach number and inlet air angle. The cascade correlations for exit air angle are formulated in terms of a deviation angle from a geometric reference line, such as the trailing-edge mean camber line. The correlations, based on actual compressor test data, are employed in current design systems to accurately predict the performance of compressors using standard airfoil sections.

In recent years, however, to increase overall engine performance, compressor cascade technology has advanced to the point where mathematically defined airfoils are needed to fulfill advanced aerodynamic and structural requirements. These airfoils could possess optimum surface pressure distributions and boundary layer characteristics and other aerodynamic performance superior to the standard airfoil sections currently in use. One very important example of this type of airfoil design is the supercritical cascade airfoil. As the stage

loading increases, which is required to reduce engine weight and increase efficiency, embedded regions of supersonic flow adjacent to the airfoil surface occur even for cascades with subsonic inlet and exit velocities. The term supercritical refers to the presence of velocities in the flow field which are above the "critical" or sonic speed. A major drawback to this type of cascade is that shocks may be present in the flow field. If present, shocks would cause an increase in the total pressure loss coefficient and reduced flow turning. Thus an accurate assessment of the cascade flow field is required to minimize these losses. The supercritical airfoil data acquired to date indicates that the turning angle and profile total pressure loss for these cascades are not accurately predicted by data correlations based on standard series airfoils. To obtain new data correlations for advanced compressor cascades would require a large number of tests and would be excessively expensive. Therefore, it would be of great interest to have available an accurate numerical analysis to predict the blade-to-blade flow field and the viscous wake emanating from the cascade trailing edge line.

Inviscid flow solvers are available, that if modified with boundary layer adjustments to the airfoil surface can closely model the aerodynamics of compressor and turbine cascades except in the trailing edge region. In this region, current cascade flow solvers are inadequate because they do not model the viscous wake. The problem arises because the surface velocity distribution cannot be accurately modelled without accounting for the viscous effects. There is a strong interaction between the viscous and inviscid flow fields which must be taken into account. Also when the wake is not modelled, a stagnation

point not existing in the real viscous flow is computed on the airfoil surface at the trailing edge which affects the pressure distribution over the last 10 to 15 percent chord of the airfoil surface. Current methods used to correct these inaccuracies in the trailing edge flow are based on past experience with standard series airfoils. These methods lack the sound physical basis that would permit their general use for advanced airfoils. If the velocity distribution is not properly calculated, errors in the calculated boundary layer will result, possibly masking flow separation prior to the trailing edge, and leading to large errors in the downstream flow angle and total pressure loss. Therefore, to avoid the excessive cost of testing in advanced compressor designs and to obtain structural integrity, quiet engine operation and efficient aerodynamic performance, an accurate viscous flow solver is required as part of the design system.

To predict the flow field, two approaches may be taken. These solutions consist of solving;

1. Navier-Stokes equations
2. Boundary layer equations with an appropriate inviscid flow model.

The solution of the Navier-Stokes equations has two main advantages over the boundary layer equations. The first is that the Navier-Stokes equations are regular at separation. Second they can handle large separation regions with large reverse flow velocities. However, their solution is very time consuming and therefore expensive to run on the computer. There is approximately an order of magnitude difference in computing time between the solution at the Navier-Stokes equations and

the solution of the boundary layer equations with an appropriate inviscid flow solver. Also the ability to handle large separation regions is of no interest for a well designed compressor or turbine cascade as this condition will not exist in the engine operation range. Further, in contrast to solution methods for the Navier-Stokes equations, numerical errors associated with the solution of the potential flow and boundary layer equations can be rendered very small. In fact, in many cases solutions of the boundary layer equations produce more accurate results than the Navier-Stokes equations as long as the region of separated flow is small or the flow remains attached. In predicting the lift and drag on a GK 75-06-12 airfoil the interactive boundary layer prediction of Melnik et al. [10] produced much more accurate results than the Navier-Stokes procedure of Deiwert [11].

In a prediction of the pressure distribution on a RAE 2822 airfoil operating at an angle of attack of 2.81 degrees, the interactive boundary layer solution of Melnick and Brook [12] produced a closer approximation to the data than the Navier-Stokes solution of Pulliam [13]. An extensive investigation of subsonic flows was performed by Horstman [14] at NASA Ames Research Center. The calculations were performed with a version of the MacCormak program which has been extensively used and is based on an explicit formulation of the two-dimensional form of the Navier-Stokes equations with a predictor-corrector algorithm. The computational facilities allowed the use of 79 x 82 and 134 x 48 grid nodes and the solution domain extended from a position on the body to the equivalent of three chord lengths downstream. Results were compared with an interactive boundary layer

routine and the results showed little difference between the two approaches. A review by Lock [15] indicates the need for an evaluation of numerical accuracy before placing reliance on the solutions of the Navier-Stokes equations and notes that they show larger disagreements with measurements than those of the interactive boundary layer calculations.

Based on the fact that the boundary layer equations require far less computational effort and for flows without massive separation the boundary layer equations produce equivalent, or in some cases better results, in comparison with data than the Navier-Stokes equations, the boundary layer equations were selected as the focus of this study. In terms of viscous wake prediction the most extensive study undertaken to date has been that of Lakshminarayana et al. [16-22]. The analytical modelling of the wake was investigated in both two and three dimensions, for the near and far wake including the effects of curvature, rotation, turbulence characteristics in the wake and freestream turbulence. The assumption of incompressible flow without separation was made in this rather complete analytical study of compressor wakes. The study undertaken here will include both the effects of compressibility and flow separation on a two-dimensional blade-to-blade flow field and the downstream viscous wake.

Typically for high Reynolds number flow, the flow over an airfoil or a blade can be divided into two distinct regions: an inner dissipative region consisting of the boundary layer and wake and the outer inviscid region. The principal interaction arises from displacement thickness effect with small changes in surface pressure.

If this interaction is weak, the viscous effect on the pressure is small and the flow field can be solved in the direct mode whereby the pressure is specified as a boundary condition at the boundary layer edge. However, the flow over a compressor or turbine blade involves both a weak overall interaction from displacement thickness effects and wake curvature effects and local strong interaction effects which occur at a point of separation and at the airfoil trailing edge as the boundary layer experiences an abrupt change in the no slip condition and accelerates into the wake. It has been shown by Goldstein that this will inevitably lead to a singularity at the point of separation [23] causing the breakdown of the numerical method. As an immediate consequence, the conventional direct iterative schemes which are used to account for the interaction of the boundary and the outer inviscid flow cannot be applied when separation is present. Catherall and Mangler [24] were the first to realize that relaxing the pressure would lead to regular solutions of the boundary layer equations. By prescribing the displacement thickness and calculating the pressure, they were able to integrate the boundary layer equations through the separation point and into a region of reverse flow without any evidence of singular behavior at the separation point. This analysis led to other inverse solutions of the boundary layer equations, prescribing either displacement thickness or wall shear [25-28]. A problem associated with the inverse techniques is that the required displacement thickness or wall shear is not known a priori. The appropriate value has to be obtained, as part of the overall problem, from the interaction between the boundary layer and the inviscid flow. The global organization of the direct and

inverse iterative methods consists of two parts treated alternatively; the calculation of the boundary layer (viscous region) and the calculation of the outer inviscid flow. In the direct method the boundary layer equations are solved with prescribed pressure p and the outer flow is computed with the prescribed displacement thickness δ^* . In the inverse method, the role of p and δ^* are interchanged. As discussed previously, the direct method breaks down at separation point and the inverse method must be utilized. For the inverse procedure discussed above the convergence of the iterative process is slow due to the need for severe under relaxation. Carter and Wornom [29] had to use an under relaxation factor of 0.2 and the convergence gets even slower when the region of inverse boundary layer calculation is enlarged. A second drawback is the difficulty to obtain a smooth transition from a directly to an inversely calculated region [30].

A large improvement over the inverse method can be obtained by applying the semi-inverse method of Le Balleur [31]. Here the boundary layer is calculated inversely, but the outer flow is calculated in a direct way. Thus both parts of the flow field are calculated with prescribed displacement thickness, resulting in two pressure distributions which must be the same at convergence. An iterative cycle is completed with a relaxation formula which combines the old displacement thickness and the two pressure distributions into an updated displacement thickness. Underrelaxation was still required but convergence occurred in fewer iterations. The method of Kwon and Fletcher [32] and Carter [33] possess the same type of calculation procedure as Le Balleur but the relaxation procedure allows for over

relaxation leading to more rapid convergence. For the aforementioned schemes with alternate treatment of viscous and inviscid regions, the numerical procedure provides only a weak, retarded coupling of both regions. As previously stated near separation and near the trailing edge, the interaction has a strong simultaneous character and there does not exist a definite hierarchy between the boundary layer and the outer inviscid flow [34]. Thus it is expected that a numerical scheme which possesses a simultaneous coupling of the viscous and inviscid parts of the flow field would have favorable properties with regards to convergence. For isolated airfoils in incompressible flow, Veldman [35] accomplishes this with a linear combination of the pressure and displacement thickness and the boundary condition possesses the elliptic character of the outer flow. The iterative process converges rapidly allowing over relaxation to be applied. A survey of the literature for cascade flow is found in the work of Moses et al. [36,37], where a simultaneous solution of the inviscid flow and boundary layer equations for compressor cascades operating in incompressible flow was performed.

The present work includes the effect of compressibility coupled with the interactive procedure of Veldman [35]. The inviscid flow field is a two-dimensional finite area potential flow model which can handle transonic flow. The discussion of the inviscid flow solver is found in Chapter 2. The boundary layer routine is a two-dimensional implicit finite difference routine and the calculation procedure including the viscous-inviscid interaction calculation is found in Chapter 3.

CHAPTER 2 Inviscid Flow Field Modelling

2.1 Introduction

For the design of modern compressor and turbine airfoils with high inlet subsonic Mach numbers, an inviscid analysis that can handle the effects of compressibility and weak shocks is required. It is important that the analysis be both accurate and computationally efficient. Also the prediction scheme must have great flexibility in modelling the cascade geometry, as wide variations in the combinations of blade thickness, gap/chord ratio, and stagger can be expected.

Several inviscid flow calculations can be utilized with varying degrees of success in terms of the above mentioned criteria. For rotational flow with strong shocks the time dependent Euler equations would be required. However, the computing costs can be prohibitive particularly in the preliminary design stage. Also strong shocks are typically not present as the peak Mach number on the blade suction surface is usually less than one, and no shocks will exist. For an advanced compressor blade section there can be a region on the suction surface where the Mach number is slightly greater than one. But even under these conditions, shocks if present are weak and the flow will essentially retain its irrotational nature. For irrotational flow, a potential flow solver can be utilized. Solution of the full potential equations, which would be required to handle the wide range of geometric conditions, are faster by a factor of roughly ten over the Euler equations while obtaining comparable accuracy even with strong shocks present [38]. Further reductions in computing time be obtained through use of the small dis-

turbance form of the potential flow equations. The assumptions associated with small perturbation theory can cause substantial error for cascades with high turning. Therefore for the prediction of the inviscid flow field, the solution of the full potential equations were chosen.

2.2 Two-Dimensional Compressible Potential Flow for Cascades

The inviscid flow solver is based on a finite area method which calculates flow properties in the physical plane on a non-orthogonal grid [39]. Working in the physical plane eliminates the mapping step required in the work of Ref. [40] and thereby increases the geometric flexibility. For example, decreasing gap to chord ratios make the cascade increasingly difficult to map. The flow is assumed to be two-dimensional, compressible, steady and irrotational. The direction parallel to the cascade is the tangential or "y" direction, while the normal direction through the cascade line is the axial or "x" direction. For irrotational flow a potential function ϕ exists such that

$$\phi_x = \frac{u}{V_1} \tag{2.1}$$

$$\phi_y = \frac{v}{V_1}$$

where

- ϕ_x - partial derivative of the potential function with respect to the axial direction
- ϕ_y - partial derivative of the potential function with respect to the tangential direction

- u - axial velocity
- v - tangential velocity
- V_1 - relative inlet velocity

For the present analysis, an integro-differential form of mass conservation through finite areas is utilized. The approximation is second-order accurate on smoothly varying grids despite the mesh distorting effects of stagger, turning and thickness. For any finite area enclosed by a piecewise smooth simply connected curve D, ϕ must satisfy continuity, which for steady flow is given by

$$\int_D r \phi_n ds = 0 \quad (2.2)$$

where r is the modified density ratio given by

$$r = \frac{H}{H_w} \frac{\rho}{\rho_T} = \frac{H}{H_w} \left(1 - \left[\frac{\gamma-1}{2} M_1^2 \right] |\nabla \phi|^2 / \left[1 + \frac{\gamma-1}{2} M_1^2 \right] \right)^{\frac{1}{\gamma-1}} \quad (2.3)$$

where

$\frac{H}{H_w}$ is used to correct for the effects of endwall boundary layers

and

$\frac{\rho}{\rho_T}$ is the ratio of the static to total density.

In Eq. (2.2), ϕ_n is the velocity normal to the curve D at any location.

In addition to satisfying Eq. (2.2), the following boundary conditions must be satisfied:

Flow tangency:

$$\phi_n = 0 \quad \text{on the airfoil surface} \quad (2.4)$$

Periodicity:

$$\nabla \phi(x, y + \tau) = \nabla \phi(x, y) \quad (2.5)$$

τ - blade gap

Far Field

ϕ_x, ϕ_y specified and constant on the far upstream and downstream stations

The derivatives ϕ_x, ϕ_y are obtained from knowledge of Mach numbers M_1 and M_2 and the flow angles θ_1 and θ_2 . Note that these four quantities are related by global mass conservation, therefore only three of them need to be specified. If the trailing edge is sharp, the condition that ϕ_x and ϕ_y be specified in the downstream region is then replaced by the Kutta condition such that the velocity be continuous there.

2.2.1 Finite Area Mass Balance and Grid Generation

Due to the periodic boundary condition given by Eq. (2.5) a strict geometric limitation is imposed on cascade grid. To obtain tightly bonded matrices required for computational efficiency and to insure second order accuracy, the mesh must be periodic. Grid points associ-

ated with one set of mesh curves should begin and end either on airfoil surfaces or at points periodic to each other. A mesh composed of streamlines and potential lines is not periodic except for the simple case of purely axial flow. The grid employed here is a nonorthogonal periodic mesh composed of vertical lines and contour curves which are averages of the airfoil contours. It is easily constructed for any cascade geometry and can be refined where needed. A sample grid is shown in Fig. 1. The mesh is then triangulated to produce acute triangles wherever possible as indicated in Fig. 2. In regions of rapidly changing curvature or in the vicinity of a blunt leading edge, this may not be possible. Under these conditions a localized error will be seen in the solution as obtuse triangles will produce polygons with negative areas. This can be overcome through grid refinement in regions of high curvature or a local orthogonal grid for the blunt leading edge condition. The local grid will be discussed later. Each grid point is thereby connected to all of its neighboring grid points. The perpendicular bisectors of the neighbor lines are constructed forming the mesh polygon D as seen in Fig. 3. Since the perpendicular bisectors of the sides of the triangles meet at a point, the mesh polygons cover the entire cascade passage exactly, and each grid point is in only one mesh polygon. For an orthogonal mesh, as is found in the upstream and downstream flow fields, these polygons reduce to rectangles.

To satisfy continuity which is given by Eq. (2.2) a finite area mass balance approach will be utilized for each polygon.

$$\int_D r \phi_n ds = 0 \approx \sum_m \frac{r_m + r_o}{2} \left(\frac{\phi_m - \phi_o}{h_m} \right) \zeta_m \quad (2.6)$$

where

ζ_m is the length of the mth polygon face

h_m is the distance between the mth grid point and the reference grid point inside the polygon

The subscripts m and o denote a particular polygon side and polygon center, respectively. To satisfy the flow tangency conditions given by Eq. (2.4), there must be no mass flow across the airfoil surface. Thus, the terms corresponding to mass flux at the airfoil surface are set to zero. By satisfying Eq. (2.6) at each grid point, the continuity equation is preserved. Also, since the mesh polygons cover the entire cascade passage with no overlap, the continuity equation is satisfied globally. Because mass conservation is expressed in integral rather than differential form, only first derivatives must be approximated, in comparison to the typical potential differential equation given in conservation form as;

$$(r \phi_x)_x + (r \phi_y)_y = 0 \quad (2.7)$$

Also the derivatives are in the directions determined by the neighboring mesh points. Thus, the approximation given by Eq. (2.6) avoids the problem of approximating Cartesian derivatives on a non-orthogonal grid. The grid system described remains second order accurate provided the grid is quasi uniform or that the variation of the grid spacing varies smoothly on a given grid line. In general, the cascade analysis

based on the grid of Fig. 1 gives suitably accurate results for most typical cascade geometry. This may not be the case, however, if detailed results are needed about blunt leading edges. For instance, it may be required to determine the location of the leading edge stagnation point or predict a very strong pressure gradient. Due to the nature of the grid in Fig. 1, for a blunt leading edge, these details are lost. To obtain this information a local analysis is performed based on the results from the global analysis on a relatively coarse grid. The local analysis is made only in the region of interest and the remaining flow field description is assumed to be correct based on the converged coarse grid solution. This is based on numerical experimentation which has shown that the effects of the approximation errors at the leading edge are propagated only a short distance from the source of the error. The local mesh is orthogonal as shown in Fig. 4. The local mesh calculation is performed separately from the coarse grid calculation. The boundary conditions are the flow tangency condition of the airfoil surface and for the outermost grid line and the first and last wall normal grid line, the value of the potential function is specified and held constant. The specified values for the potential function are obtained by interpolations from the coarse grid solution. The local mesh is orthogonal as is shown in fig. 4. For the case of an orthogonal mesh the mesh polygons become parallelograms.

2.2.2 Resulting System of Equations and Solution Technique

A nonlinear system of equations will arise from the relations found in Eqs. (2.3) and (2.6). These can be expressed as

$$F(r) \bar{\phi} = D(r) \quad (2.8)$$

$$\bar{r} = R(\phi) \quad (2.9)$$

where \bar{r} and $\bar{\phi}$ are vectors comprised of the r and ϕ values at the grid points. The elements of the F matrix and the D vector depend on r while R is a function of ϕ only. The system of equations in Eqs. (2.8) and (2.9) are solved iteratively by first fixing r solving Eq. (2.8) to update ϕ and then with ϕ fixed, Eq. (2.9) is solved for r . To minimize roundoff error, the change in the potential function can be calculated rather than the potential function.

Defining

$$\Delta \phi = \phi^{n+1} - \phi^n$$

with n as the iteration number, Eq. (2.8) can be written as

$$F \Delta \bar{\phi} = D - F \bar{\phi}^n = \Delta D \quad (2.10)$$

Also in order to increase the rate of convergence successive over relaxation (SOR) can be performed on the density

$$r^{n+1} = \omega r^{n+1} + (1 - \omega) r^n \quad (2.11)$$

The typical range for the relaxation factor ω is from 1.2 to 1.8.

For the calculation of the density ratio from Eq. (2.3), the deriv-

atives ϕ_x and ϕ_y must be approximated. This is accomplished by interpolation using orthogonal polynomials as described in Ref. [41]. At the airfoil surface the axial velocity ϕ_x is calculated then ϕ_y is found by satisfying the flow tangency condition, Eq. (2.4). By interpolation with orthogonal polynomials the calculation of ϕ_x and ϕ_y is formally second order accurate.

To insure a computational efficient algorithm, the most desirable system of equations is a block tridiagonal system. To obtain a block tridiagonal system, the upstream and downstream boundary conditions must be invoked. Consider the first upstream grid line as shown in Fig. 5. At this location ϕ_x and ϕ_y are constant from the boundary conditions. Upstream of this point the density and pressure are also constant. Consider the application of Eq. (2.6) to an elemental area associated with the first grid line. Note that this area extends beyond the first grid line at $I=1$, therefore a fictitious grid line at $I=0$ is required. The sides of the element are numbered clockwise with the upstream face being 1. The contribution of side 1 to Eq. (2.6) is as follows;

$$\frac{(r(0,j) + r(1,j))}{2} (\phi(0,j) - \phi(1,j)) \frac{\Delta y}{\Delta x} \quad (2.12)$$

The quantities $r(0,j)$ and $\phi(0,j)$, where the 0 denotes the i or x grid location and j the y grid location, are quantities upstream of the first grid line, or calculation field. They can, however, be obtained based on the upstream boundary condition. The density is assumed to be constant upstream of the first grid line,

$$r(0,j) = r(1,j) \quad (2.13)$$

For $\phi(0,j)$ a second order accurate centered difference expression gives;

$$\frac{\phi(2,j) - \phi(0,j)}{2 \Delta x} = \phi_x(1,j) \quad (2.14)$$

or

$$\phi(0,j) = \phi(2,j) - 2 \Delta x \phi_x \quad (2.15)$$

where ϕ_x is known from the boundary condition.

From the contribution of side 1 the following expression exists;

$$r(1,j)(\phi(2,j) - \phi(1,j) - 2 \Delta x \phi_x(1,j)) \frac{\Delta y}{\Delta x} \quad (2.16)$$

This expression is valid for $j = 2$ to $j = \text{NGY}$ where NGY is the number of grid points in the tangential direction. The relationship between the grid point at $j = 1$ and $j = \text{NGY}$ is obtained from the periodicity boundary condition Eq.(2.5). Since the grid is periodic the value of the potential function at $j = \text{NGY}$ is,

$$\phi(i,\text{NGY}) = \phi(i,1) + C \quad (2.17)$$

Equation (2.7) is valid upstream of the cascade leading edge. The constant C is given by

$$C = \int_0^s \phi_y dy = \phi_y s \quad (2.18)$$

where s is the blade spacing.

Similar expressions to Eqs. (2.17) and (2.18) hold for the downstream flow field. The following system of equations is generated.

At $i = 1$

$$\bar{B}_1 \Delta \bar{\phi}_1 + \bar{C}_1 \Delta \bar{\phi}_2 = \bar{d}_1 \quad (2.19)$$

For $i = 2$ to $NGX - 1$

$$\bar{A}_i \Delta \bar{\phi}_{i-1} + \bar{B}_i \Delta \bar{\phi}_i + \bar{C}_i \Delta \bar{\phi}_{i+1} = \bar{d}_i \quad (2.20)$$

$i = NGX$

$$\bar{A}_i \Delta \bar{\phi}_{i-1} + \bar{B}_i \Delta \bar{\phi}_i = \bar{d}_i \quad (2.21)$$

where \bar{A} , \bar{B} and \bar{C} are the coefficient matrices based on Eq. (2.6), and $\Delta \bar{\phi}$ and \bar{d} are column vectors. NGX is the number of grid points in the axial direction. The block tridiagonal system of equations can be solved efficiently using a block tridiagonal solver developed by Swift [42]. This solution technique is found in Appendix A.

2.2.3 Extension to Transonic Flow

For the inviscid solver chosen in this work, irrotational flow was assumed and a potential formulation was used. Thus no dissipative

mechanism is present in the system of equations given by Eqs. (2.19), (2.20) and (2.21). A result of eliminating changes in entropy is the existence of both expansion and compression shocks as valid solutions. While this is not a problem for subsonic flow, the existence of expansion shocks in supersonic flow is unacceptable and must be avoided. This problem is overcome by the use of implicitly or explicitly added artificial viscosity or compressibility. For transonic conditions both subsonic and supersonic patches will exist along the airfoil. As the flow changes from subsonic to supersonic the nature of equations changes from elliptic to hyperbolic and an elliptic solver based on a central difference method is doomed to failure as no artificial viscosity is present. For the supersonic region, an upwind differencing scheme is usually required, as positive artificial viscosity is introduced into the calculation from the higher order terms of the finite difference equations and the acceptable solution of a compression shock is obtained. For supersonic calculations using an upwind differencing scheme, an explicit space marching technique is used rather than an implicit procedure as in subsonic flow. For an explicit procedure the CFL condition [43] must be satisfied to ensure a stable calculation. For the Mach number close to one as is the case of advanced compressor rotors, the CFL stability criterion prohibits reasonable step sizes causing an explicit calculation to become impractical. Thus the same calculation procedure as subsonic flow will be used with artificial compressibility [44] added to ensure the correct solution concerning compression shocks. An upwind differencing technique is used when calculating the density by

$$r = r - \chi \mu \Delta r \quad (2.22)$$

where

χ - artificial compressibility factor

$$\mu = \max(0, 1 - \frac{1}{M^2})$$

and

$$\Delta r = \nabla r \cdot \nabla \phi \Delta s / |\nabla \phi| \quad (2.23)$$

Δs is the local mesh spacing.

In Eq. (2.22] increasing the value of χ enhances the stability of the calculation procedure. However, increasing χ to enhance stability, must be done with care since the discrete solution is affected by the choice of χ , in particular the shock location can be shifted. Also the use of artificial compressibility does increase the local truncation error of the solution. While the central differencing technique is second order accurate the upwind differencing described here approaches only first order accuracy. The larger the artificial compressibility factor, the more biased the differencing will be in the upwind direction, and the closer the local solution to the first order accuracy. Thus, χ should be chosen as small as possible to ensure stability typically in the range of 0.5 to 2.

2.3 Sample Calculations

To assess the validity and accuracy of the finite area approach to

the full potential equation, three test cases were analyzed and compared with the exact or hodograph solution. A description of the exact solution technique is found in [45]. The first comparison was with the Gostelow compressor cascade hodograph solution [45]. The flow was incompressible and the cascade consisted of airfoils with blunt leading edges and cusped trailing edges (Fig. 6). A comparison of the current analysis with the exact solution in terms of pressure coefficient versus percent chord shows very good agreement (Fig. 7). Due to the blunt leading edge a local analysis was required to obtain good agreement in the leading edge region. The local grid was initiated at 65% chord on the suction surface and finished at 40% chord on the pressure surface, with 65 grid points along the airfoil surface and 9 grid points in the wall normal direction. Total run time for the global and local solution was less than 10 seconds on an IBM 3090 computer.

The next case considered was the transonic turbine impulse cascade shown in Fig. 8. The exact or hodograph solution for this cascade was produced by Hobson [46]. A comparison of Mach number versus axial chord was made. As seen in Fig. 9, good agreement was obtained. Due to the sharp leading and trailing edges, no local analysis was required. For this case, total run time was approximately 15 seconds on an IBM 3090 computer.

The third comparison was made with the exact solution of the Korn shock free transonic compressor cascade seen in Fig. 10 [47]. The initial calculation was done without the use of artificial compressibility and an expansion wave was generated just beyond the leading edge on the suction surface as the peak Mach number approached 1.4. With the

addition of artificial compressibility and a local analysis due to the blunt leading edge, good agreement was obtained between the computed and exact Mach number distribution (Fig. 11). The total run time was approximately 40 seconds on an IBM 3090 computer.

CHAPTER 3
Viscous Flow Field Modelling

For an accurate assessment of the cascade intrablade aerodynamics and the wakes emanating from the blade trailing edge and moving downstream, the viscous effects at the airfoil surface and in the blade wake must be taken into account. For the case of a typical compressor or turbine cascade, the viscous effects are important only near the blade surface and in a thin wake, and therefore a boundary layer approach is valid.

3.1. Equations for Laminar and Turbulent Compressible Boundary Layer

The Navier-Stokes equations for the two-dimensional case are as follows:

Continuity

$$\frac{\partial \rho^*}{\partial t^*} + u^* \frac{\partial \rho^*}{\partial x^*} + v^* \frac{\partial \rho^*}{\partial y^*} + \rho^* \left(\frac{\partial u^*}{\partial x^*} + \frac{\partial v^*}{\partial y^*} \right) = 0 \quad (3.1)$$

X Momentum

$$\begin{aligned} \rho^* \left(\frac{\partial u^*}{\partial t^*} + u^* \frac{\partial u^*}{\partial x^*} + v^* \frac{\partial u^*}{\partial y^*} \right) &= - \frac{\partial p^*}{\partial x^*} \\ + \frac{\partial}{\partial x^*} \left[\lambda^* \left(\frac{\partial u^*}{\partial x^*} + \frac{\partial v^*}{\partial y^*} \right) + 2\mu \frac{\partial u^*}{\partial x^*} \right] \\ + \frac{\partial}{\partial y^*} \left[\mu^* \left(\frac{\partial u^*}{\partial y^*} + \frac{\partial v^*}{\partial x^*} \right) \right] \end{aligned} \quad (3.2)$$

Y Momentum

$$\begin{aligned}
 \rho^* \left(\frac{\partial v^*}{\partial t^*} + u^* \frac{\partial v^*}{\partial x^*} + v^* \frac{\partial v^*}{\partial y^*} \right) &= - \frac{\partial p^*}{\partial y^*} \\
 + \frac{\partial}{\partial y^*} \left[\lambda^* \left(\frac{\partial u^*}{\partial x^*} + \frac{\partial v^*}{\partial y^*} \right) + 2\mu \frac{\partial v^*}{\partial y^*} \right] \\
 + \frac{\partial}{\partial x^*} \left[\mu^* \left(\frac{\partial v^*}{\partial x^*} + \frac{\partial u^*}{\partial y^*} \right) \right] & \quad (3.3)
 \end{aligned}$$

Energy

$$\begin{aligned}
 \rho^* \left(\frac{\partial h^*}{\partial t^*} + u^* \frac{\partial h^*}{\partial x^*} + v^* \frac{\partial h^*}{\partial y^*} \right) &= \frac{\partial p^*}{\partial t^*} + u^* \frac{\partial p^*}{\partial x^*} \\
 + v^* \frac{\partial p^*}{\partial y^*} + \frac{\partial}{\partial x^*} \left(k^* \frac{\partial T^*}{\partial x^*} \right) \\
 + \frac{\partial}{\partial y^*} \left(k^* \frac{\partial T^*}{\partial y^*} \right) + \phi^* & \quad (3.4)
 \end{aligned}$$

where the dissipation function ϕ^* is

$$\phi^* = \lambda^* \left(\frac{\partial u^*}{\partial x^*} + \frac{\partial v^*}{\partial y^*} \right)^2 + 2\mu^* \left[\left(\frac{\partial u^*}{\partial x^*} \right)^2 + \frac{1}{2} \left(\frac{\partial u^*}{\partial y^*} + \frac{\partial v^*}{\partial x^*} \right)^2 + \left(\frac{\partial v^*}{\partial y^*} \right)^2 \right]$$

To nondimensionalize the equations, let

$$\begin{aligned}
 x^* &= L x \\
 y^* &= L y \\
 u^* &= u_\infty u \\
 v^* &= u_\infty v
 \end{aligned}$$

$$\begin{aligned}
\rho^* &= \rho_\infty^* \rho \\
p^* &= \rho_\infty^* u_\infty^{*2} p \\
t^* &= L t / u_\infty^* \\
\mu^* &= \mu_\infty^* \mu \\
T^* &= T_\infty^* T \\
h^* &= C_{p\infty}^* T_\infty^* h \\
C_p^* &= C_{p\infty}^* C_p \\
\lambda^* &= \mu_\infty^* \lambda
\end{aligned} \tag{3.5}$$

Substituting the relationships in Eqs. (3.5) into Eqs. (3.1) - (3.4) gives:

Continuity

$$\frac{\partial \rho}{\partial t} + u \frac{\partial \rho}{\partial x} + v \frac{\partial \rho}{\partial y} + \rho \left(\frac{\partial u}{\partial x} + \frac{\partial v}{\partial y} \right) = 0 \tag{3.6}$$

X-Momentum

$$\begin{aligned}
\rho \left(\frac{\partial u}{\partial t} + u \frac{\partial u}{\partial x} + v \frac{\partial u}{\partial y} \right) &= - \frac{\partial p}{\partial x} \\
+ \frac{1}{Re} \left\{ \frac{\partial}{\partial x} \left[\lambda \left(\frac{\partial u}{\partial x} + \frac{\partial v}{\partial y} \right) + 2\mu \frac{\partial u}{\partial x} \right] \right. \\
+ \left. \frac{\partial}{\partial y} \left[\mu \left(\frac{\partial u}{\partial y} + \frac{\partial v}{\partial x} \right) \right] \right\} &
\end{aligned} \tag{3.7}$$

Y-Momentum

$$\rho \left(\frac{\partial v}{\partial t} + u \frac{\partial v}{\partial x} + v \frac{\partial v}{\partial y} \right) = - \frac{\partial p}{\partial y} + \frac{1}{\text{Re}} \left\{ \frac{\partial}{\partial y} \left[\lambda \left(\frac{\partial u}{\partial x} + \frac{\partial v}{\partial y} \right) + 2\mu \frac{\partial v}{\partial y} \right] + \frac{\partial}{\partial x} \left[\mu \left(\frac{\partial v}{\partial x} + \frac{\partial u}{\partial y} \right) \right] \right\} \quad (3.8)$$

Energy

$$\rho \left(\frac{\partial h}{\partial t} + u \frac{\partial h}{\partial x} + v \frac{\partial h}{\partial y} \right) = (\gamma - 1) M_\infty^2 \left(\frac{\partial p}{\partial t} + u \frac{\partial p}{\partial x} + v \frac{\partial p}{\partial y} \right) + \frac{1}{\text{Re}} \frac{\partial}{\partial x} \left[\left(\frac{C_p \mu}{\text{Pr}} \right) \frac{\partial T}{\partial x} \right] + \frac{\partial}{\partial y} \left[\left(\frac{C_p \mu}{\text{Pr}} \right) \frac{\partial T}{\partial y} \right] + \frac{(\gamma - 1) M_\infty^2 \phi}{\text{Re}} \quad (3.9)$$

where the dissipation function is

$$\phi = \lambda \left(\frac{\partial u}{\partial x} + \frac{\partial v}{\partial y} \right)^2 + 2\mu \left[\left(\frac{\partial u}{\partial x} \right)^2 + \frac{1}{2} \left(\frac{\partial u}{\partial y} + \frac{\partial v}{\partial x} \right)^2 + \left(\frac{\partial v}{\partial y} \right)^2 \right]$$

and

$$\text{Re} = \frac{\rho_\infty^* u_\infty^* L^*}{\mu_\infty^*}$$

$$\text{Pr} = \frac{C_p^* \mu^*}{k^*}$$

The boundary conditions for these equations are as follows:

At the wall

$u = 0$ No slip condition
 $v = 0$ No penetration condition
 $T = T(t, X)$ Specified wall temperature

or

$$\frac{\partial T}{\partial n} = f(t, x) \quad \text{specified heat transfer}$$

Far from the wall the flow field is specified.

Consider Eqs. (3.6) - (3.9) in the limit as $Re \rightarrow \infty$. The Euler equations are obtained.

$$\frac{\partial \rho}{\partial t} + \frac{\partial \rho u}{\partial x} + \frac{\partial \rho v}{\partial y} = 0 \quad (3.10)$$

$$\rho \left(\frac{\partial u}{\partial t} + u \frac{\partial u}{\partial x} + v \frac{\partial u}{\partial y} \right) = - \frac{\partial p}{\partial x} \quad (3.11)$$

$$\rho \left(\frac{\partial v}{\partial t} + u \frac{\partial v}{\partial x} + v \frac{\partial v}{\partial y} \right) = - \frac{\partial p}{\partial y} \quad (3.12)$$

$$\rho \frac{Dh}{Dt} = (\gamma - 1) M_\infty^2 \frac{Dp}{Dt} \quad (3.13)$$

The boundary conditions will now be investigated. The solution to the Euler equations will be incorrect at the wall because in order to satisfy the no slip conditions, $\frac{\partial u}{\partial y} \rightarrow \infty$. To overcome this problem, the double limit $Re \rightarrow \infty$, $y \rightarrow 0$ must be considered. First, introduce the following stretching parameters:

Let

$$y = \bar{y} / \sqrt{\text{Re}} \quad (3.14)$$

$$v = \bar{v} / \sqrt{\text{Re}}$$

The other variables remain unchanged. Once again take the limit as $\text{Re} \rightarrow \infty$ in Eq. (3.6) - (3.9) with the new variables introduced. This results in the following:

Continuity

$$\frac{\partial \rho}{\partial t} + \frac{\partial \rho u}{\partial x} + \frac{\partial \rho \bar{v}}{\partial \bar{y}} = 0 \quad (3.15)$$

X-Momentum

$$\rho \left(\frac{\partial u}{\partial t} + u \frac{\partial u}{\partial x} + \bar{v} \frac{\partial u}{\partial \bar{y}} \right) = - \frac{\partial p}{\partial x} + \frac{\partial}{\partial \bar{y}} \left[\mu \frac{\partial u}{\partial \bar{y}} \right] \quad (3.16)$$

Y-Momentum

$$\frac{\partial p}{\partial \bar{y}} = 0 \quad (3.17)$$

Energy Equation

$$\rho \left(\frac{\partial h}{\partial t} + u \frac{\partial h}{\partial x} + \bar{v} \frac{\partial h}{\partial y} \right) = (\gamma - 1) M_\infty^2 \left(\frac{\partial p}{\partial t} + u \frac{\partial p}{\partial x} \right) + \frac{\partial}{\partial y} \left[\frac{C_p \mu}{Pr} \frac{\partial T}{\partial y} \right] + (\gamma - 1) M_\infty^2 \left(\frac{\partial u}{\partial y} \right)^2 \quad (3.18)$$

Equations (3.15) through (3.18) are valid in the region close to the wall. The solution of these equations must be matched with the inviscid solution far from the wall, at the edge of the boundary layer. For the inviscid field the following limit exists.

$$u_e(x, t) = \lim_{y \rightarrow 0} u_{inv}(x, y, t)$$

and for the boundary layer solution

$$u_{bl} = \lim_{\bar{y} \rightarrow \infty} u_{bl}(x, \bar{y}, t)$$

Thus, to match the viscous and inviscid flow fields

$$u_{bl} = u_e(x, t) \quad \text{as } \bar{y} \rightarrow \infty$$

where

- u_e - edge velocity
- u_{inv} - inviscid velocity
- u_{bl} - boundary layer velocity

A composite solution can be formed in the adjoining region for the viscous and inviscid fields as

$$u_c = u_{inv} + u_{bl} - u_e \quad (3.19)$$

Next, the temperature profile is considered. The inviscid solution near the wall does not match the boundary layer solution. Therefore, a composite solution must also be used here. Let

$$\begin{aligned} T_e(x,t) &= \lim_{y \rightarrow 0} T_{inv}(x,y,t) \\ &\text{and} \\ T_{bl} &= \lim_{\bar{y} \rightarrow \infty} T_{bl}(x,\bar{y},t) \end{aligned}$$

The matching condition will be

$$T_{bl} = T_e(x,t) \quad \text{as } \bar{y} \rightarrow \infty$$

A composite solution for the adjoining flow fields will be

$$T_c = T_{inv} + T_{bl} - T_e \quad (3.20)$$

The v component of the velocity must be matched in both the inviscid and boundary layer flow to $O(1/\sqrt{\text{Re}})$.

The continuity equation in the boundary layer is

$$\frac{\partial \rho}{\partial t} + \frac{\partial \rho u}{\partial x} + \frac{\partial \rho \bar{v}}{\partial y} = 0$$

For large \bar{y} (boundary layer edge)

$$\frac{\partial \rho \bar{v}}{\partial y} = - \left(\frac{\partial \rho_e}{\partial t} + \frac{\partial \rho_e u_e}{\partial x} \right)$$

Integrating this expression gives

$$\rho_e \bar{v}_e = - \left(\frac{\partial \rho_e}{\partial t} + \frac{\partial \rho_e u_e}{\partial x} \right) \bar{y} + F(x, t)$$

Dividing by $\sqrt{\text{Re}}$ gives

$$\rho_e v_e = - \left(\frac{\partial \rho_e}{\partial t} + \frac{\partial \rho_e u_e}{\partial x} \right) y + F(x, t) / \sqrt{\text{Re}} \quad (3.21)$$

For the inviscid flow field

$$\rho_e v_e = - \left(\frac{\partial \rho_e}{\partial t} + \frac{\partial \rho_e u_e}{\partial x} \right) y + O(y^2)$$

Thus as $\text{Re} \rightarrow \infty$ matching of the v component is matched.

The assumption of a perfect gas will be made. The enthalpy is given by

$$h = C_p T \quad (3.22)$$

For steady flow the energy equation then becomes for constant specific heat

$$\rho u \frac{\partial T}{\partial x} + \rho v \frac{\partial T}{\partial y} = (\gamma - 1) M_\infty^2 u \frac{dp}{dx} + \frac{1}{Pr} \frac{\partial}{\partial y} \left(\mu \frac{\partial T}{\partial y} \right) + (\gamma - 1) M_\infty^2 \mu \left(\frac{\partial u}{\partial y} \right)^2 \quad (3.23)$$

The boundary layer equation will be solved for both laminar and turbulent flow. Osborne Reynolds [48] in 1883 was the first to observe and study the phenomena of transition from laminar to turbulent flow. Reynolds assumed that the instantaneous fluid velocity satisfied the Navier Stokes equations and that the instantaneous velocity could be separated into mean and fluctuating components. The result was a set of Reynolds equations which differed from the Navier-Stokes equations only through additional terms called the Reynolds stresses. Including these terms in the boundary layer equations for steady flow with constant specific heat gives [49],

Continuity

$$\frac{\partial}{\partial x} (\rho u) + \frac{\partial}{\partial y} \left[\rho \left(v + \frac{\overline{\rho'v'}}{\rho} \right) \right] = 0 \quad (3.24)$$

X-Momentum

$$\rho \left[u \frac{\partial u}{\partial x} + \left(v + \frac{\overline{\rho'v'}}{\rho} \right) \frac{\partial u}{\partial y} \right] = - \frac{dp}{dx} + \frac{\partial}{\partial y} \left[\mu \frac{\partial u}{\partial y} - \overline{\rho u'v'} \right] \quad (3.25)$$

Energy

$$\begin{aligned}
 \rho \left[u \frac{\partial T}{\partial x} + \left(v + \frac{\overline{\rho'v'}}{\rho} \right) \frac{\partial T}{\partial y} \right] &= (\gamma-1) M_\infty^2 u \frac{dp}{dx} \\
 + \frac{\partial}{\partial y} \left(\frac{\mu}{Pr} \frac{\partial T}{\partial y} \right) + (\gamma-1) M_\infty^2 \mu \left(\frac{\partial u}{\partial y} \right)^2 \\
 + \frac{\partial}{\partial y} \left[-\overline{\rho v' T'} \right] - (\gamma-1) M_\infty^2 \overline{\rho u' v'} \frac{\partial u}{\partial y} & \quad (3.26)
 \end{aligned}$$

The bars on the v component of velocity and y have been dropped to avoid confusion with averaged quantities. A new velocity component normal to the surface can be defined as

$$\tilde{v} = v + \frac{\overline{\rho'v'}}{\rho} \quad (3.27)$$

The eddy viscosity is defined as

$$\epsilon = -\rho \frac{\overline{u'v'}}{\partial u / \partial y} \quad (3.28)$$

The turbulent Prandtl number can be expressed as

$$Pr_t = \frac{\overline{u'v'}}{\overline{v'T'}} \left(\frac{\partial T / \partial y}{\partial u / \partial y} \right) \quad (3.29)$$

A discussion of the turbulent Prandtl number is found in Harris [50]. Substituting Eqs. (3.27), (3.28), and (3.29), into Eqs. (3.24), (3.25) and (3.26) gives

Continuity

$$\frac{\partial}{\partial x} (\rho u) + \frac{\partial}{\partial y} (\rho \tilde{v}) = 0 \quad (3.30)$$

Momentum

$$\rho \left[u \frac{\partial u}{\partial x} + \tilde{v} \frac{\partial u}{\partial y} \right] = - \frac{dp}{dx} + \frac{\partial}{\partial y} \left[\mu \bar{\epsilon} \frac{\partial u}{\partial y} \right] \quad (3.31)$$

Energy

$$\begin{aligned} \rho \left[u \frac{\partial T}{\partial x} + \tilde{v} \frac{\partial T}{\partial y} \right] &= (\gamma - 1) M_\infty^2 u \frac{dp}{dx} \\ &+ (\gamma - 1) M_\infty^2 \mu \bar{\epsilon} \left(\frac{\partial u}{\partial y} \right)^2 \\ &+ \frac{\partial}{\partial y} \left[\frac{\mu}{Pr} \hat{\epsilon} \frac{\partial T}{\partial y} \right] \end{aligned} \quad (3.32)$$

where

$$\bar{\epsilon} = 1 + \frac{\epsilon}{\mu} \quad (3.33)$$

$$\hat{\epsilon} = 1 + \frac{\epsilon}{\mu} \frac{Pr}{Pr_t}$$

with $Pr_t = .95$.

When working with the primitive variables, a singularity in the equations will occur at the stagnation point. Also as the boundary layer grows along the body, in a finite difference solution more and

more grid points must be added to describe the flow field. To overcome these problems the Levy-Lees transformation [51] will be employed.

Levy-Lees Variables

$$\xi(x) = \int_0^x \rho_e u_e \mu_e r^{2m} dx \quad (3.34)$$

$$\eta(x,y) = \frac{u_e r^m}{\sqrt{2\xi(x)}} \int_0^y \rho_e dy$$

where

$m = 0$ 2-D flow

$m = 1$ axisymmetric flow.

The relationship between the derivatives in the physical plane and the transformed plane are as follows,

$$\left(\frac{\partial}{\partial x}\right)_y = \rho_e u_e \mu_e \left(\frac{\partial}{\partial \xi}\right)_\eta + \eta_x \left(\frac{\partial}{\partial \eta}\right)_\xi \quad (3.35)$$

$$\left(\frac{\partial}{\partial y}\right)_x = \frac{\rho_e u_e}{\sqrt{2\xi}} \left(\frac{\partial}{\partial \eta}\right)_\xi$$

The Euler equation gives the following relationship at the boundary layer edge,

$$\rho_e u_e \frac{du_e}{dx} = - \frac{dp_e}{dx} \quad (3.36)$$

From the ideal gas equation of state and the y momentum equation at a

particular x location;

$$p = \rho RT = p_e = \text{const.} \quad (3.37)$$

Thus the density in the boundary layer is related to the temperature as

$$\frac{\rho_e}{\rho} = \frac{T}{T_e} \quad (3.38)$$

Utilizing Eqs. (3.34) - (3.38) in Eqs. (3.30) - (3.32) gives the following equations in the transformed coordinate system

Continuity Equation

$$2 \xi F F_\xi + V_\eta + F = 0 \quad (3.39)$$

X-Momentum

$$2 \xi F F_\xi + V F_\eta - (\theta \bar{\epsilon} F_\eta)_\eta + \beta(F^2 - Q) = 0 \quad (3.40)$$

Energy equation

$$2 \xi F Q_\xi + V Q_\eta - \left(\frac{\theta}{Pr} \hat{\epsilon} Q_\eta \right)_\eta - \alpha \theta \bar{\epsilon} F_\eta^2 = 0 \quad (3.41)$$

where

$\theta = \frac{\rho u}{\rho_e u_e} = 1$ for viscosity linear with respect to temperature

$$\alpha = (\gamma-1) M_\infty^2 \frac{u_e^2}{T_e} \quad (3.42)$$

$$\beta = \frac{2\xi}{u_e} \frac{du_e}{d\xi}$$

$$V = \frac{\sqrt{2\xi}}{\rho_e u_e r^m} \left[\rho \tilde{v} + \frac{\eta_x \sqrt{2\xi} F}{r^m} \right]$$

$$F = \frac{u}{u_e}$$

$$Q = \frac{T}{T_e}$$

At $\xi = 0$ Eqs. (3.39) - (3.41) are only a function of η . Thus the leading edge singularity in the x-momentum equation has been alleviated. This is associated with the term $2\xi F F_\xi$. No knowledge of the derivative F_ξ is required since the term drops out at $\xi = 0$.

$$\xi = 0 \quad (x = 0)$$

$$V_\eta + F = 0 \quad (3.43)$$

$$VF_\eta - (\theta F_\eta)_\eta + \beta(F^2 - Q) \quad (3.44)$$

$$VQ_\eta - \left(\frac{\theta}{Pr} Q\right)_\eta - \alpha\theta F_\eta^2 = 0 \quad (3.45)$$

At $\xi = 0$, two possible cases exist for β . The first case is for zero pressure gradient at the leading edge or uniform flow.

$$\xi = 0$$

$$u_e = 1 \quad (3.46)$$

$$\beta = \frac{2\xi}{u_e} \frac{du_e}{d\xi} = 0$$

The second case is for the leading edge stagnation point.

$$\xi = 0$$

$$u_e = 0 \quad (3.47)$$

$$\alpha = 0$$

$$\beta = \frac{2\xi}{u_e} \frac{du_e}{d\xi} \rightarrow 1$$

Equations (3.43) - (3.47) can be used to generate the required initial profile for the solution of the boundary layer equations. The boundary conditions for these equations are,

$$\text{At } \eta = 0$$

$$F = 0; \quad V = 0; \quad Q = Q_w(\xi) \quad (3.48)$$

$$\text{As } \eta \rightarrow \infty$$

$$F = 1; \quad Q = 1$$

Equations (3.39) through (3.41) can be further simplified if the assumption of adiabatic work-free flow can be utilized. This is the typical case for compressor stators, and for axial flow compressor rotors when relative velocities are used. Then the energy equation can be combined with the x-momentum equation. The continuity equation remains unchanged.

First investigate the following term in the x-momentum equation.

$$\beta(F^2 - Q) = \frac{2\xi}{u_e} \frac{du_e}{d\xi} \left(\left(\frac{u_e}{T_e} \right)^2 - \frac{T_e}{T_e} \right)$$

The edge velocity can be expressed in terms of the Mach number as

$$u_e = M_e \sqrt{\gamma R T_e}$$

where

γ - ratio of specific heats

R - gas constant

Thus

$$\beta^2(F^2 - Q) = \frac{2\xi}{M_e \sqrt{\gamma R T_e}} \left[\sqrt{\gamma R T_e} \frac{dM_e}{d\xi} + \frac{M_e \sqrt{\gamma R}}{2\sqrt{T_e}} \frac{dT_e}{d\xi} \right] \cdot \left(F^2 - \frac{T_e}{T_e} \right) \quad (3.49)$$

From the energy equation for adiabatic work free flow, the stagnation enthalpy is a constant. Thus for an ideal gas with constant specific heat,

$$C_p T_e + \frac{1}{2} u_e^2 = \text{const.} \quad (3.50)$$

Thus

$$\frac{dT_e}{d\xi} = - \frac{u_e}{C_p} \frac{du_e}{d\xi}$$

Introducing the Mach number and rearranging gives

$$\frac{dT_e}{d\xi} = - \frac{2 M_e \gamma R T_e}{2 C_p + M_e^2 \gamma R} \frac{dM_e}{d\xi} \quad (3.51)$$

Substituting Eq. (3.51) into Eq. (3.49) gives,

$$\beta^2 (F^2 - Q) = \left\{ \frac{2\xi}{M_e} \frac{dM_e}{d\xi} - \frac{2 \xi M_e \gamma R}{2 C_p + M_e^2 \gamma R} \frac{dM_e}{d\xi} \right\} \cdot \left(F^2 - \frac{T}{T_e} \right) \quad (3.52)$$

Introducing a modified pressure gradient term

$$\beta' = \frac{2\xi}{M_e} \frac{dM_e}{d\xi} \quad (3.53)$$

gives

$$\beta^2 (F-Q) - \beta' \left[1 - \frac{M_e^2 \gamma R}{2 C_p + M_e^2 \gamma R} \right] \left(F^2 - \frac{T}{T_e} \right) \quad (3.54)$$

For adiabatic work free flow

$$C_p T + \frac{1}{2} u^2 = C_p T_e + \frac{1}{2} u_e^2 \quad (3.55)$$

or

$$\frac{T}{T_e} = 1 + \frac{1}{2} \frac{M_e^2 \gamma R}{C_p} [1 - F^2] \quad (3.56)$$

Substituting Eq. (3.56) into Eq. (3.54) gives

$$\beta (F^2 - Q) = \beta' (F^2 - 1) \quad (3.57)$$

for adiabatic work-free flow.

Thus the ξ -momentum equation becomes

$$2\xi F F_{\xi} + V F_{\eta} - (\theta \bar{\varepsilon} F_{\eta})_{\eta} + \beta'(F^2 - 1) = 0 \quad (3.58)$$

3.2. Turbulent Transport Models

The turbulent boundary layer is treated as a composite layer consisting of a laminar viscous sublayer very near the wall, an inner region and an outer layer.

For the inner region, the eddy viscosity model is based on a Prandtl mixing length concept. The eddy viscosity for this region as referred to the molecular viscosity is expressed as

$$\left(\frac{\varepsilon}{\mu}\right)_i = \frac{\rho \ell^2}{\mu} \left| \frac{\partial u}{\partial y} \right| \quad (3.59)$$

where ℓ is the mixing length. For the inner region the mixing length is given by the Van Driest correction with a damped law of the wall. Then

$$\ell = k_1 y [1 - \exp(-\frac{y}{A})] \quad (3.60)$$

where

$$\begin{aligned} k_1 &= .41 \\ A &= 26 \nu \left(\frac{\omega}{\rho}\right)^{-1/2} \end{aligned} \quad (3.61)$$

Cebeci and Smith [52] give a pressure gradient correction for application to both incompressible and compressible turbulent boundary layers

as

$$A = 26 \frac{\nu}{N} (\tau_w/\rho)^{-1/2} \quad (3.62)$$

where

$$N = (1 - 11.8 p^+)^{1/2}$$

$$p^+ = - \frac{\nu u_e}{(\tau_w/\rho)^{3/2}} \frac{du_e}{dx} \quad (3.63)$$

For the outer layer, one of two models may be used. Cebeci and Smith suggest a constant value given by

$$\left(\frac{\epsilon}{\mu}\right)_o = K_2 u_e \delta_{inc}^* \quad (3.64)$$

where

$$K_2 = .0168$$

and δ_{inc}^* is the incompressible displacement thickness.

The cutoff point between the inner and outer layer is given by simply checking the magnitudes of the eddy viscosities calculated by Eqs. (3.59) and (3.64). At the point where

$$\left(\frac{\epsilon}{\mu}\right)_i = \left(\frac{\epsilon}{\mu}\right)_o$$

the outer layer model will be used. Another model presented by Spalding and Patankar [53] suggests that the mixing length is constant in the outer region. Then in the inner region,

$$\left(\frac{\epsilon}{\mu}\right)_o = \frac{\rho l^2}{\mu} \left| \frac{\partial u}{\partial y} \right| \quad (3.65)$$

with

$$l = .09 \delta = \text{constant} \quad (3.66)$$

where

δ = boundary layer thickness.

The criteria for the inner and outer regions is set by the mixing length. If the mixing length given by Eq. (3.60) is greater than the mixing length given by Eq. (3.66), then the outer layer model will be employed.

Now to express the eddy viscosity relationships in the Levy-Lees variables.

For the inner layer without the pressure correction

$$\frac{Y}{A} = Re^{1/4} \frac{\rho_e u_e \bar{y}}{26 \theta Q^2 \mu_e} \left(\frac{\theta_w Q_w \mu_e}{\sqrt{2\xi}} \left(\frac{\partial F}{\partial \eta} \right)_w \right)^{1/2} \quad (3.67)$$

The pressure correction N is related to the p^+ term given by Eq. (3.66), nondimensionalizing gives

$$p^+ = \frac{\rho_e u_e \mu_e}{R_e u_\tau^3} \frac{du_e}{dx} \quad (3.68)$$

for the physical plane.

The subscript w represents the wall value, and \bar{y} is the stretched coordinate in the physical plane. The mixing length is

$$\ell = \frac{.41 \bar{y}}{Re^{1/2}} (1 - \exp(-\frac{Y}{A})) \quad (3.69)$$

Also Eq. (3.59) becomes

$$\left(\frac{\epsilon}{\mu}\right)_i = \frac{Re^{3/2} \ell^2 u_e^2}{Q \mu_e \sqrt{2\xi}} \left| \frac{\partial F}{\partial \eta} \right| \quad (3.70)$$

For the outer layer Eq. (3.64) becomes

$$\left(\frac{\epsilon}{\mu}\right)_o = Re K_2 \frac{\rho_e u_e}{\mu_e \theta Q^2} \delta_{inc}^* \quad (3.71)$$

with

$$\delta_{inc}^* = \frac{1}{Re^{1/2}} \int_0^\infty (1 - F) \frac{\sqrt{2\xi} Q}{\rho_e u_e} d\eta$$

The model in the outer layer based on the mixing length will be given by Eq. (3.70) with the appropriate mixing length.

3.2.1 Transition from Laminar to Turbulent Flow

For the case of two-dimensional boundary layers, the transition region can be satisfactorily calculated by using several empirical correlations. One such correlation for natural transition on flat plates and airfoils was proposed by Cebeci [54].

This correlation is given by

$$Re_{\theta, tr} = 1.174 [1 + 22400/Re_x] Re_x^{0.46} \quad (3.72)$$

where Re_θ is the Reynolds number based on the momentum thickness and Re_x is the Reynolds number based on the distance along the body from the initial station.

Transition is assumed to occur instantaneously. This is based on a study by Kwon and Pletcher [55]. Several models involved with the extent of the transition region were investigated and the calculated velocity profiles were compared with experimental data. The model showing the best agreement with the experimental data was with instantaneous transition from laminar to turbulent flow.

The above discussion is for natural transition. For regions where flow separation is encountered immediate transition from laminar to turbulent flow is assumed.

3.3 Formulation of the Finite Difference Representation of the Compressible Boundary Layer Equations

In order to ensure stability, the finite difference expressions will be based on an implicit calculation scheme which will allow variable grid spacing in both the marching and wall normal directions. The boundary layer equations given by Eqs. (3.39) through (3.41) are nonlinear.

Consider the term VF_η found in the x momentum equation, Eq. (3.40). The term is non-linear since neither V nor F_η is known. To solve the compressible boundary layer equations, the non-linear terms must be linearized and an iterative approach taken. A Newton-Raphson linearization technique will be utilized. The following approximation is made.

$$V = \bar{V} + \Delta V$$

$$F_\eta = \bar{F}_\eta + \Delta F_\eta$$

where

\bar{V}, \bar{F}_η - previous estimate

V, F_η - current iteration

and

$$\Delta V = V - \bar{V}$$

Therefore

$$V F_\eta = \bar{V} \bar{F}_\eta + \Delta F_\eta \bar{V} + \Delta V \bar{F}_\eta + \Delta V \Delta F_\eta$$

The assumption is made that the square of a change is small in comparison to the other terms. Therefore,

$$V F_\eta \approx \bar{V} \bar{F}_\eta + \Delta F_\eta \bar{V} + \Delta V \bar{F}_\eta$$

or

$$V F_\eta \approx \bar{V} F_\eta + V \bar{F}_\eta - \bar{V} \bar{F}_\eta \quad (3.73)$$

From a Taylor series expansion, F_η can be represented as

$$\left(\frac{\partial F}{\partial \eta}\right)_j^i \approx \frac{F_{j+1}^i - F_{j-1}^i}{\eta_{j+1} - \eta_{j-1}} \quad (3.74)$$

The i notation is associated with the streamwise direction and the j notation with the direction normal to the wall. Equation (3.74) and the expressions to follow will be 2nd order accurate for equal grid spacing in the normal direction. Now to account for large gradients near the wall a small grid spacing would be required and if a constant grid spacing were used through the boundary layer an overwhelming number of

grid points would be required vastly increasing computer time. Therefore to maintain accuracy near the wall and reduce the computing time a variable grid spacing will be required. This will cause a slight increase in truncation error. However if the grid spacing in the η direction should vary smoothly essentially 2nd order accuracy will be maintained. The following limitations were imposed;

$$\frac{\Delta\eta_{j+1}}{\Delta\eta_j} = r \quad \begin{array}{l} r < 1.05 \text{ for laminar flow} \\ < 1.02 \text{ for turbulent flow} \end{array}$$

where

$$\Delta\eta_j = \eta_j - \eta_{j-1}$$

Also at the wall

$$\begin{array}{ll} \Delta\eta_1 \approx .05 & \text{laminar flow} \\ \Delta\eta_1 \approx 10^{-3} & \text{turbulent flow.} \end{array}$$

Equation (3.74) can also be expressed as

$$\left(\frac{\partial F}{\partial \eta}\right)_j^i = \frac{F_{j+1}^i - F_{j-1}^i}{\Delta\eta_{j+1} + \Delta\eta_j}$$

The term $\frac{\partial}{\partial \eta} \left(\theta \bar{\varepsilon} \frac{\partial F}{\partial \eta} \right)$ is given by

$$\begin{aligned} \frac{\partial}{\partial \eta} (\theta \bar{\epsilon}) \frac{\partial F}{\partial \eta} &\approx \frac{2}{\Delta} \left[\frac{(\theta \bar{\epsilon})_{j+1/2}^i}{\Delta \eta_{j+1}} (F_{j+1}^i - F_j^i) \right. \\ &\quad \left. - \frac{(\theta \bar{\epsilon})_j^i}{\Delta \eta_j} (F_j^i - F_{j-1}^i) \right] \end{aligned} \quad (3.75)$$

where

$$\Delta = \Delta \eta_j + \Delta \eta_{j+1}$$

and

$$(\theta \bar{\epsilon})_{j+1/2}^i = \frac{1}{2} [(\theta \bar{\epsilon})_{j+1}^i + (\theta \bar{\epsilon})_j^i]$$

Terms with respect to ξ are now obtained. F_ξ can be given by the following 2nd order polynomial expression

$$(F_\xi)_j^i = a_0^i F_j^i + a_1^i F_j^{i-1} + a_2^i F_j^{i-2} \quad (3.76)$$

where

$$\begin{aligned} a_0^i &= \frac{1}{\xi_i - \xi_{i-2}} + \frac{1}{\xi_i - \xi_{i-1}} \\ a_1^i &= - \left(\frac{\xi_i - \xi_{i-2}}{\xi_i - \xi_{i-1}} \right) \left(\frac{1}{\xi_{i-1} - \xi_{i-2}} \right) \\ a_2^i &= \left(\frac{\xi_i - \xi_{i-1}}{\xi_i - \xi_{i-2}} \right) \left(\frac{1}{\xi_{i-1} - \xi_{i-2}} \right) \end{aligned}$$

Substituting Eqs. (3.73) - (3.74) into Eq. (3.40) gives,

$$\begin{aligned}
& 2\xi_i F_j^i (a_0^i F_j^i + a_1^i F_j^{i-1} + a_2^i F_j^{i-2}) \\
& + \overline{V}_j^i \left(\frac{F_{j+1}^i - F_{j-1}^i}{\Delta} \right) + \overline{V}_j^i \left(\frac{\overline{F}_{j+1}^i - \overline{F}_{j-1}^i}{\Delta} \right) \\
& - \overline{V}_j^i \left(\frac{\overline{F}_{j+1}^i - \overline{F}_{j-1}^i}{\Delta} \right) - \frac{2}{\Delta} \left[\frac{(\overline{\theta\varepsilon})_{j+1/2}^i}{\Delta\eta_{j+1}} (F_{j+1}^i - F_j^i) \right. \\
& \quad \left. - \frac{(\overline{\theta\varepsilon})_{j-1/2}^i}{\Delta\eta_j} (F_j^i - F_{j-1}^i) \right] \\
& + \beta^i [2 \overline{F}_j^i F_j^i - (\overline{F}_j^i)^2 - \overline{Q}_j^i] = 0 \tag{3.77}
\end{aligned}$$

Note the term $a_0^i (F_j^i)^2$ in Eq. (3.77). This term can be linearized by the Newton-Raphson technique as

$$a_0^i (F_j^i)^2 = a_0^i [2 \overline{F}_j^i F_j^i - (\overline{F}_j^i)^2] \tag{3.78}$$

Substituting Eq. (3.78) into Eq. (3.77) and collecting terms gives,

$$-A_j F_{j-1} + B_j F_j - C_j F_{j+1} + a_j V_j = D_j \tag{3.79}$$

The coefficients are given by,

$$A_j = -\frac{1}{\Delta} \left[-\overline{V}_j^i - \frac{2(\overline{\theta\varepsilon})_{j-1/2}^i}{\Delta\eta_j} \right] \tag{3.80}$$

$$\begin{aligned}
B_j = & 4\xi_i a_o^i \overline{F_j^i} + 2\xi_i (a_1^i F_j^{i-1} + a_2^i F_j^{i-2}) \\
& + \frac{2}{\Delta} \left[\frac{(\overline{\theta\varepsilon})_{j+1/2}^i}{\Delta\eta_{j+1}} + \frac{(\overline{\theta\varepsilon})_{j-1/2}^i}{\Delta\eta_j} \right] + 2\beta^i \overline{F_j^i}
\end{aligned} \tag{3.81}$$

$$C_j = -\frac{\overline{V_j^i}}{\Delta} + \frac{2}{\Delta} \frac{(\overline{\theta\varepsilon})_{j+1/2}^i}{\Delta\eta_{j+1}} \tag{3.82}$$

$$a_j = \frac{\overline{F_{j+1}^i} - \overline{F_{j-1}^i}}{\Delta} \tag{3.83}$$

$$\begin{aligned}
D_j = & 2\xi_i (\overline{F_j^i})^2 a_o^i + \overline{V_j^i} \left(\frac{\overline{F_{j+1}^i} - \overline{F_{j-1}^i}}{\Delta} \right) \\
& + \beta^i (\overline{F_j^i})^2 + \beta^i \overline{Q_j^i}
\end{aligned} \tag{3.84}$$

To solve Eq. (3.77) $\overline{V_j^i}$ must be known. This can be obtained from the continuity equation

$$2\xi F_\xi + V_\eta + F = 0 \tag{3.39}$$

A centered difference expression, about the point i,j , can not be used as this would only couple the odd and even points possibly leading to an incorrect solution. However, 2nd order accurate expressions can be obtained by writing

$$(v_n)^i_{j-1/2} = \frac{v_j^i - v_{j-1}^i}{\Delta \eta_j} \quad (3.85)$$

$$(F_\xi)^i_{j-1/2} = \frac{1}{2} [(F_\xi)^i_j + (F_\xi)^i_{j-1}] \quad (3.86)$$

$$F_{j-1/2}^i = \frac{1}{2} (F_j + F_{j-1}) \quad (3.87)$$

Substituting Eqs. (3.85) - (3.87) into Eq. (3.39) gives

$$v_j^i = v_{j-1}^i - c_j^i (F_j^i + F_{j-1}^i) + d_j^i \quad (3.88)$$

where

$$c_j = \Delta \eta_j \xi^i \left[a_0^i + \frac{1}{2\xi} \right] \quad (3.89)$$

$$d_j = -\Delta \eta_j \xi_i \left[a_1^i (F_j^{i-1} + F_{j-1}^{i-1}) + a_2^i (F_j^{i-2} + F_{j-1}^{i-2}) \right] \quad (3.90)$$

Finally to obtain an expression for the energy equation.

$$2\xi F Q_\xi + v Q_n - \left(\frac{\theta}{Pr} \hat{\epsilon} Q_n \right)_n - \alpha \theta \bar{\epsilon} F_n^2 = 0 \quad (3.41)$$

The finite difference representations are now presented.

$$\frac{\partial}{\partial \eta} \left(\frac{\theta}{Pr} \hat{\varepsilon} \frac{\partial Q}{\partial \eta} \right) = \frac{2}{\Delta} \left[\frac{(\hat{\theta\varepsilon}/Pr)_{j+1/2}}{\Delta \eta_{j+1}} (Q_{j+1}^i - Q_j^i) \right] - \frac{(\hat{\theta\varepsilon}/Pr)_{j-1/2}}{\Delta \eta_j} (Q_j^i - Q_{j-1}^i) \quad (3.91)$$

$$(Q_\eta)_j^i = \frac{Q_{j+1}^i - Q_{j-1}^i}{\Delta \eta_{j+1} + \Delta \eta_j} \quad (3.92)$$

and

$$Q_\xi = a_0^i Q_j^i + a_1^i Q_j^{i-1} + a_2^i Q_j^{i-2} \quad (3.93)$$

Substituting Eqs. (3.74), (3.91), (3.92) and (3.93) into Eq. (3.41) gives

$$\bar{A}_j Q_{j-1} + \bar{B}_j Q_j + \bar{C}_j Q_{j+1} = \bar{D}_j \quad (3.94)$$

where

$$\bar{A}_j = - \left[\frac{v_j^i}{\Delta} + \frac{2}{\Delta} \frac{(\hat{\theta\varepsilon}/Pr)_{j-1/2}}{\Delta \eta_j} \right] \quad (3.95)$$

$$\bar{B}_j = 2\xi_i F_j^i a_0^i + \frac{2}{\Delta} \left[\frac{(\hat{\theta\varepsilon}/Pr)_{j+1/2}}{\Delta \eta_{j+1}} + \frac{(\hat{\theta\varepsilon}/Pr)_{j-1/2}}{\Delta \eta_j} \right] \quad (3.96)$$

$$\bar{C}_j = - \left[\frac{2}{\Delta} \frac{(\hat{\theta\varepsilon}/Pr)_{j+1/2}}{\Delta \eta_{j+1}} - \frac{v_j^i}{\Delta} \right] \quad (3.97)$$

and

$$\begin{aligned} \bar{D}_j = & - 2\xi_i F_j^i (a_1^i Q_j^{i-1} + a_2^i Q_j^{i-2}) \\ & + \alpha^i (\theta \varepsilon)_j^i \left(\frac{F_{j+1}^i - F_{j-1}^i}{\Delta} \right)^2 \end{aligned} \quad (3.98)$$

3.4. Direct Mode Calculation Technique

With the pressure gradient β specified, Eqs. (3.78), (3.88), and (3.94) can be solved following an L-U decomposition of the resulting matrix. The scheme is as follows:

for $j = 2, N-1$

$$F_j = E_j F_{j-1} + G_j V_{j-1} + H_j \quad (3.99)$$

$$V_j = V_{j-1} - c_j (F_j + F_{j-1}) + d_j$$

At $j = 1$ the solution is known from the boundary conditions.

$$F_j^i = V_j^i = 0 \quad (3.100)$$

At $j = N$

$$F_N = E_N F_{N-1} + G_N V_{N-1} + H_N = 1$$

Thus

$$E_N = 0$$

$$G_N = 0$$

$$H_N = 1$$

E_j, H_j, G_j are defined as follows,

$$E_j = [A_j - c_j (C_j G_{j+1} - a_j)]/P$$

$$G_j = [C_j G_{j+1} - a_j]/P \quad (3.101)$$

$$H_j = [D_j + (C_j G_{j+1} - a_j)d_j + C_j H_{j+1}]/P$$

with

$$P = B_j - C_j E_{j+1} + c_j (C_j G_{j+1} - a_j) \quad (3.102)$$

The coefficients will be calculated for $j = N-1, \dots, 1$ where N is the number of grid points in the η direction. Once the coefficients are defined, Eq. (3.99) will be used to calculate the velocity distribution in the boundary layer. This will then be used as input for the solution of the energy equation. From Eq. (3.94) the energy equation is

for $j = 3, N-2$

$$\bar{A}_j Q_{j-1} + \bar{B}_j Q_j + \bar{C}_j Q_{j+1} = \bar{D}_j \quad (3.94)$$

At $j = 2$

$$Q_{j-1} = T_w$$

and

$$\bar{B}_2 Q_2 + \bar{C}_2 Q_3 = \bar{D}_2 - T_w \bar{A}_2 \quad (3.103)$$

At $j = N-1$

$$Q_N = 1$$

$$\bar{A}_{N-1} Q_{N-2} + \bar{B}_{N-1} Q_{N-1} = D_{N-1} - C_{N-1} \quad (3.104)$$

Equations (3.94), (3.103), (3.104) are solved using a tridiagonal equation solver.

Once the solution to the energy equations is obtained the new values for Q will be used as input to the momentum and continuity equations. This iteration procedure will continue until the average change in F based on the 2 norm is 5×10^{-4} or less.

3.5 Inverse Mode Calculation Technique

3.5.1 Introduction

Whenever the pressure gradient becomes adverse, as is the case in a compressor rotor, the skin friction decreases and may eventually become zero and the flow will separate from the wall. It is well known that many numerical methods for solving the boundary layer equations encounter difficulties when the flow separates from the body surface. The relevant common feature of these methods is the prescription of the pressure as a boundary condition (direct method). It has been shown by Goldstein [56,57] that apart from exceptional circumstances, this will lead to a singularity in the solution, causing the breakdown of the numerical method.

Catherall and Mangler [24] were the first to realize that relaxing the pressure would lead to regular solutions of the boundary layer equations at separation. By prescribing the displacement thickness as a boundary condition, they were able to integrate the boundary layer equations through the separation point and into a region of reverse flow without evidence of singular behavior at the separation point.

3.5.2 Calculation Procedure

The calculation procedure will be presented for the case of adiabatic flow.

First define a stream function as follows;

$$F = \frac{\partial f}{\partial \eta} = \frac{u}{u_e} \quad (3.105)$$

where

f = stream function

The continuity equation is given by Eq. (3.39). Substituting Eq. (3.105) into Eq. (3.39) gives

$$2\xi \frac{\partial}{\partial \xi} \left(\frac{\partial f}{\partial \eta} \right) + \frac{\partial f}{\partial \eta} + \frac{\partial V}{\partial \eta} = 0 \quad (3.106)$$

Rearranging Eq. (3.106) and integrating with respect to η gives for the continuity equation;

$$V(\eta) = - 2\xi \frac{\partial f}{\partial \eta} - f(\eta) = \sqrt{2\xi} \frac{\partial}{\partial \xi} (\sqrt{2\xi} f) \quad (3.107)$$

From Eq. (3.105)

$$F = f_{\eta}$$

This is modelled by a second order accurate centered difference expression about the point $j - 1/2$

$$(f_{\eta})_{j-1/2}^i = \frac{f_j^i - f_{j-1}^i}{\Delta \eta_j} = F_{j-1/2}^i \quad (3.108)$$

From an average operator

$$F_{j-1/2}^i = \frac{1}{2} (F_j^i + F_{j-1}^i)$$

Therefore Eq. (3.108) becomes

$$f_{j-1}^i - f_j^i + \frac{\Delta \eta_j}{2} (F_{j-1}^i + F_j^i) = 0$$

Let

$$b_j = \frac{\Delta \eta_j}{2}$$

Then

$$f_{j-1}^i - f_j^i + b_j (F_{j-1}^i + F_j^i) = 0 \quad (3.109)$$

This will be used to calculate the stream function.

Now to obtain the finite difference form of the energy equation. For the case of separated or reverse flow the FLARE approximation [58] will be used. For small regions of separated flow the convection term in the momentum equation is neglected. This will give acceptable results for cases where the reverse flow velocity is less than 10% of the freestream value.

In the Levy Lees variables, the term $2\xi F F_\xi$ in the momentum equation will be approximated as;

$$2\xi F F_\xi = 2 \lambda \xi F F_\xi$$

where

$$\lambda = 0 \quad F < 0$$

$$\lambda = 1 \quad F > 0$$

Thus the momentum equation becomes

$$2\xi \lambda F F_\eta + V F_\eta - (\theta \bar{\varepsilon} F_\eta)_\eta + \beta(F^2 - 1) = 0 \quad (3.110)$$

The nonlinear terms are linearized with Newton-Raphson linearization as before. However, the stream function is introduced by the continuity equation, Eq. (3.107). The modified velocity V is given in terms of the stream function by the following 2nd order finite difference equation;

$$V_j^i = -2\xi^i (2 a_0^i f_j^i + a_1^i f_j^{i-1} + a_2^i f_j^{i-2}) - f_j^i \quad (3.111)$$

Therefore the linearized form of $V F_\eta$ becomes

$$\begin{aligned} V F_\eta &= \bar{V}_j^i \left(\frac{F_{j+1}^i - F_{j-1}^i}{\Delta \eta_{j+1} + \Delta \eta_j} \right) \\ &+ [-2\xi^i (a_0^i f_j^i + a_1^i f_j^{i-1} + a_2^i f_j^{i-2}) - f_j^i] \left(\frac{\bar{F}_{j+1}^i - \bar{F}_{j-1}^i}{\Delta \eta_{j+1} + \Delta \eta_j} \right) \\ &- \bar{V}_j^i \left(\frac{\bar{F}_{j+1}^i - \bar{F}_{j-1}^i}{\Delta \eta_{n+1} + \Delta \eta_j} \right) \end{aligned} \quad (3.112)$$

The other linearizations follow as before.

The following expression results;

$$A_j F_{j-1}^i + B_j F_j^i + C_j F_{j+1}^i + D_j f_j^i = E_j \beta^i + G_j \quad (3.113)$$

The definition of the coefficients are as follows;

$$A_j = \frac{-\bar{V}_j^i}{\Delta} - \frac{2}{\Delta} \frac{\theta_{j-1/2}^i \bar{\epsilon}_{j-1/2}^i}{\Delta \eta_j} \quad (3.114)$$

$$\begin{aligned} B_j &= 4 \lambda \xi^i a_o^i \bar{F}_j^i + 2 \lambda \xi^i (a_1^i F_j^{i-1} + a_2^i F_j^{i-2}) \\ &+ \frac{2}{\Delta} \left[\frac{\theta_{j+1/2}^i \bar{\epsilon}_{j+1/2}^i}{\Delta \eta_{j+1}} + \frac{\theta_{j-1/2}^i \bar{\epsilon}_{j-1/2}^i}{\Delta \eta_j} \right] + 2 \bar{\beta}^i \bar{F}_j^i \end{aligned} \quad (3.115)$$

$$C_j = \frac{\bar{V}_j^i}{\Delta} - \frac{2}{\Delta} \frac{\theta_{j+1/2}^i \bar{\epsilon}_{j+1/2}^i}{\Delta \eta_{j+1}} \quad (3.116)$$

$$D_j = [-2 \xi^i a_o^i - 1] \left(\frac{\bar{F}_{j+1}^i - \bar{F}_{j-1}^i}{\Delta} \right) \quad (3.117)$$

$$E_j = -(\bar{F}_j^i)^2 - 1 \quad (3.118)$$

$$\begin{aligned} G_j &= 2 \lambda \xi^i a_o^i \bar{F}_j^i{}^2 + 2 \xi^i (a_1^i f_j^{i-1} + a_2^i f_j^{i-2}) \left(\frac{\bar{F}_{j+1}^i - \bar{F}_{j-1}^i}{\Delta} \right) \\ &+ \bar{V}_j^i \left(\frac{\bar{F}_{j+1}^i - \bar{F}_{j-1}^i}{\Delta} \right) + 2 \bar{\beta}^i \bar{F}_j^i{}^2 \end{aligned} \quad (3.119)$$

Thus the equations for the stream function and momentum coupled with

continuity are

$$f_{j-1}^i - f_j^i + b_j(F_{j-1}^i + F_j^i) = 0 \quad (3.109)$$

$$A_j F_{j-1}^i + B_j F_j^i + C_j F_{j+1}^i + D_j f_j^i = E_j \beta^i + G_j \quad (3.113)$$

The solution to Eqs. (3.109) and (3.113) is obtained through a L-U decomposition. Here one of the unknowns is the pressure gradient and the outer boundary condition is unspecified. However the blocks below the main diagonal can be eliminated and a recursion formula developed for back substitution. The unknowns can be computed as

$$F_j^i = A_j' F_{j+1}^i + B_j' \beta^i + C_j' \quad (3.120)$$

$$f_j^i = D_j' F_{j+1}^i + E_j' \beta^i + G_j' \quad (3.121)$$

The coefficients are defined as

$$A_j' = -C_j/R_1 \quad (3.122)$$

$$B_j' = \frac{E_j - A_j B_{j-1}' - D_j (b_j B_{j-1}' + E_{j-1}')}{R_1} \quad (3.123)$$

$$C_j' = \frac{G_j - A_j C_{j-1}' - D_j (b_j C_{j-1}' + G_{j-1}')}{R_1} \quad (3.124)$$

$$D_j' = A_j' R_2 \quad (3.125)$$

$$E'_j = b B'_{j-1} + E'_{j-1} + B'_j R_2 \quad (3.126)$$

$$G'_j = b_j C'_{j-1} + G'_{j-1} + C'_j R_2 \quad (3.127)$$

with

$$\begin{aligned} R_1 &= B_j + (A_j + D_j b_j) A'_{j-1} + D_j (D'_{j-1} + b_j) \\ R_2 &= b_j (1 + A'_{j-1}) + D'_{j-1} \end{aligned}$$

At the wall ($j=1$) the boundary conditions are

$$F_1^i = 0$$

$$f_1^i = 0 \quad (3.128)$$

The boundary condition therefore gives the following values for the coefficients at the wall;

$$A'_1 = B'_1 = D'_1 = E'_1 = G'_1 = 0 \quad (3.129)$$

The coefficients are computed starting at $j=2$ and continued to the boundary layer edge at $j = NJ$.

The pressure gradient β is calculated by solving Eqs. (3.120) and (3.121) at $j = NJ-1$ along with the following outer boundary condition. The value of the stream function at the edge is given by

$$f_e = f_{NJ}^i = \int_0^{y_e} F \, dn \quad (3.130)$$

The displacement thickness is given by

$$\delta^* = \frac{\sqrt{2\xi}}{\rho_e u_e} \int_0^{\infty} (Q - F) d\eta$$

At $y > y_e$ $(Q - F) = 0$, thus

$$\delta^* = \frac{\sqrt{2\xi}}{\rho_e u_e} \int_0^{y_e} Q d\eta - \frac{\sqrt{2\xi}}{\rho_e u_e} f_e \quad (3.131)$$

Solving for f_e

$$f_e = f_{NJ}^i = \int_0^{\eta_e} Q d\eta - \frac{\rho_e u_e \delta^*}{\sqrt{2\xi}} \quad (3.132)$$

This is the additional required boundary if $\frac{\rho_e u_e \delta^*}{\sqrt{2\xi}}$ is specified.

The $\int_0^{\eta_e} Q d\eta$ can be approximated with a trapezoidal integration scheme. Substituting Eq. (3.132) into Eq. (3.121) gives

$$f_{NJ} = QI - \frac{\rho_e u_e \delta^*}{\sqrt{2\xi}} = f_{NJ-1}^i + \frac{\Delta\eta_i}{2} (F_{NJ-1}^i + F_{NJ}^i) \quad (3.133)$$

where

$$QI = \int_0^{\eta_e} Q d\eta$$

Rearranging Eq. (3.133), substituting into Eq. (3.121) and solving for β gives

$$E'_{NJ-1} \beta^i = QI - \frac{\rho_e u_e \delta^*}{\sqrt{2} \xi} - \frac{\Delta \eta_j}{2} (A'_{NJ-1} F'_{NJ} + B'_{NG-1} \beta^i + C'_{NJ-1} + F'_{NJ})$$

$$(3.134)$$

$$- D'_{NJ-1} F'_{NJ} - G'_{NJ-1}$$

Substituting for F'_{NJ-1} from Eq. (3.120) along with the boundary condition that $F'_{NJ} = 1$ gives

$$\beta^i = \left[QI - \frac{\rho_e u_e \delta^*}{\sqrt{2} \xi} - \frac{\Delta \eta_{NJ}}{2} (A'_{NJ-1} + C'_{NJ-1} + 1) \right. \\ \left. - D'_{NJ-1} - G'_{NJ-1} \right] / \left(E'_{NJ-1} + \frac{\Delta \eta_{NJ}}{2} B'_{NJ-1} \right)$$

$$(3.135)$$

Once the pressure gradient is known the edge Mach number will be calculated and ρ_e , T_e , u_e and ξ will be updated.

The solution of Eqs. (3.109) and (3.113) will then proceed from $j = NJ-1$ to $j = 2$. The new temperature distribution is calculated from the velocity profile for the condition of adiabatic flow and the modified velocity V is calculated from Eq. (3.111). The iteration procedure is continued until the average change in F based on the 2 norm is less than 10^{-4} and the "boundary layer mass flux" $\frac{\rho_e u_e \delta^*}{\sqrt{2} \xi}$ is matched within a specified tolerance. Note two checks must be made here, one on F and one on the "boundary layer mass flux". This increases the number of iterations and the computer time to obtain a converged solution. It should be noted that a new edge velocity based on the viscous solution was calculated. This in general will not be the same as the inviscid edge velocity. For a consistent solution the viscous and inviscid field

must be matched. This matching procedure will be discussed under the section on viscous-inviscid interactions.

3.6 Viscous-Inviscid Calculation Procedure

3.6.1 Introduction

Two computational techniques have been presented for predicting compressible boundary layer flow. The direct method which involves specifying a pressure or inviscid edge Mach number distribution and an inverse method where a boundary mass flux was specified and the resulting pressure gradient calculated. The direct method performs well for attached boundary layers where the interaction between the viscous and inviscid flow field is "weak", i.e., the viscous effect on the surface pressure is small and the complete flow field can be solved sequentially. However, the flow over a turbine or compressor blade involves both the weak interaction due to standard displacement effects and local "strong" viscous inviscid interaction effects. In particular, near an airfoil-trailing edge strong interactions occur from separation of the viscous layer from the airfoil surface, and from the abrupt change in the no slip condition that the boundary layer experiences at the point of separation or termination of the airfoil surface and into the wake. These conditions lead to singularities in a classical boundary layer solution and a subsequent breakdown of the weak interaction or direct method approach. This leads to the inverse method where the displacement thickness or "boundary layer mass flux" must be specified. A problem associated with this technique is that the boundary layer mass flux is not known a priori. The appropriate value has to be obtained as

part of the overall problem from the interaction, the boundary layer and inviscid flow. Near separation and near the trailing edge, there no longer exists a definite hierarchy between the boundary layer and the outer inviscid flow [34,59]. As a consequence a numerical scheme which possesses a simultaneous coupling between the viscous and inviscid parts of the flow field can have very favorable characteristics in terms of convergence for matching of the flow fields. This method is consistent with the asymptotic triple deck theory of Stewartson [60].

3.6.2 Viscous-Inviscid Matching Procedure for Subsonic Flow

The inviscid flow field is assumed to be two-dimensional, irrotational compressible flow. Therefore the initial estimate of the inviscid flow is calculated from the full potential cascade solver described in Chapter 2. This provides the edge Mach number distribution for input to the boundary layer equations for calculations in the direct mode. As the solution approaches a point of separation or the blade trailing edge, the number of iterations to obtain a converged solution increases substantially until divergence occurs. If at a particular station a converged solution is not obtained in fifty iterations or less, the direct mode is abandoned and the inverse mode is initiated specifying the boundary layer mass flux for all remaining stations. This is assumed to be the start of the strong interaction region.

The boundary layer mass flux was previously defined as

$$XMF = \frac{\rho_e u_e \delta^*}{\sqrt{2 \xi}} \quad (3.136)$$

Prior to this calculation station the interaction between the viscous and inviscid fields is assumed to be weak. Even for cases of mild separation the displacement thickness is relatively thin in actual physical dimensions. Therefore, rather than recalculating the inviscid flow field with the full potential solver with a new shape to account for the displacement thickness, it is assumed that the new velocity can be described by the initial inviscid velocity plus a perturbation velocity described by thin airfoil theory.

$$u_{e_INV}^{n+1} = u_e^o + u_c^n \quad (3.137)$$

where

- u_{e_INV} - updated inviscid edge velocity
- u_e^o - initial inviscid edge velocity
- u_c - correction to the inviscid edge velocity for displacement thickness effects
- n - iteration number to be discussed later

For subsonic flows the correction is obtained from the Hilbert integral [61]

$$u_c^n = \frac{1}{\pi} \int_{x_i}^{x_e} \frac{(u_e^o \delta^*)^n}{x - \xi} d\xi \quad (3.138)$$

with

- x_i, x_e denoting the beginning and end of the strong interaction region
- ξ dummy variable

For supersonic flow, a linearized Prandtl-Meyer relation is used [62]

$$\frac{(u_c)_x}{u_e} = (M_e^2 - 1)^{-1/2} \alpha \quad (3.139)$$

$$\alpha = \left(\frac{v}{u} \right)_{y=\delta^*} = \delta_x^*$$

For subsonic flow the discretization of Eq. (3.138) will be accomplished with mid-point integration rule.

Let

$$h(\xi) = (u_e \delta^*)_{\xi} \quad (3.140)$$

For N grid points with N-1 equal segments along the blade section the finite difference representation of Eq. (3.140) can be found from a centered difference expression as

$$h^n(\xi_{j+1/2}) = \frac{(u_{e0,j+1} \delta_{j+1}^{*n} - u_{e0,j} \delta_j^{*n})}{\Delta x} + O(\Delta x^2) \quad (3.141)$$

Further let

$$g(x, \xi) = \frac{h(\xi)}{x - \xi}$$

Then

$$g^n(x_i, \xi_{j+1/2}) = \frac{h^n(\xi_{j+1/2})}{x_i - \xi_{j+1/2}} \quad (3.142)$$

The velocity perturbation is then

$$U_c^n(x_i) = \frac{1}{\pi} \sum_{j=1}^{N-1} \Delta x_j g^n(x_i, \xi_{j+1/2}) \quad (3.143)$$

The updated inviscid edge velocity can then be calculated from Eq. (3.136). This will then be used to recalculate an inviscid edge Mach number. For computations in the inverse mode, the boundary layer mass flux was specified. The viscous edge Mach number was then calculated. In general these two Mach numbers will be different, particularly in a strong interaction zone. Therefore an iterative procedure must be developed for proper matching of the viscous and inviscid flow fields for regions of flow separation or near the blade trailing edge. The difference between the two edge Mach numbers can be used as a potential to calculate an improved value for XMF given Eq. (3.136). To do this formally would require a way to determine how a change in M_e would effect the boundary layer mass flux XMF. However, success has been achieved by noting that for small excursions in the local M_e , the response to increasing XMF was an increase in the displacement thickness δ^* . This is similar to the case of an adverse pressure gradient and M_e decreases as expected. Decreasing XMF leads to a decrease in displacement thickness δ^* and an increase in edge Mach number as is the case of a favorable pressure gradients. This concept is put into practice as follows. Having passed through the boundary layer calculation to obtain $M_{e,BL}$ and using Eq. (3.137) to calculate, $M_{e,inv}$ from $U_{e,inv}$, the new input for the inverse calculation is

$$XMF^{n+1} = XMF^n \left(\frac{M_{e,BL}^n}{M_{e,inv}^n} \right) \quad (3.144)$$

where

n - iteration number

Equation (3.144) is only used as a basis for correcting XMF and it does produce converged solutions. At convergence $M_{e,BL} = M_{e,inv}$ and Eq. (3.144) represents an identity having no effect on the nature of the final solution.

One main advantage of this method is that under-relaxation of the change from iteration can often be avoided. Under-relaxation, as used by Carter and Wornom [29], can lead to excessive computing time. The current method can use successive over relaxation which allows a drastic reduction in computing time. This is given by

$$XMF^{n+1} = XMF^n + \omega XMF^n \left(\frac{M_{e,BL}^n}{M_{e,inv}^n} - 1 \right) \quad (3.145)$$

with

ω - relaxation parameter

Typical values of the relaxation parameter are in the range of 1.4 to 1.8.

The speed of the convergence can be increased even more utilizing the quasi-simultaneous technique of Veldman [35]. The first n iterations are performed as previously stated to obtain a partially converged solution. Then at the $n+1$ th iteration the quasi-simultaneous solution will begin. The updated inviscid edge velocity is calculated by Eqs. (3.137) and (3.138). The boundary layer equations are parabolic and are marched in the flow direction, but for subsonic inviscid flow the nature is elliptic, therefore it is logical that at the $n+1$ th iteration level any new displacement thickness calculated at the $n+1$ th level should be

included in the calculation of the inviscid updated velocity. For example, consider Eq. (3.141). Assume that the strong interaction region began at $i = m$ and the boundary layer calculations have proceeded to station $i = m + 5$. The displacement thickness has now been calculated at the n th iteration level therefore it can be used in the inviscid velocity update as follows;

For $i > m$

$$u_{c.}^n = \frac{1}{\pi} \left[\sum_{j=1}^{i-1} \Delta x_j g^{n+1}(x_i, \xi_{j+1/2}) + \sum_{j=i}^{N-1} \Delta x_j g^n(x_i, \xi_{j+1/2}) \right] \quad (3.146)$$

where

$$g^{n+1}(x_i, \xi_{j+1/2}) = \frac{h^{n+1}(\xi_{j+1/2})}{x_i - \xi_{j+1/2}}$$

and

$$h^{n+1}(\xi_{j+1/2}) = \frac{(u_{e0,j+1} \delta_{j+1}^{*n+1} - u_{e0,j} \delta_j^{*n+1})}{X_{j+1} - X_j}$$

This gives even more rapid convergence of the matching procedure due to the linear combination of u_e and δ^* as the external boundary condition. The iterations are continued until the inviscid edge Mach number and the viscous edge Mach number match within a specified tolerance.

Thus the summary of the overall procedure is as follows;

1. Calculate the inviscid flow field using the full potential equations given in Chapter 1.

2. With the edge Mach number specified calculate the viscous flow field along the blade surface using the direct mode calculation procedure up to the strong interaction region.
3. Specify the boundary layer mass flux over the remaining blade surface and calculate the remaining viscous flow field.
4. Calculate the new inviscid edge Mach number utilizing thin airfoil theory to give the perturbation from the original distribution.
5. Compare the viscous and inviscid edge Mach numbers. If they match within a specified tolerance the calculation is complete. If they are outside the tolerance, respecify the mass flux and repeat steps 3, 4, and 5.

3.7 Wake Calculation Procedure

3.7.1 Turbulence Modeling

For flow over the blade surface turbulence was modelled using an eddy-viscosity, two-layer concept as described in Section 3.2. The same concept can be applied in the wake with one major exception. As the flow separates from the airfoil surface at the blade trailing edge, a rapid acceleration of the flow at the wake centerline occurs as the blade no slip condition is relaxed. This abrupt change in the surface boundary condition brings about the requirement of a new eddy viscosity model for the inner region. A concept developed by Cebeci, et al. [63] was modified for this purpose. The wake boundary layer is assumed to consist of 3 regions, an inner wake region which is part of the inner region previously defined, a new inner region and an outer region (Fig. 12). From Ref. 63 the inner wake region has the following eddy viscosi-

ty in Levy-Lees variables.

$$e = e_w = 0.4 \frac{\rho}{\rho(\eta_c)} \frac{\mu(\eta_c)}{\mu} \exp \left[\frac{u_e F(\eta_c)}{2.75 u_\tau^{T.E.}} - 2.08 \right] \quad (3.147)$$

η_c is defined as the distance from the wake centerline to the point where

$$u_{CALC}^* = 1.1 u_{log}^* \quad (3.148)$$

where

u_{CALC} is the calculated dimensional velocity and

u_{log} is given by

$$u_{log}^* = u_\tau^{*T.E.} \left[2.5 \ln \left(\frac{y^* u_\tau^{*T.E.}}{v} \right) + 5.2 \right] \quad (3.149)$$

where

$$u_\tau^{*T.E.} = \left(\frac{\mu^*}{\rho^*} \frac{\partial u^*}{\partial y^*} \right)^{1/2} \quad (3.150)$$

Nondimensionalizing and introducing Levy Lees variables gives

$$u_\tau^{T.E.} = \left[\theta_w \mu_e Q_w \frac{u_e^2}{\sqrt{2} \xi \sqrt{Re}} \frac{\partial F_w}{\partial \eta} \right]^{1/2} \quad (3.151)$$

and

$$u_{log} = u_\tau^{T.E.} \left[2.5 \ln \left(\frac{\bar{y} \sqrt{Re} u_\tau^{T.E.}}{\rho_e \mu_e} \right) + 5.2 \right] \quad (3.152)$$

For the case of linear viscosity law Eq. (3.147) becomes

$$e_w = .4 \exp\left[\frac{u_e F(\eta_c)}{2.75 u_\tau^{T.E.}} - 2.08\right] \quad (3.153)$$

For the remaining inner layer a model for the mixing length based on Spalding and Patankar model [53] rather than the model previously discussed in Section 3.2 will be used. The mixing length is still modelled as

$$l = k_1 y [1 - \exp(-y/A)]$$

with the following exceptions

$$\begin{aligned} k_1 &= .435 \\ A &= \frac{26 \nu}{N} (\tau/\rho)^{-1/2} \end{aligned} \quad (3.154)$$

where τ is the local shear stress. In the previous expression in Section 3.2 the shear stress at the wall was used. The outer layer is the same as Section 3.2 with the Spalding and Pantankar model being used. Thus the following breakdown of the eddy viscosity occurs in the wake

Inner region

For

$$e_i < e_w \quad e = e_w$$

For

$$e_i > e_w \quad e = e_i$$

Outer region

$$e = e_o$$

e_i , e_o are previously defined in Section 3.2.

At large distances from the blade trailing edge the condition may exist such that $e_w > e_o$. If this occurs it is assumed that $e = e_o$ across the entire wake.

3.7.2 Calculation Procedure

The overall wake calculation procedure is essentially the same as procedure for the blade. The calculation procedure for the wake will be the inverse mode where the boundary layer mass flux is specified. The wake centerline is assumed to be along the inviscid wake streamline as described in Chapter 2. The coordinate system is set up with the suction surface side of the wake being positive and the pressure surface side of the wake being negative. The boundary conditions at $\eta = \infty$ are the same as given in Section 3.5 for the inverse mode calculation. At the wake centerline, however, the no slip condition is no longer applicable.

At $\eta = 0$ (wake centerline)

$$\frac{\partial F}{\partial \eta} = 0 \quad (\text{symmetric wakes})$$

$$v = 0 \quad (3.155)$$

$$\frac{\partial Q}{\partial \eta} = 0$$

Also, $u_{1p} = u_{1s}$ = centerline velocity. Where u_{1s} , u_{1p} are the velocities at the wake centerline for the suction and pressure sides of the wake, respectively.

The edge velocities on the suction and pressure sides of the wake will in general be different for asymmetric wakes. Therefore in Levy Lees variables

$$F_{1P} = F_{1S} \frac{u_{es}}{u_{ep}} \quad (3.156)$$

where u_{es} , u_{ep} are the edge velocities for the suction and pressure sides of the wake, respectively.

To satisfy the boundary condition at the wake centerline, a first order forward difference expression is used.

$$\frac{F_{2S}^i - F_{1S}^i}{\Delta\eta} = 0 \quad (3.157)$$

and

$$\frac{F_{2P}^i - F_{1P}^i}{\Delta\eta} = 0 \quad (3.158)$$

Combining Eqs. (3.156), (3.157) and (3.158) gives the boundary condition for the wake centerline for symmetric wakes.

$$F_{2P} = F_{1P} = F_{1S} \frac{u_{es}}{u_{ep}} = F_{2S} \frac{u_{es}}{u_{ep}} \quad (3.159)$$

In the inverse mode the same set of equations as presented in Section 3.5 are obtained. For asymmetric wakes only, the condition that $V = 0$ is used.

Suction Side

$$F_{js}^i = A'_{js} F_{(j+1)s}^i + B'_{js} \beta_s^i + C'_{js}$$

$$f_{js}^i = D'_{js} F_{(j+1)s}^i + E'_{js} \beta_s^i + G'_{js}$$
(3.160)

Pressure Side

$$F_{jp}^i = A'_{jp} F_{(j+1)p}^i + B'_{jp} \beta_p^i + C'_{jp}$$

$$f_{jp}^i = D'_{jp} F_{(j+1)p}^i + E'_{jp} \beta_p^i + G'_{jp}$$
(3.161)

From the boundary condition given by Eq. (3.159)

$$A'_{1s} = 1$$

$$B'_{1s} = C'_{1s} = D'_{1s} = E'_{1s} = G'_{1s} = 0$$
(3.162)

and

$$A'_{1p} = 1$$

$$B'_{1p} = C'_{1p} = D'_{1p} = E'_{1p} = G'_{1p} = 0$$
(3.163)

The coefficients are computed as before starting at $j = 2$ and ending at $j = NJS$ or NJP , for the number of grid points on the suction and pressure sides of the wake, respectively. The solution for the pressure gradient on either side of the wake is as presented in Section 3.5. Finally, the calculations are made as before from the outer boundary to the inner boundary except that now the iteration will include one com-

plete sweep across the wake. The iteration procedure is continued until the average change in F across the entire wake and the boundary layer mass flux at the edges of the wake are matched with a specified tolerance. The viscous-inviscid matching procedure is identical to the procedure presented in Section 3.6.

3.8 Sample Calculations

To assess the validity of the mathematical procedure of this model, a set of numerical experiments were performed.

This first case was Howarth flow [64] where the flow experiences a severe adverse pressure gradient resulting in massive separation. The boundary layer edge velocity distribution is found in Fig. 13 with a freestream Mach number of 4. The direct calculation procedure with specified pressure gradient was used to calculate the boundary layer flow up to the point where massive separation occurs. At that point the boundary equations are no longer valid and the solution diverges. The boundary layer velocity profiles are shown at various x/c locations in Figs. 14 and 15 for laminar flow. At $x/c = 0.056$ flow separation occurred and the solution diverged. A comparison of the computed skin friction coefficient distribution with the results of Werle and Senechal [65] shows good agreement (Fig. 16). A comparison of the displacement thickness distribution for the same case also shows good agreement (Fig. 17).

The next numerical investigation employed the Gostelow compressor cascade previously discussed in Chapter 2. The Reynolds number was 100,000. The calculated Mach number distribution for the suction sur-

face is presented in Fig. 18 for the cases with and without viscous interaction with the inviscid stream. The region of strong interaction is found to be between 80% to 100% chord. It is seen that due to the increasing boundary layer thickness near the trailing edge the rapid deceleration found in the inviscid calculation is not present. At the blade trailing edge, the Mach number for the viscous-inviscid interaction calculation is 0.075 compared to 0.066 for in inviscid case. The boundary layer development along the blade suction surface can be seen in Figs. 19 through 28. At 40% chord (Fig. 19) the velocity profile is good in terms of no separation. Due to the adverse pressure gradient, however, the fluid close to the wall experiences substantial deceleration and finally separates at 95% chord (Fig. 26). A small recirculation region is seen close to the wall in Figs. 27 and 28. Note that the velocity distribution is plotted against the Levy-Lees normal coordinate η . This coordinate is scaled such that boundary layer growth in the transformed coordinate system is minimized thereby reducing the number of grid points required in the finite difference calculation, substantially reducing the computational effort. The displacement thickness growth is very rapid near the blade trailing edge as can be seen in Fig. 29. The skin friction distribution versus airfoil surface streamwise distance is found in Fig. 30. Note that near the blade trailing edge a negative skin friction coefficient exists indicating flow separation. The inverse calculation procedure with the FLARE approximation experienced no difficulty with the calculation in that region.

The calculated Mach number distribution for the Gostelow cascade

pressure surface is found in Fig. 31. Once again the region of strong interaction between the viscous and inviscid flow field is near the blade trailing edge. However, the interaction on the pressure side is weaker than the suction side. At the blade trailing edge, the inviscid edge Mach number 0.066 while the viscous inviscid interaction calculation gives a value of 0.065. The curvature at the blade trailing edge is reduced due to the boundary layer thickness thereby reducing the flow acceleration at that point resulting in a lower Mach number. The boundary layer development from 40% chord to the blade trailing edge is presented in Figs. 32 through 38. As seen from the velocity profiles, the boundary layers are healthy along the pressure surface and no flow separation occurs. Figure 39 gives the skin friction coefficient distribution for the pressure side. The skin friction coefficients are positive over the entire surface and increase near the trailing edge due to the favorable pressure gradient. A plot of the displacement thickness is found in Fig. 40. Note that the displacement thickness is much smaller on the pressure surface than the suction surface indicating more desirable velocity profiles in terms of avoiding flow separation. The displacement thickness decreases near the trailing edge also indicating the favorable pressure gradient and a healthy velocity profile.

The results from the boundary layer calculations on the suction and pressure surfaces on the airfoil were used to march downstream of the cascade into the wake. The Mach number distribution versus streamwise distance is presented in Fig. 41. At the cascade trailing edge line, the Mach number on the suction side of the wake is 0.075 while on the pressure side, the Mach number is 0.065 indicating the asymmetric

nature of the wake. This can also be evidenced in the large difference in the displacement thickness (Figs. 29, 40). Note that as the solution proceeds downstream, the Mach number on the suction and pressure sides reach the same value as the normal pressure gradient across the wake is alleviated. At $x/c = 1.5$ the Mach number on either side of the wake has reached a value of 0.068. Calculations in the wake are done in the inverse mode where the mass flux parameter is specified. The final distribution of this parameter is presented in Fig. 42. The wake velocity profile at $x/c = 1.01$ is found in Fig. 43. The fluid at the wake centerline has accelerated and the point of minimum velocity has moved up into the suction side of the wake. This curvature of the centerline is caused by the asymmetric nature of the wake. From Fig. 43 it is seen that the slope of the velocity decrease is steeper on the pressure side than the suction side of the wake. This is similar to the experimental study of Gallus [5,6]. Note that the velocity in the wake has been divided by the suction surface edge velocity and plotted against the Levy-Lees coordinate η which is used once again to minimize wake spreading and, therefore the computational effort. Figure 44 shows the wake profile at $x/c = 1.045$. The flow continues to accelerate along the wake centerline and the point of minimum velocity has moved up farther into the suction side of the wake. This curvature effect can be related to the deviation from the inviscid exit flow angle experienced in actual compressor cascades. Note that the suction side edge Mach number has decreased while the pressure side edge Mach number has increased as the flow is alleviating the normal pressure gradient in the wake. Figures 45 through 49 give the development of the wake profile up to $x/c =$

1.490. Figures 49 through 51 show the wake velocity profiles versus the nondimensional physical coordinate y/L , where L is the chord length for $x/c = 1.01, 1.225$ and 1.487 , respectively. It is seen that the wake width increases and the velocity gradient decreases as the distance from the trailing edge increases.

From the numerical study of the Gostelow cascade, it can be concluded that the numerical analysis can handle flow separation and asymmetric wakes in terms of wake development and cascade deviation angle.

CHAPTER 4

Numerical Results and Comparison with Experimental Data

4.1 1968 Stanford Conference Data

The first case to be analyzed was a comparison with the data of Lugwig and Tillman [66] for a mild adverse pressure gradient. The flow identification number was 1100. The turbulent boundary layer calculation was initiated by matching the skin friction coefficient, displacement thickness and momentum thickness at the starting point. The values of the freestream velocity and velocity gradient were specified and the direct calculation mode was used for the boundary layer calculation. A comparison of the calculated skin friction coefficient distribution versus the experimental values is found in Fig. 53. An excellent match between the analytical and experimental results was obtained. This indicates that the chosen turbulent eddy viscosity model was working properly.

4.2 Flat Plate Symmetric Turbulent Wake Data

The development of the turbulent wake from the turbulent boundary layers on the two sides of a thin flat plate with zero pressure gradient represents a simple problem. However, it is of considerable interest as it represents the limiting case of flow near the trailing edge of an airfoil and into the wake. The data of Chevray and Kovaszny [67] was chosen. An aluminum flat plate was used with dimensions 240 cm long, 50 cm wide with a constant thickness of 0.160 cm except the last 60 cm where it was machined down symmetrically on both sides so that the thickness tapered linearly to 0.025 cm at the trailing edge. Coil

springs were used as turbulence generators installed at 30 cm from the leading edge. This produced a thick and stable turbulent boundary layer at the trailing edge. The Reynolds number based on the boundary layer thickness was 1.5×10^4 . The flow was uniform over 75% of the span at the trailing edge and 60% of the span at the last wake station, indicating the two-dimensionality of the flow.

For the numerical analysis, the displacement thickness and shape factor at the trailing edge were matched with the experimental values. The flow over the first 30 cm was calculated as laminar with an instantaneous transition to turbulent flow at 30 cm. To match the experimental displacement thickness and shape factor, the calculation proceeded along the zero pressure gradient flat plate up to $X/L = 1.1$. The calculation into the wake was initiated at $X/L = 1.1$. The comparison of the predicted wake centerline velocity against the experimental centerline velocity is found in Fig. 54. The calculation was an interactive calculation in the inverse mode. The agreement between the numerical analysis and experimental data is very good. At the far downstream location, the centerline velocity is underpredicted by approximately 3%.

4.3 Supercritical Cascade Builds 1 and 2

In recent years, compressor cascade technology has advanced to the point where mathematically defined airfoils can be designed for given aerodynamic and structural requirements. One important example of this type of designed airfoil is the supercritical airfoil. Supercritical airfoils are transonic airfoils which operate with subsonic inlet and exit flow velocities with embedded regions of supersonic flow adjacent

to the airfoil suction surface. The term supercritical refers to the presence of velocities in the flowfield which are above the critical or sonic speed. This type of cascade, if designed to be shock free, proved to be superior in overall performance in comparison to standard airfoil series. To obtain a shock free design, however, requires an accurate prediction of the blade-to-blade flow field. Mathematical techniques that closely model the aerodynamics of cascades except in the region of thick blunt trailing edges are available. In this region inviscid flow calculations are inadequate even with boundary layer adjustments to the airfoil surface because they do not account for the strong interaction or model the wake. The wake modelling deficiency leads to two major problems. The first problem arises because the surface velocity distribution cannot be computed accurately without accounting for the strong interaction between the viscous and inviscid flow fields. The second problem involves inaccuracies throughout the entire trailing edge region. The large velocity variation at the trailing edge creates an artificial disturbance which leads to errors in the calculation of the downstream flow properties when wake mixing calculations are used.

To assess the accuracy of the current calculation, a comparison was made with the experiment data of Hobbs et al. [68]. Detailed cascade wake flow data was obtained for two configurations. Build 1 was a supercritical fore-loaded cascade, while Build 2 was the standard multiple circular arc aft-loaded compressor cascade. To achieve acceptable measurement accuracy near the trailing edge, a large scale, low speed experiment was performed. The scale-speed combination was chosen to retain dynamic similitude in the wake by holding the Reynolds number

based on airfoil chord within the correct range. It was stated that both cascades had undergone extensive high speed testing with no significant change in performance. The two-dimensionality of the flow was maintained by controlling the endwall boundary layer flows to achieve an overall midspan axial velocity density ratio near one.

The supercritical cascade Build 1 is presented in Fig. 55. Note the waviness in the airfoil leading and trailing edge regions. The data in Ref. 68 did not include the airfoil coordinates and an attempt was made to obtain them from a sketch. Due to the inaccuracies associated with the airfoil shape attempts to accurately predict the airfoil surface velocity distribution had to be abandoned.

For Build 1 the following test conditions existed:

Inlet Air Angle	52°
Exit Air Angle	87.1°
Flow Turning	35.1°
Inlet Mach Number	.1132
Exit Mach Number	.0912
Profile Loss	0.017
Reynolds Number	4.78×10^5

The surface Mach number distributions calculated from the experimental static pressure data are presented in Figs. 56 and 57 for the suction and pressure surfaces, respectively. The velocity profile near the airfoil trailing edge and near wake were measured with a single hot film probe. Kiel and five-hole combination probes were used for the wake traverses.

The numerical calculations were initiated at the blade leading edge

and transition to turbulent flow was assumed to occur at 4% chord. This was the earliest station to initiate the turbulent flow calculation and still maintain a stable calculation. The experimental Mach number distribution was used as the input edge Mach number distribution. The current analysis had no problems in calculating along the airfoil surface and into the wake. The first station at which experimental velocity profile data available was for 97% chord. In Fig. 58 the numerical results of the current analysis are compared with the experimental profile for the suction surface. For the experimental data, the estimated probe placement accuracies are ± 0.005 y/pitch in an absolute sense and 0.0002 y/pitch in a relative sense. Taking this into account in Fig. 58 produces excellent agreement between the numerical prediction and the data. Figure 59 gives the comparison between the experimental and calculated velocity profiles for $x/c = 1$ on the airfoil suction surface. Excellent agreement is obtained between calculation and experiment. Figures 60 and 61 show similar comparisons for the pressure surface at $x/c = 0.97$ and $x/c = 1$. Once again very good agreement is obtained between experiment and calculation.

In Figs. 62 through 65 the comparison of the experimental versus calculated velocity profiles in the near wake are presented for $x/c = 1.01, 1.02, 1.03$ and 1.06 , respectively. Agreement between the experimental and calculated wake profiles is excellent and the highly asymmetric wake is clearly evident. Figure 66, for an intermediate wake station of $x/c = 1.13$, also shows excellent agreement between calculation and experiment. It can be seen that the width of the wake is increasing and the velocity defect is decreasing as the wake moves

downstream. Figures 67 and 68 give the velocity profiles in the far wake at $x/c = 1.39$ and 1.65 . The agreement between the data and calculation is good particularly in terms of wake width and shape, however, the velocity at the wake centerline is low by about 10%. The calculated profile loss coefficient for Build 1 was 0.0179. The coefficient was overestimated by approximately 5% when compared to test data.

For Build 2, a multiple circular arc aft-loaded cascade was investigated which is shown in Fig. 69. The following flow conditions existed:

Inlet Flow Angle	50.5°
Exit Flow Angle	87.1°
Flow Turning	36.6
Inlet Mach Number	0.1162
Exit Mach Number	0.0928
Profile Loss	0.0175
Reynolds Number	5.88×10^5

Figures 70 and 71 show the blade surface Mach number distribution calculated from the experimental blade surface pressure data for the suction and pressure side, respectively. Note the peak Mach number has been shifted aft in Build 2 in comparison to Build 1. This results in a more severe adverse pressure gradient near the blade trailing edge than Build 1. As in the calculation for Build 1, transition from laminar to turbulent flow was at 4% chord. It was suggested in Ref. 68 that intermittent flow separation was occurring in the last 10% chord on the suction surface for Build 2. The boundary layer prediction routine used in Ref. 68 did not reach the trailing edge on the suction surface. The present

calculation, however, changed the calculation procedure from the direct mode to the inverse mode and had no problem marching to the blade trailing edge and into the wake. Figure 72 gives the comparison between the computed and experimental velocity profile for $x/c = 0.97$ on the suction surface for Build 2. Excellent agreement is obtained between the experiment and the computations. A similar result is seen in Fig. 73 for $x/c = 1$ on the suction surface. Figures 74 and 75 show the comparison between the experimental and computed velocity profiles at $x/c = 0.97, 1$ respectively, for the pressure surface. Good agreement is also seen here. Figures 76 through 79 give the experimental and computed velocity profiles for the near wake at $x/c = 1.01, 1.02, 1.03$ and 1.06 , respectively. Excellent agreement is obtained between computed and experimental profiles in the near wake. The mixing in the trailing edge near wake region is much more rapid for Build 2 than Build 1. This is believed to be due to the difference in the velocity profiles on the suction surface at the blade trailing edge. The experimental and calculated wake velocity profiles for Build 2 at $x/c = 1.12$ and 1.23 are presented in Figs. 80 and 81. Good agreement was obtained for the wake shape, however, the minimum computed velocity was approximately 10% low at $x/c = 1.12$ and approximately 15% low at $x/c = 1.23$ in comparison to the test data. The calculated profile loss coefficient was 0.0187. The loss coefficient was overpredicted by approximately 7%. The discrepancy is directly related to the under prediction of the wake centerline velocity in the far wake.

CHAPTER 5 Summary and Recommendations

A unified approach has been presented to calculating the two-dimensional blade-to-blade flow field and ensuing wake for advanced compressor cascades. For laminar supersonic flow, operating in the direct mode with pressure gradient specified, the current analysis has compared well with existing numerical methods. For turbulent calculations in the direct mode, the analysis gave excellent agreement when compared with the Stanford Conference Ludwig and Tillman test data indicating the turbulent eddy viscosity concept functioned properly.

For cascade analysis, the calculation routine had no problem in handling the trailing edge separation in the case of the Gostelow compressor cascade. This numerical test case proved the full capability of the analysis by combining the solution of the full potential equations as input to the boundary layer computation for calculation in the direct mode. The routine located the region of strong interaction near the blade trailing edge on the suction side and the inverse calculation method was initiated whereby the "boundary layer mass flux" is specified. The routine had no difficulty in integrating through the separation region to the blade trailing edge and into the wake. The new inviscid velocity distribution was then efficiently calculated based on thin airfoil theory and the interactive routine gave the final result whereby the viscous and inviscid flow fields were correctly matched. The expected trends were calculated by the overall calculation procedure. The adverse pressure gradient was relieved on the suction side of the blade and as this occurred the length of the separation bubble at

the trailing edge diminished from 10% chord to 3% chord. The expected asymmetric wake was calculated and due to mixing in the wake the normal pressure gradient due to the mixing of the pressure and suction surface boundary layers was alleviated.

The overall calculation procedure was successful in the calculations of the flat plate turbulent symmetric wake profiles. In the near and intermediate wake, the match with the experimental data was excellent while at the far wake location, the centerline velocity was down in the computation by approximately 3%.

The procedure was successful in the prediction of the viscous flow field of current technology multiple circular arc and advanced technology supercritical compressor cascades. The agreement for the velocity profiles on the blade surface and in the near and intermediate wake was excellent. For the far wake, the general shape showed good agreement between computation and experiment, but the computed minimum velocity was consistently lower than the experiment. This was also evident in the flat plate comparison. The problem is believed to lie in the wake eddy viscosity term and the rate at which the turbulent eddy viscosity increases along the wake centerline. But, the result is not alarming, as most advanced compressor designs have blade row spacings on the order of 1/4 chord, and the current analysis compared well with experimental data in this range.

However, more work is required in the modelling of the turbulent eddy viscosity for cases where the far wake is important. Also in the regions on the blade surface where separation is present the current eddy viscosity model is highly suspect. The current model does not

include the normal stresses which are in general small and can be neglected. Near separation, however, the normal stresses grow and must be included if an accurate analysis is to be completed. Therefore work is also required in choosing or developing a model which can accomplish this consideration.

CHAPTER 6 Conclusions

A new computationally efficient compressible viscous-inviscid interaction calculation procedure has been developed and tested for two-dimensional cascade flow. Comparisons with numerical studies of other authors and with published test data have been made and excellent correlation of cascade pressure distributions, skin friction distributions, blade surface velocity profiles and wake profiles has been obtained for both laminar and turbulent flow. The calculation procedure is robust and easily handled all flow fields investigated, including a numerical test case with mild flow separation. The procedure is computationally efficient with an averaged calculation time for a compressible turbulent blade to blade flow field and wake calculation taking less than eight minutes on an IBM 3090 machine.

Finally, the eddy viscosity model of Cebeci for turbulent symmetric wakes was successfully modified to account for asymmetric wakes and good correlation was obtained in comparing the predicted wake velocity profiles with experimental velocity profiles for two advanced compressor cascades.

REFERENCES

1. Kemp, N. H., and W. R. Sears, "Aerodynamic Interference Between Moving Blade Rows," J. Aero. Sci., Vol. 20, No. 9, pp. 585-597, September 1953.
2. Kemp, N. H., and W. R. Sears, "The Unsteady Forces Due to Viscous Wakes in Turbomachines," J. Aero. Sci., Vol. 22, No. 7, pp. 478-483, July 1955.
3. Silverstein, A., S. Katzoff, and W. K. Bullivant, "Downwash and Wake Behind Plain and Flapped Airfoils," NACA Rpt. 651, 1939.
4. Kaji, S., and T. Okazaki, "Generation of Sound by Rotor-Stator Interaction," J. Sound Vib., 13 (3), pp. 281-307, 1970.
5. Gallus, H. E., J. Lambertz, and Th. Wallmann, "Blade Row Interaction in an Axial Flow Subsonic Compressor Stage," J. of Eng. for Power, Vol. 180, pp. 169-177, January 1980.
6. Gallus, H. E., H. Grollius, and J. Lambertz, "The Influence of Blade Number Ratio and Blade Row Spacing on Axial Flow Compressor Stator Dynamic Load and Stage Sound Pressure Level," J. of Eng. for Power, Vol. 104, pp. 633-641, July 1982.
7. Naumann, H., and H. Yeh, "Lift and Pressure Fluctuations of a Cumbered Airfoil under Periodic Gusts and Applications in Turbomachinery," J. of Eng. for Power, pp. 1-10, January 1973.
8. Henderson, R. E., "The Unsteady Response of an Axial Flow Turbomachine to an Upstream Disturbance," Ph.D. Dissertation, Engineering Department, University of Cambridge, 1972.
9. Walker, G. J., and A. R. Oliver, "The Effect of Interaction Between Wakes from Blade Rows in an Axial Flow Compressor on the Noise Generated by Blade Interaction," J. of Eng. for Power, pp. 241-248, October 1972.
10. Melnik, R. E., R. Chow, and H. R. Mead, AIAA Paper 77-680, 1977.
11. Deiwert, AIAA Journal, 14, p. 735, 1976.
12. Melnik, R. E., and J. W. Brook, "The Computation of Viscid/Inviscid Interaction on Airfoils with Separated Flow," Report Re-697, Corporate Research Center, Grumann Corporation, April 1985.
13. Pulliam, T. H., unpublished data.
14. Horstman, C. C., AIAA Paper 82-1021, 1982.
15. Lock, R. C., AGARD CP 291, Paper 2, 1981.

16. Lakshminarayana, B., and R. Raj, "Characteristics of the Wake Behind a Cascade of Airfoils," J. Fluid Mech., Vol. 61, Part 4, pp. 707-730, 1973.
17. Lakshminarayana, B., and R. Raj, "Three Dimensional Characteristics of Turbulent Wakes Behind Rotors of Axial Flow Turbomachinery," ASME Paper 75-GT-1, 1975.
18. Lakshminarayana, B., B. Reynolds, and A. Ravindranath, "Characteristics of the Near Wake of a Compressor of a Fan Rotor Blade," AIAA Journal, Vol. 17, No. 9, pp. 959-965, September 1979.
19. Lakshminarayana, B., and C. Hah, "Prediction of Two and Three Dimensional Asymmetric Turbulent Wakes Including Curvature and Rotation Effects," AIAA Journal, Vol. 18, No. 10, pp. 1196-1204, October 1980.
20. Lakshminarayana, B., and B. Reynolds, "Turbulence Characteristics in the Near Wake of a Compressor Rotor Blade," AIAA Journal, Vol. 18, No. 11, pp. 1354-1362, November 1980.
21. Lakshminarayana, B., and T. R. Govindan, "Analysis of Turbulent Boundary Layer on Cascade and Rotor Blades of Turbomachinery," AIAA Journal, Vol. 19, No. 10, pp. 1333-1341, October 1981.
22. Lakshminarayana, B., and C. Hah, "Freestream Turbulence Effects on the Development of a Rotor Wake," AIAA Journal, Vol. 19, No. 6, pp. 724-730, June 1981.
23. Goldstein, S., "On Laminar Boundary Layer Flow Near a Position of Separation," Quarterly Journal of Mechanics and Applied Mathematics, Vol. I, p. 43, 1948.
24. Catherall, D., and K. W. Mangler, "The Integration of the Two-Dimensional Boundary Layer Equations Past the Point of Vanishing Skin Friction," Journal of Fluid Mechanics, Vol. 9, pp. 163-182, 1977.
25. Cebeci, T., "An Inverse Boundary Layer Method for Compressible Laminar and Turbulent Boundary Layers," J. Aircraft, Vol. 13, No. 9, pp. 709-718, September 1976.
26. Carter, J. E., "Inverse Boundary Layer Theory and Comparison with Experiment," NASA TP 1208, 1978.
27. Klineberg, J. M., and Steger, J. L., "On Laminar Boundary Layer Separation," AIAA Paper 74-94, January 1974.
28. Horton, H. P., "Numerical Solution of Laminar Boundary Layer Problems Using Invariant Imbedding: Inverse Problems," Queen Mary College, Faculty of Engineering, EP 1039, 1981.

29. Carter, J. E., and Wornom, S. F., "Solutions for Incompressible Separated Boundary Layers Including Viscous-Inviscid Interaction," NASA SP-347, pp. 125-150, 1975.
30. Klineburg, J. M., and J. L. Steger, "Calculation of Separated Flows at Subsonic and Transonic Speeds," Proceedings of the 3rd International Conference on Numerical Methods in Fluid Mechanics, Lecture Notes in Physics, Vol. 19, Springer-Verlag, Berlin, pp. 161-168, 1973.
31. Le Balleur, J. C., "Couplage visqueux-non visqueux: methode numerique et applications aux e'coulements bidimensionnels transoniques et supersoniques," La Recherche Aerospatiale, Vol. 183, pp. 65-76, 1978.
32. Kwon, O. K., and R. H. Pletcher, "Prediction of Incompressible Separated Boundary Layers Including Viscous-Inviscid Interaction," Journal of Fluids Engr., Vol. 101, No. 4, pp. 466-472, 1979.
33. Carter, J. E., "A New Boundary Layer Inviscid Interaction Technique for Separated Flow," AIAA Paper 79-1450, July 1979.
34. Lagerstrom, P. A., "Solutions of the Navier-Stokes Equation at Large Reynolds Number," SIAM Journal of Applied Mathematics, Vol. 28, No. 1, pp. 202-214, 1975.
35. Veldman, A. E. P., "New Quasi-Simulataneous Method to Calculate Interacting Boundary Layers," AIAA Journal, Vol. 19, No. 1, pp. 79-85, January 1981.
36. Moses, H. L., S. B. Thomason, and R. R. Jones, "Simultaneous Solution of the Inviscid Flow and Boundary Layers for Compressor Cascades," AIAA Journal, Vol. 20, No. 10, pp. 1466-1468, October 1982.
37. Moses, H. L., "Simultaneous Solution of the Inviscid Flow with a Finite Difference Boundary Layer Calculation," AIAA Ppaer 85-1274. 1985.
38. Ni, R. H., "A Multiple-Grid Scheme for Solving the Euler Equations," AIAA Journal, Vol. 20, No. 11, pp. 1565-1571, November 1982.
39. Caspar, J. R., "A Model Problem Study of Transonic Potential Flow Procedures," AIAA-80-0337, January 1980.
40. Ives, D. C., and J. F. Liutermaza, "Second Order Accurate Calculation of Transonic Flow over Turbomachinery Cascades," AIAA Journal, Vol. 17, pp. 838-844, August 1979.
41. Conte, S. D., and C. De Boor, Elementary Numerical Analysis, McGraw-Hill Book Company, 1972.
42. Swift, G. W., "The Solution of N Simultaneous Second Order Dif-

- ferential Equations by the Finite Difference Method," VPI-E-71-3, February 1971.
43. Courant, R., K. O. Friedrichs, and H. Lewy, "On the Partial Difference Equations of Mathematical Physics," IBM Journal, pp. 215-234, March 1967. (Translated form original German publication, 1928.)
 44. Hafez, M., J. South, and E. Murman, "Artificial Compressibility Methods for Numerical Solutions of Transonic Full Potential Equation," AIAA Journal, Vol. 17, pp. 838-844, August 1979.
 45. Gostelow, J. P., Cascade Aerodynamics, Pergamon Press, 1984.
 46. Hobson, D. G., "Shock-Free Transonic Flow in Turbomachinery Cascades," University of Cambridge, Dept. of Engineering, Rept. CUED/A Turbo/TR65, 1974.
 47. Korn, D. G., "Numerical Design of Transonic Cascades," Courant Institute of Mathematical Sciences, ERDA Mathematics and Computing Laboratory, Rept. COO-3077-72, January 1975.
 48. Reynolds, O., "An Experimental Investigation of the Circumstances Which Determine Whether the Motion of Water in Parallel Channels Shall be Direct or Sinuous and the Law of Resistance in Parallel Channels," Phil. Trans. Roy. Soc., Vol. 174, London, pp. 935-982, 1883.
 49. VanDriest, E. R., "Turbulent Boundary Layer in Compressible Fluids," J. Aero Sciences, Vol. 18, No. 3, pp. 145-160, March 1951.
 50. Harris, J. E., "Numerical Solution of Equations for Laminar, Transitional, and Turbulent Boundary Layers and Comparison with Experimental Data," NASA TR-368, 1971.
 51. Hayes, W. D., and R. F. Probstein, Hypersonic Flow Theory, Academic Press, 1959.
 52. Cebeci, T., and A. M. O. Smith, Analysis of Turbulent Boundary Layers, Academic Press, Inc., 1974.
 53. Patankar, S. V., and D. B. Spalding, Heat and Mass Transfer in Boundary Layers, Morgan-Grampiar Press, London, 1967.
 54. Cebeci, T., "Behavior of Turbulent Flow Near a Porous Wall with Pressure Gradient," AIAA Journal, Vol. 8, p. 2152, December 1970.
 55. Cebeci, T., Editor, Numerical and Physical Aspects of Aerodynamic Flows II, Springer-Verlag, pp. 163-174, 1983.

56. Brown, S. N., and K. Stewartson, "Laminar Separation," Annual Review of Fluid Mechanics, Vol. 1, pp. 45-72, 1969.
57. Williams, J. C., "Incompressible Boundary Layer Separation," Annual Review of Fluid Mechanics, Vol. 9, pp. 113-144, 1977.
58. Reyhner, T. A., and I. Flugge-Lotz, "The Interaction of a Shock Wave with a Laminar Boundary Layer," Int. J. Non-Linear Mech., Vol. 3, pp. 173-199, 1968.
59. Veldman, A. E. P., "Boundary Layer Flow Past a Finite Flat Plate," Thesis, Mathematics Institute, University of Groningen, The Netherlands, 1976.
60. Stewartson, K., "Multistructural Boundary Layers on Flat Plates and Related Bodies," Advances in Applied Mechanics, Vol. 14, pp. 145-239, 1974.
61. Cebeci, T., Editor, Numerical and Physical Aspects of Aerodynamic Flows II, Springer-Verlag, pp. 141-162, 1983.
62. Lees, L., and B. L. Reeves, "Supersonic Separated and Reattaching Laminar Flows: I. General Theory and Application to Adiabatic Boundary Layer/Shock Wave Interactions," AIAA Journal, Vol. 2, pp. 1907-1920, November 1964.
63. Cebeci, T., F. Thiele, P. G. Williams, and K. Stewartson, "On the Calculation of Symmetric Wakes, I. Two Dimensional Flows," Numerical Heat Transfer, Vol. 2, pp. 35-60, 1979.
64. Howarth, L., "On the Solution of the Laminar Boundary Layer Equations," Proc. Roy. Soc. London, Ser. A, Vol. 164, pp. 547-579.
65. Werle, M. J., and B. L. Senechal, "A Numerical Study of Separating Supersonic Laminar Boundary Layers," Virginia Polytechnic Institute and State University, VPIE-71-72, December 1971.
66. Ludwig, H., and W. Tillmann, "Investigations of the Wall Shearing Stress in Turbulent Boundary Layers," NACA TM 1285, 1950.
67. Chevray, R., Kovaszny, Leslie, S., G., "Turbulence Measurements in the Wake of a Thin Flat Plate," AIAA Journal, August 1969, pp. 1641-1642.
68. Hobbs, D. E., J. H. Wagner, J. F. Dannenhoffer, and R. P. Dring, "Wake Experiments and Modeling for Fore- and Aft-Loaded Compressor Cascades," Pratt and Whitney Aircraft Group, GPD, FR-13514, June 1980.

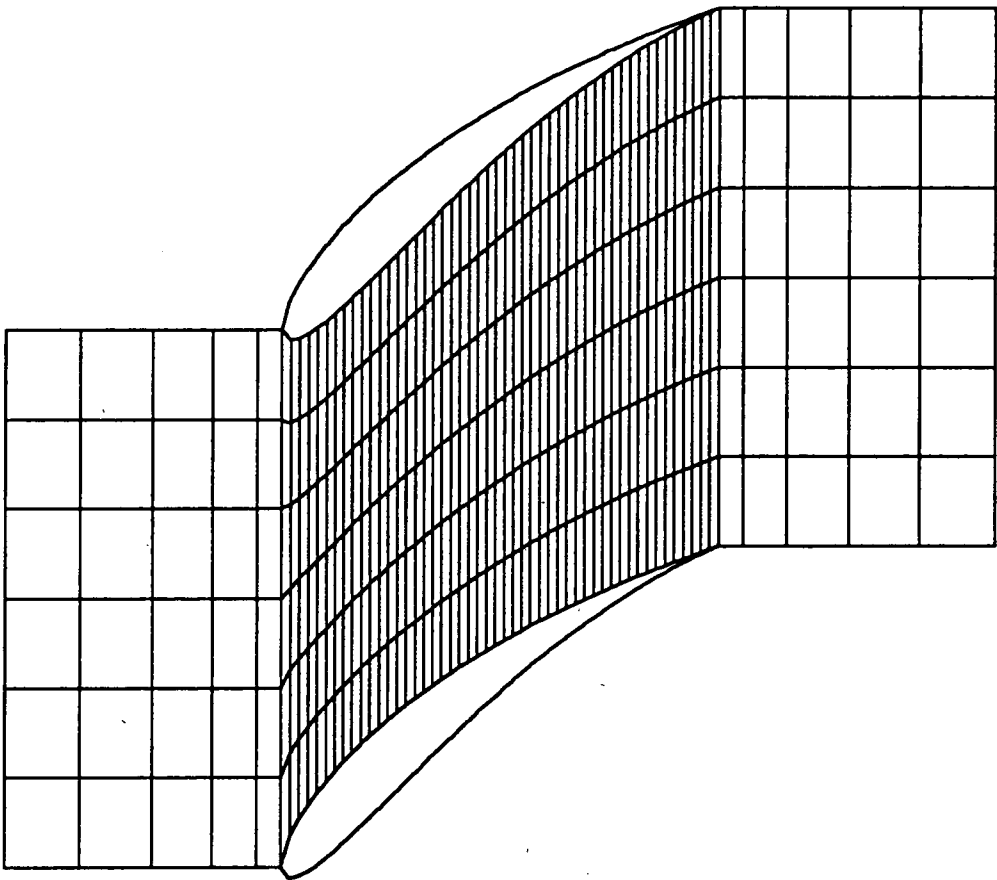


FIGURE 1 SAMPLE COMPRESSOR GRID

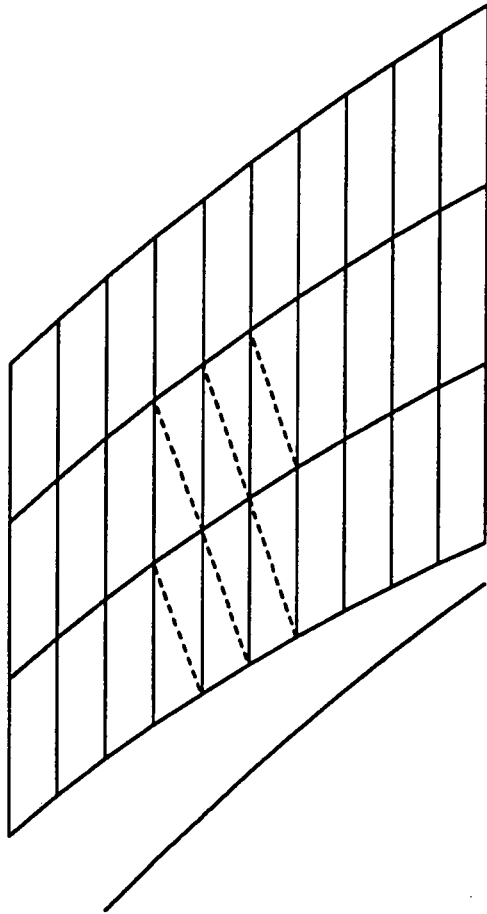


FIGURE 2 GRID TRIANGULATION

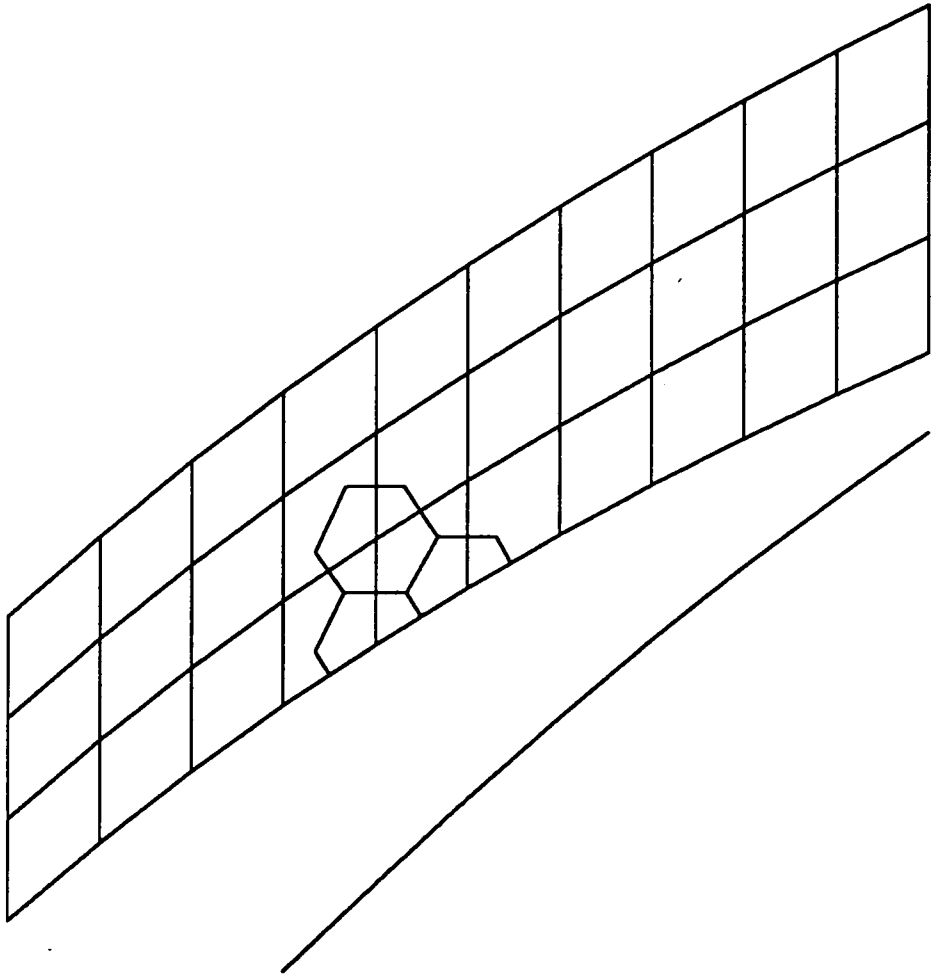


FIGURE 3 CONSTRUCTION OF MESH POLYGONS

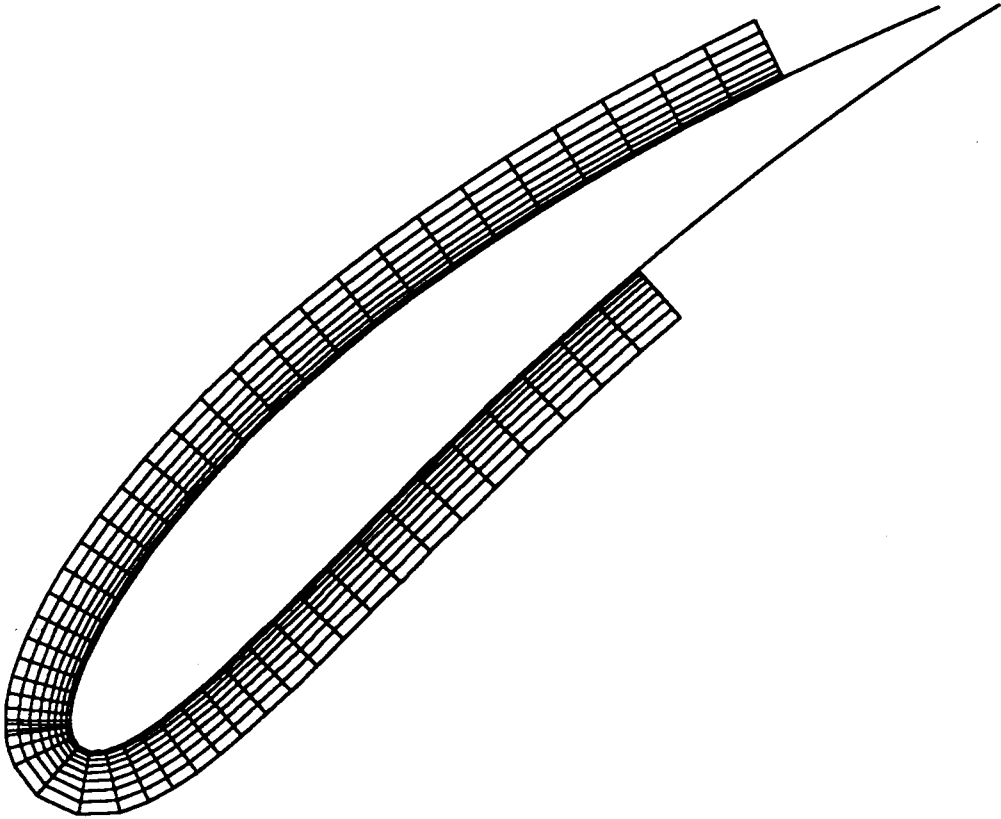


FIGURE 4 LOCAL GRID CONSTRUCTION

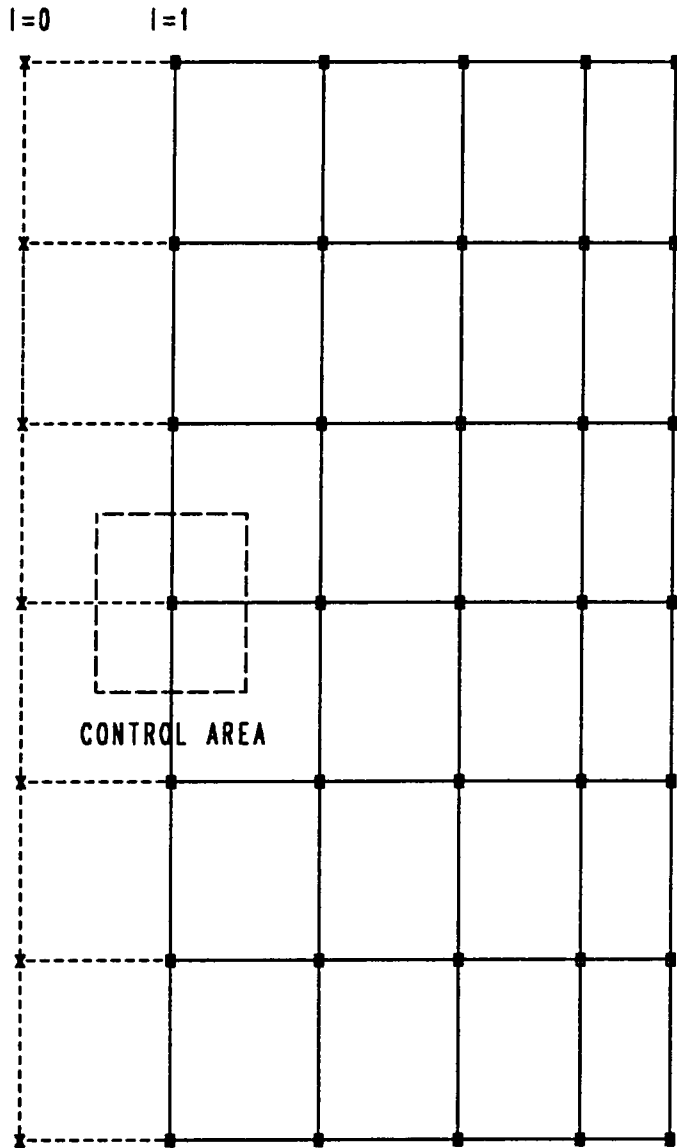


FIGURE 5 FIRST UPSTREAM GRID LINE

CASCADE DATA

GAP/CHORD=0.992
STAGGER ANGLE=37.5
INLET AIR ANGLE=53.5
EXIT AIR ANGLE=30.0

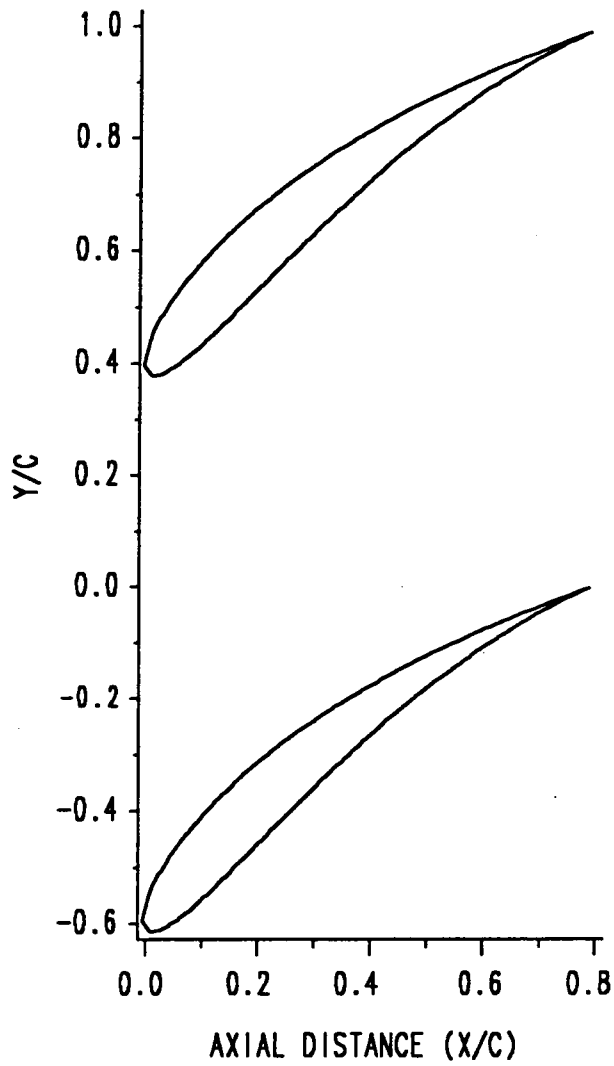
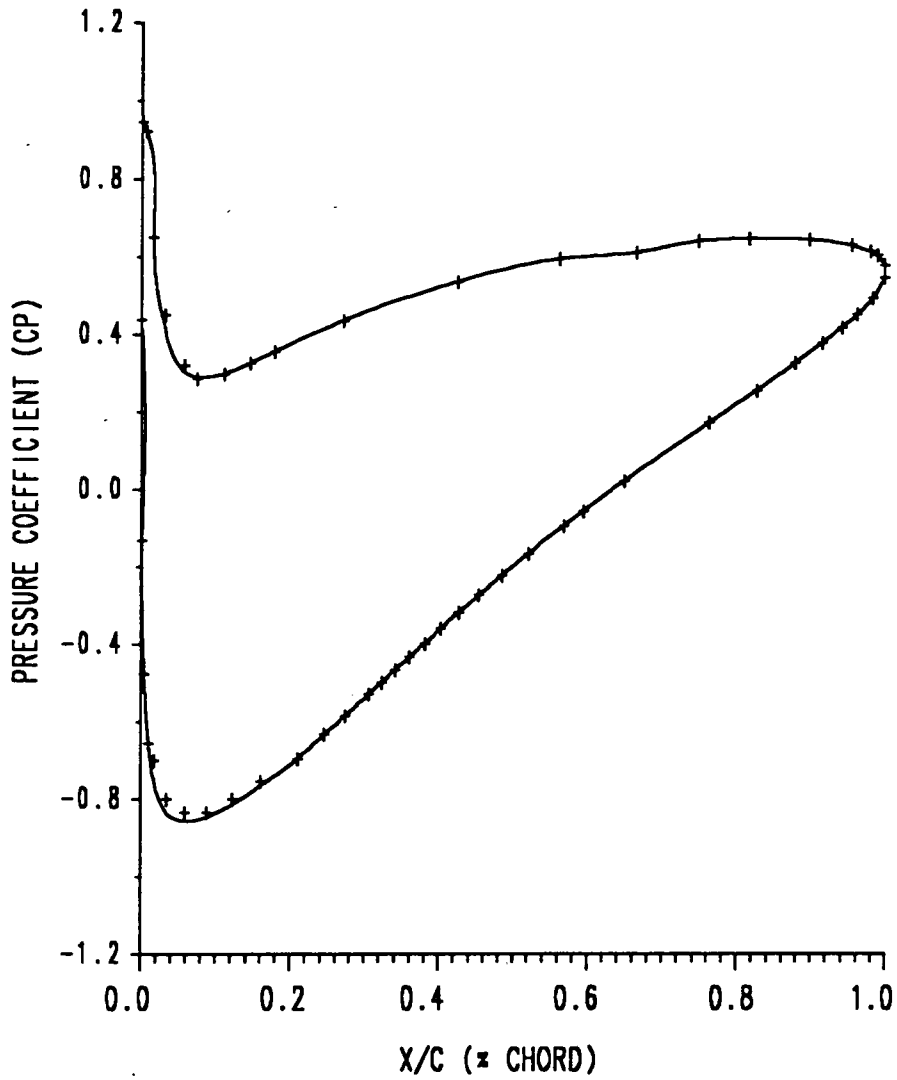


FIGURE 6 GOSTELOW COMPRESSOR CASCADE

INCOMPRESSIBLE FLOW



CASE + + + CURRENT ANALYSIS ——— EXACT ANALYSIS

FIGURE 7 PRESSURE COEFFICIENT COMPARISON FOR GOSTELOW CASCADE

CASCADE DATA

GAP/CHORD=0.5259
STAGGER ANGLE=0.0
INLET AIR ANGLE=53.9
INLET MACH NUMBER=0.58

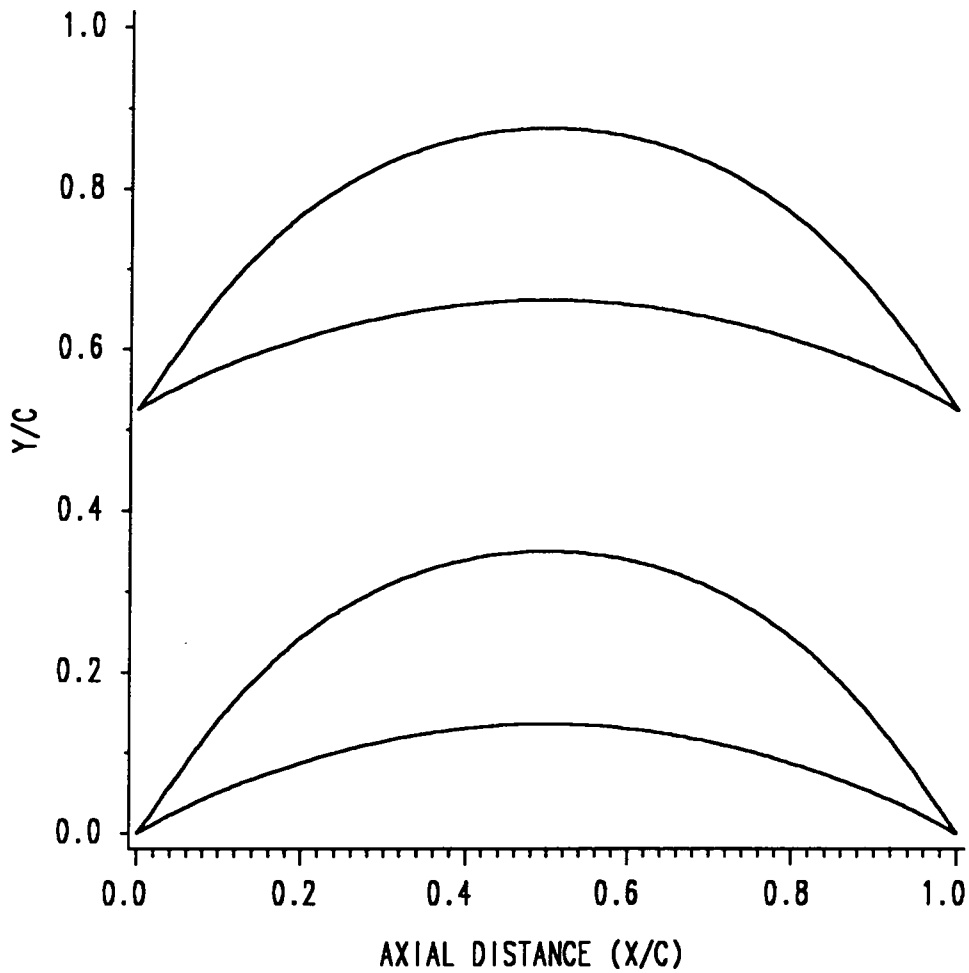
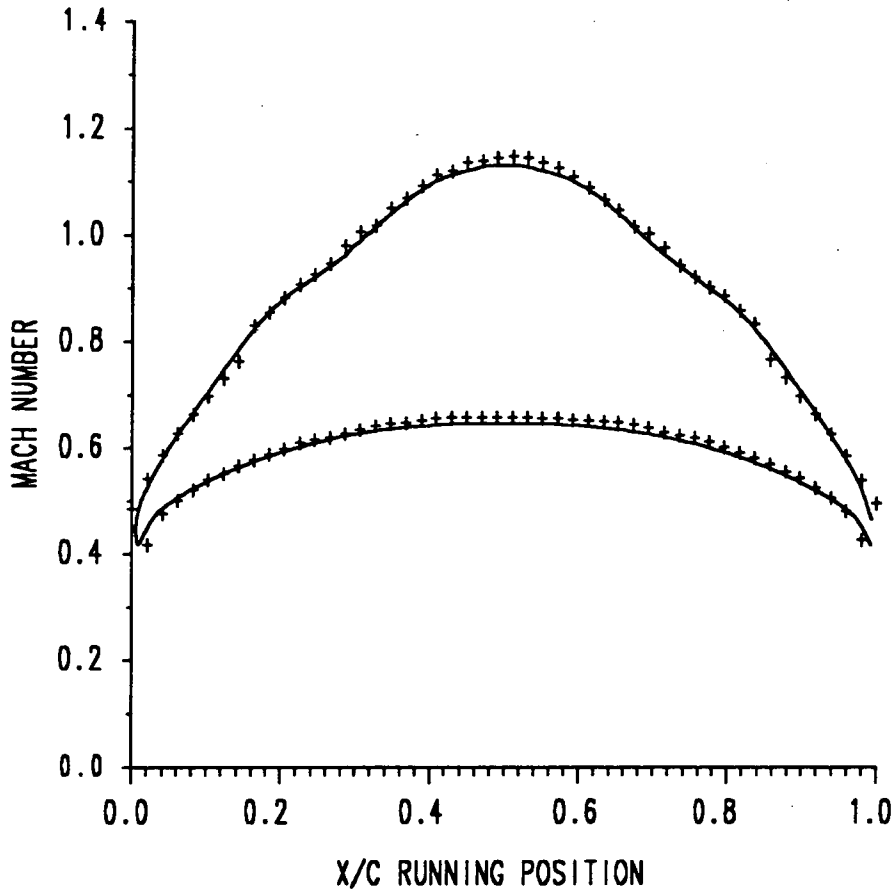


FIGURE 8 HOBSON IMPULSE TURBINE CASCADE

TRANSONIC FLOW



CASE + + + CURRENT ANALYSIS ——— EXACT ANALYSIS

FIGURE 9 MACH NUMBER COMPARISON FOR HOBSON TURBINE CASCADE

CASCADE DATA

GAP/CHORD=2.47
STAGGER ANGLE=37.5
INLET AIR ANGLE=50.0
INLET MACH NUMBER=0.70

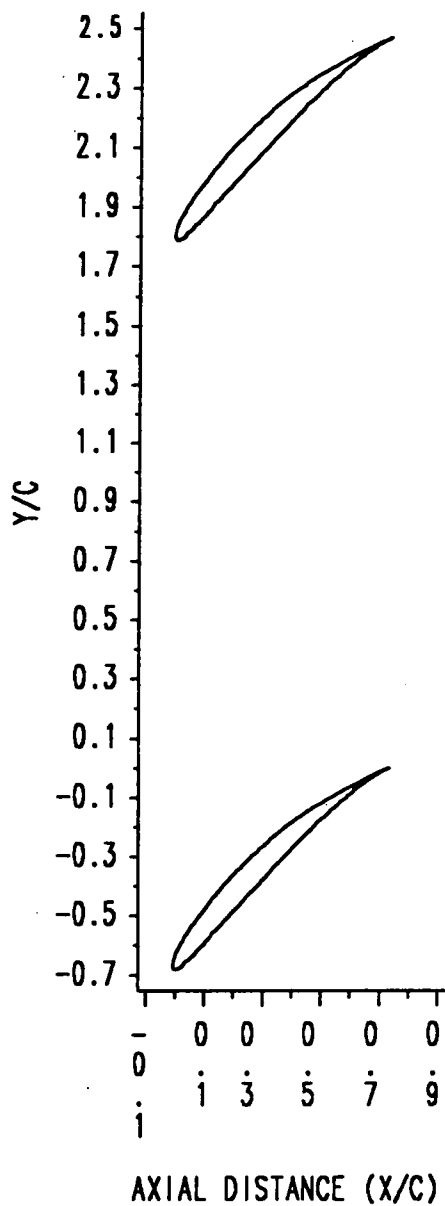
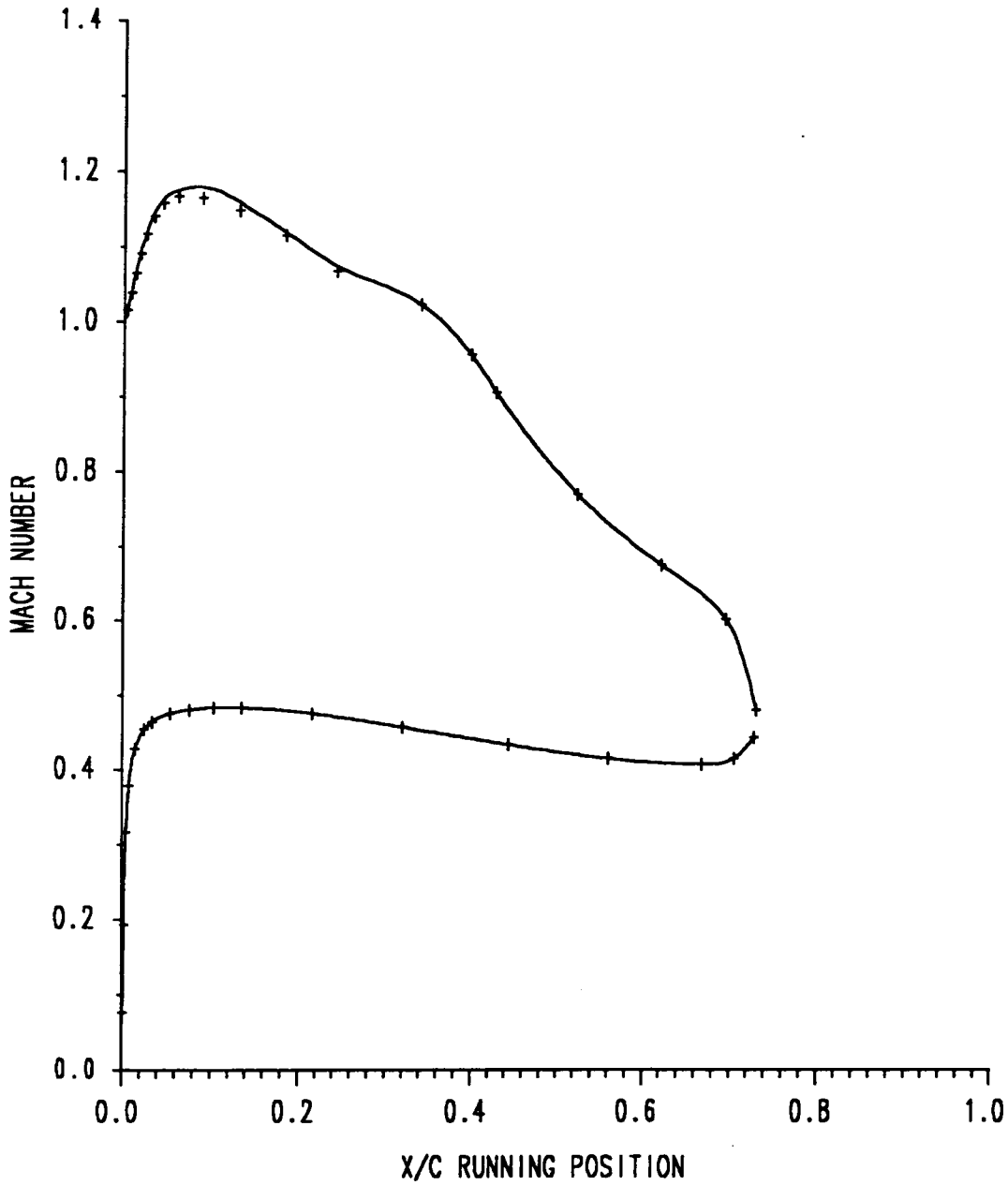


FIGURE 10 KORN COMPRESSOR CASCADE

TRANSONIC FLOW



CASE + + + CURRENT ANALYSIS ——— EXACT ANALYSIS

FIGURE 11 MACH NUMBER COMPARISON FOR KORN COMPRESSOR CASCADE

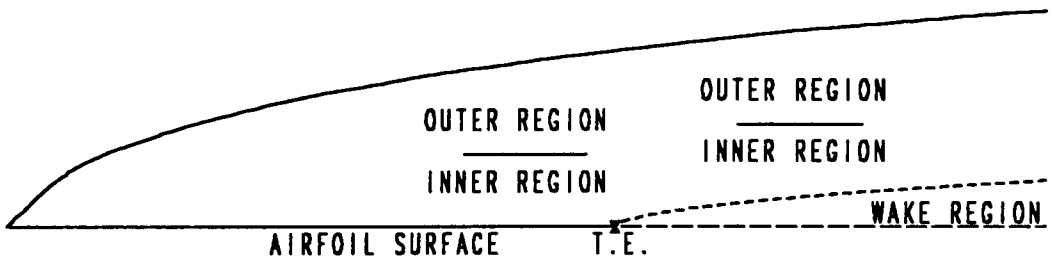


FIGURE 12 EDDY VISCOSITY REGIONS FOR WALL AND WAKE FLOWS

MACH NUMBER=4

$$UE=1-X$$

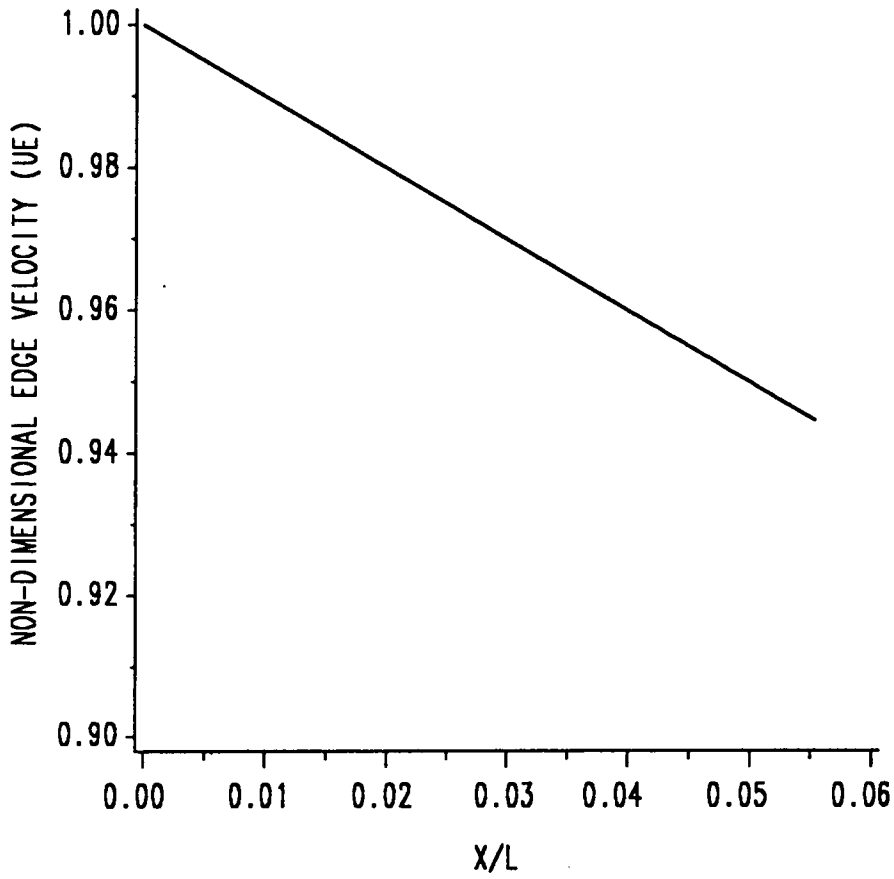


FIGURE 13 HOWARTH FLOW EDGE VELOCITY PROFILE

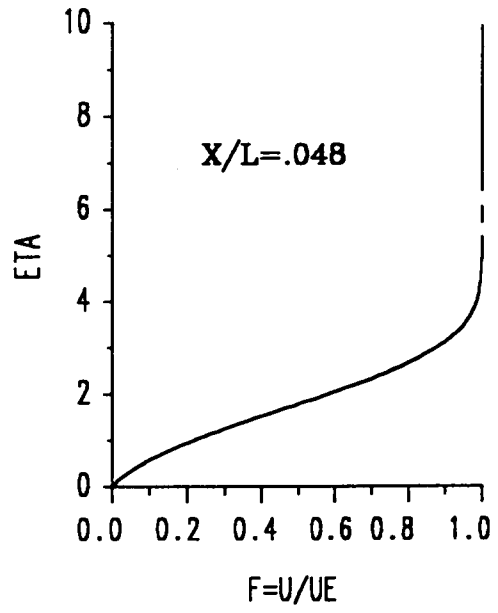
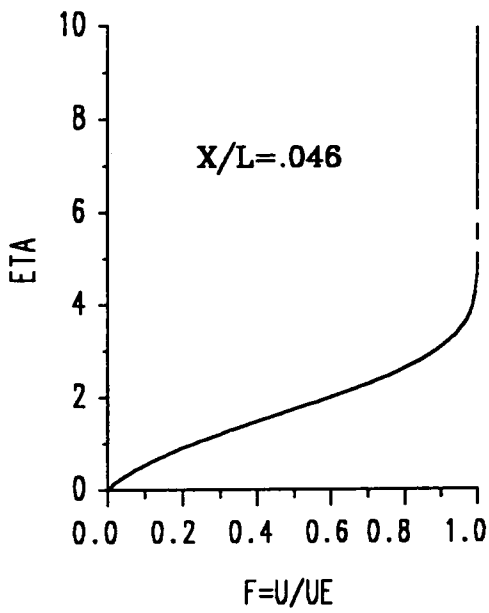
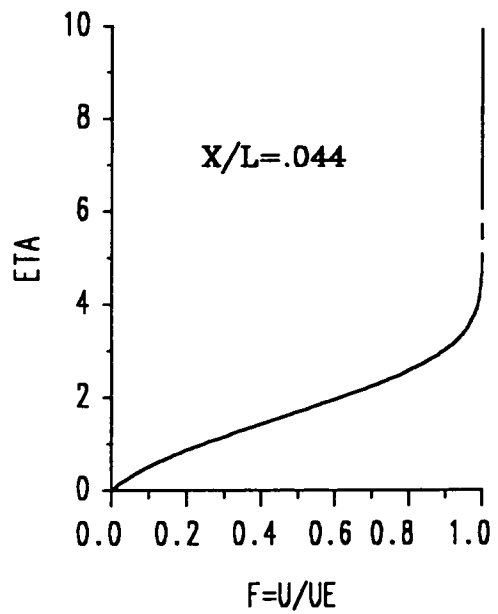
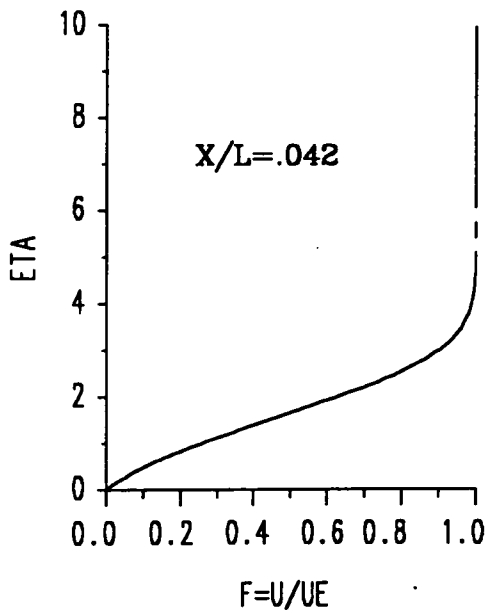


FIGURE 14 LAMINAR FLOW VELOCITY PROFILE FOR HOWARTH FLOW

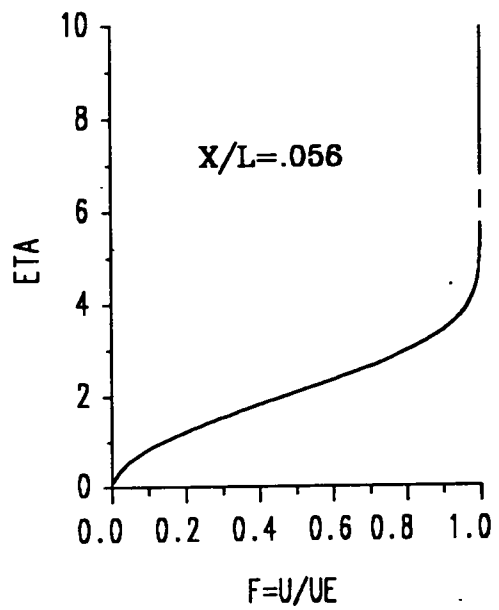
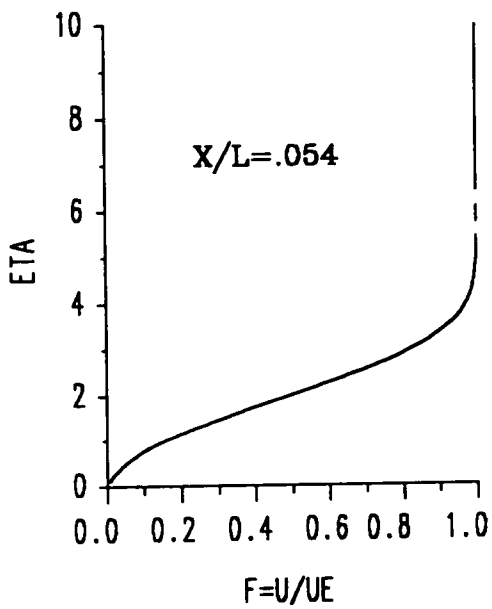
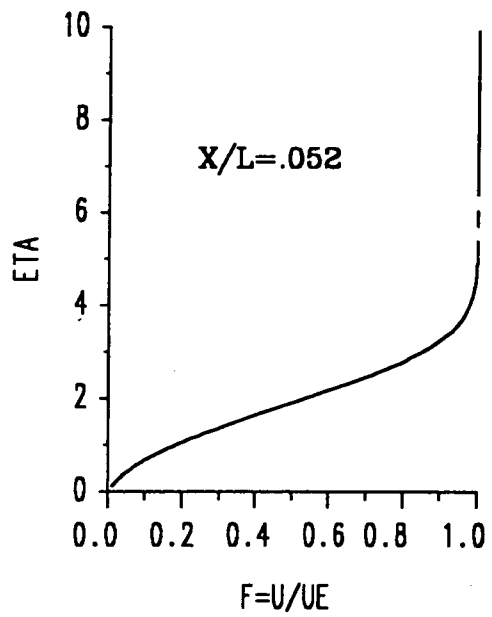
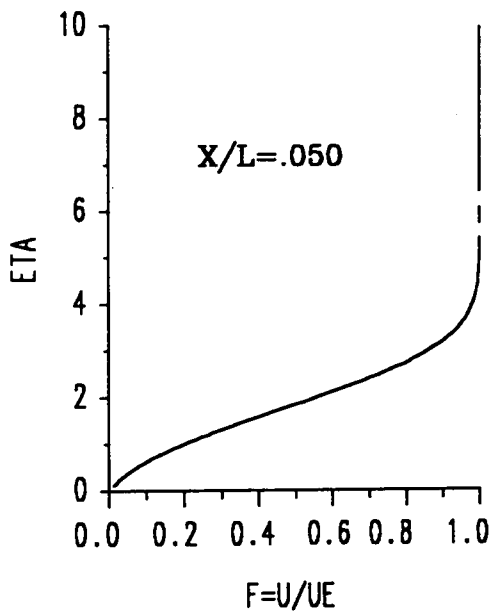
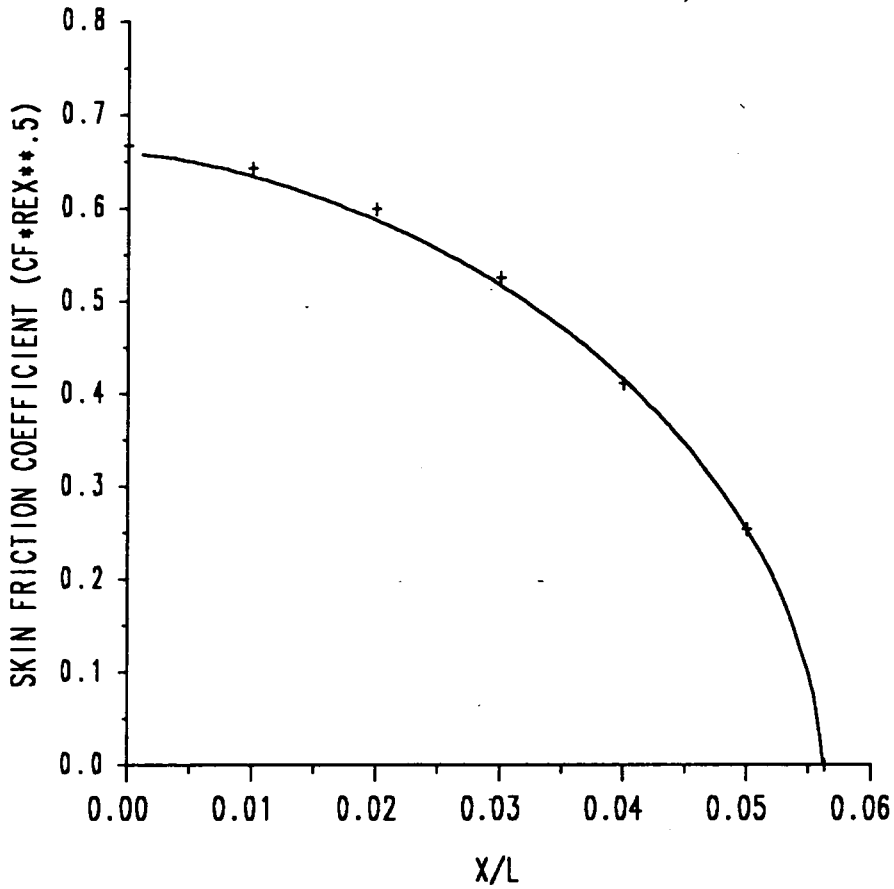


FIGURE 15 LAMINAR FLOW VELOCITY PROFILE FOR HOWARTH FLOW

COMPRESSIBLE FLOW M=4
DIRECT MODE

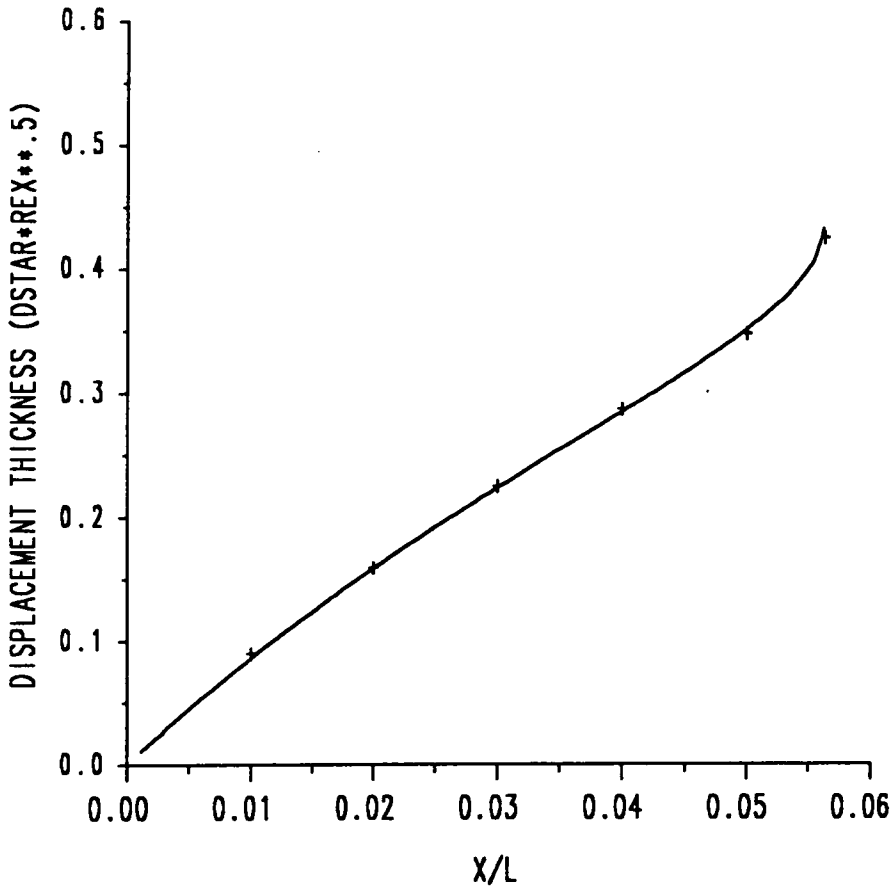


CASE — CURRENT ANALYSIS + + + WERLE (REF. 65)

FIGURE 16 SKIN FRICTION COEFFICIENT FOR HOWARTH FLOW

COMPRESSIBLE FLOW M=4

DIRECT MODE



CASE ——— CURRENT ANALYSIS + + + WERLE (REF. 65)

FIGURE 17 DISPLACEMENT THICKNESS FOR HOWARTH FLOW

SUCTION SURFACE

----- INVISCID SOLUTION

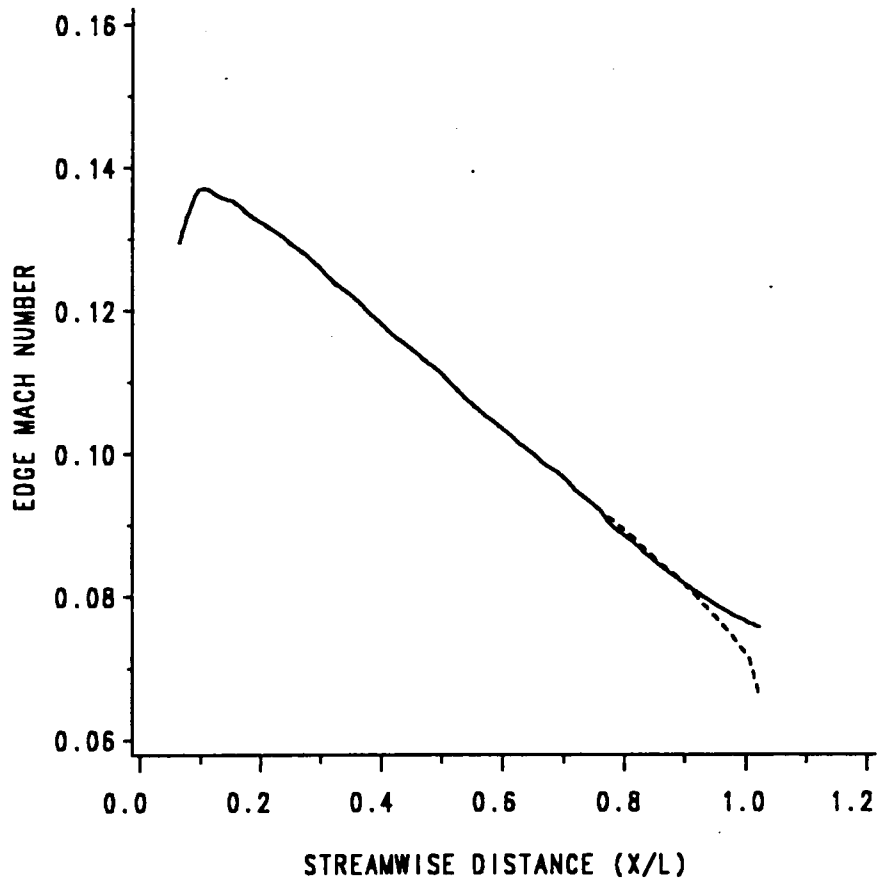


FIGURE 18 GOSTELOW CASCADE EDGE MACH NUMBER

SUCTION SURFACE

MACH NUMBER=0.111

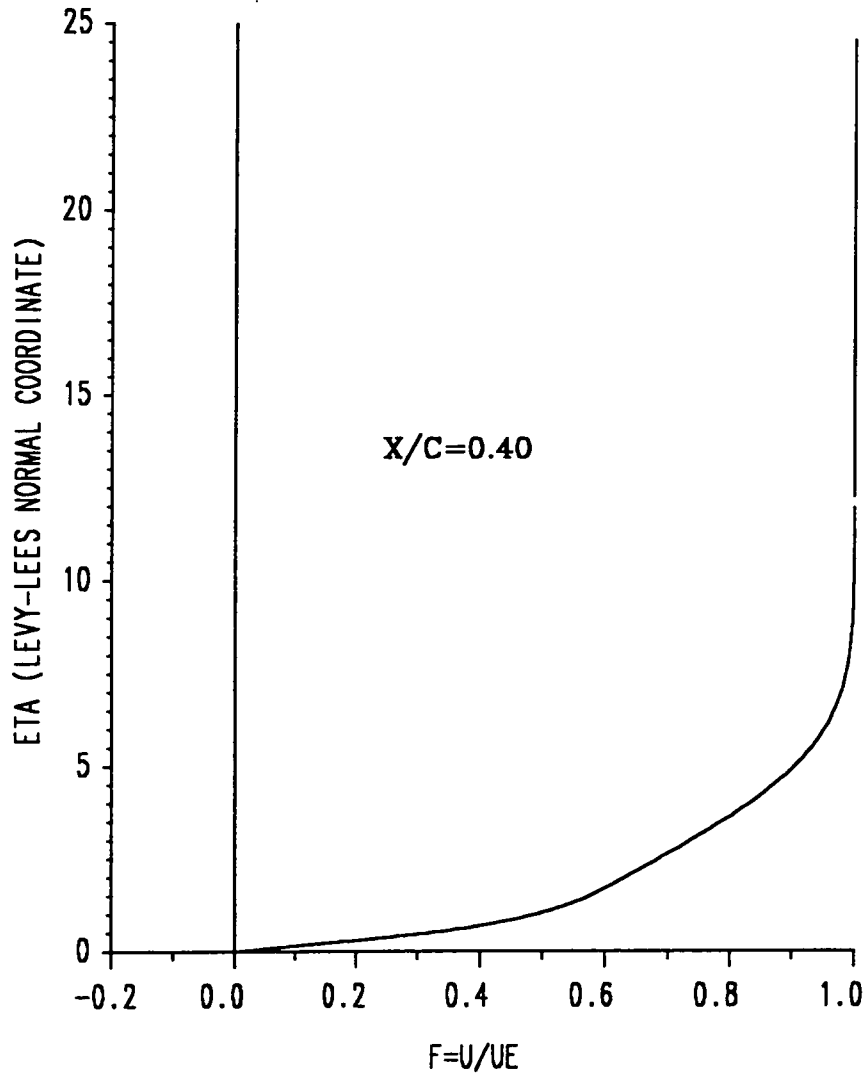


FIGURE 19 GOSTELOW CASCADE TURBULENT FLOW VELOCITY PROFILE

SUCTION SURFACE

MACH NUMBER=0.104

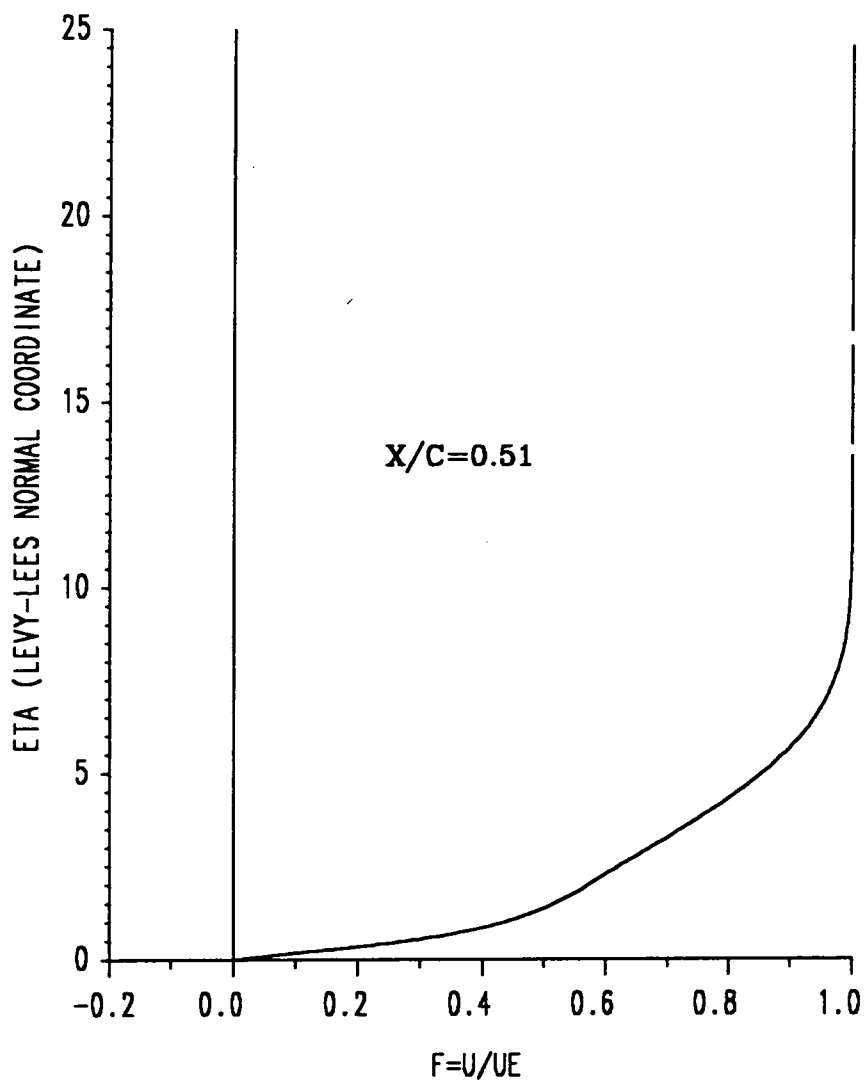


FIGURE 20 GOSTELOW CASCADE TURBULENT FLOW VELOCITY PROFILE

SUCTION SURFACE

MACH NUMBER=0.098

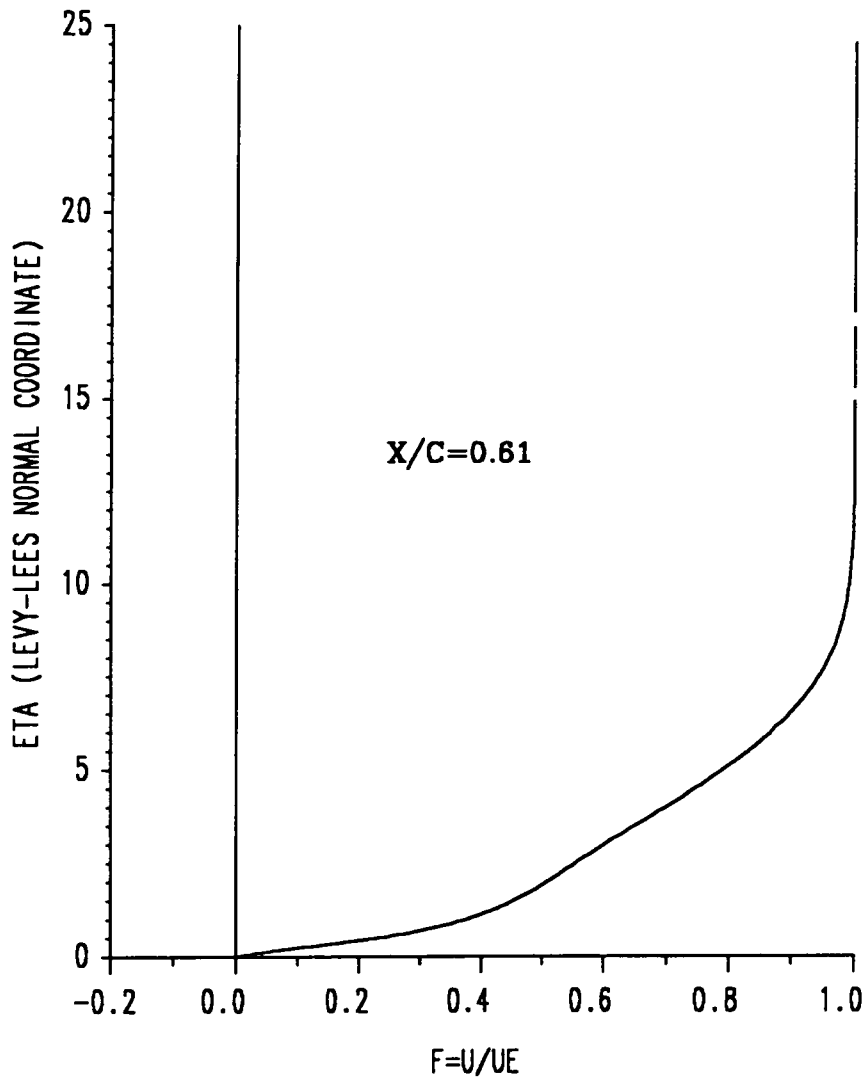


FIGURE 21 GOSTELOW CASCADE TURBULENT FLOW VELOCITY PROFILE

SUCTION SURFACE

MACH NUMBER=0.090

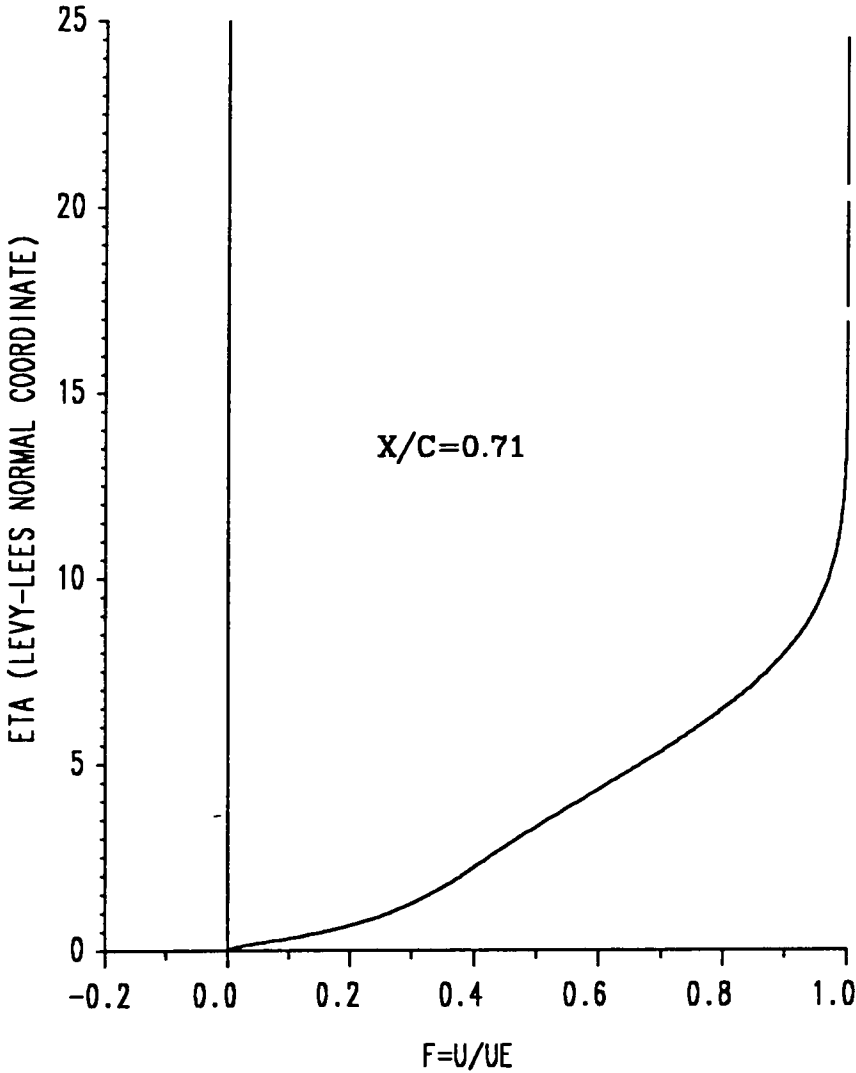


FIGURE 22 GOSTELOW CASCADE TURBULENT FLOW VELOCITY PROFILE

SUCTION SURFACE

MACH NUMBER=0.084

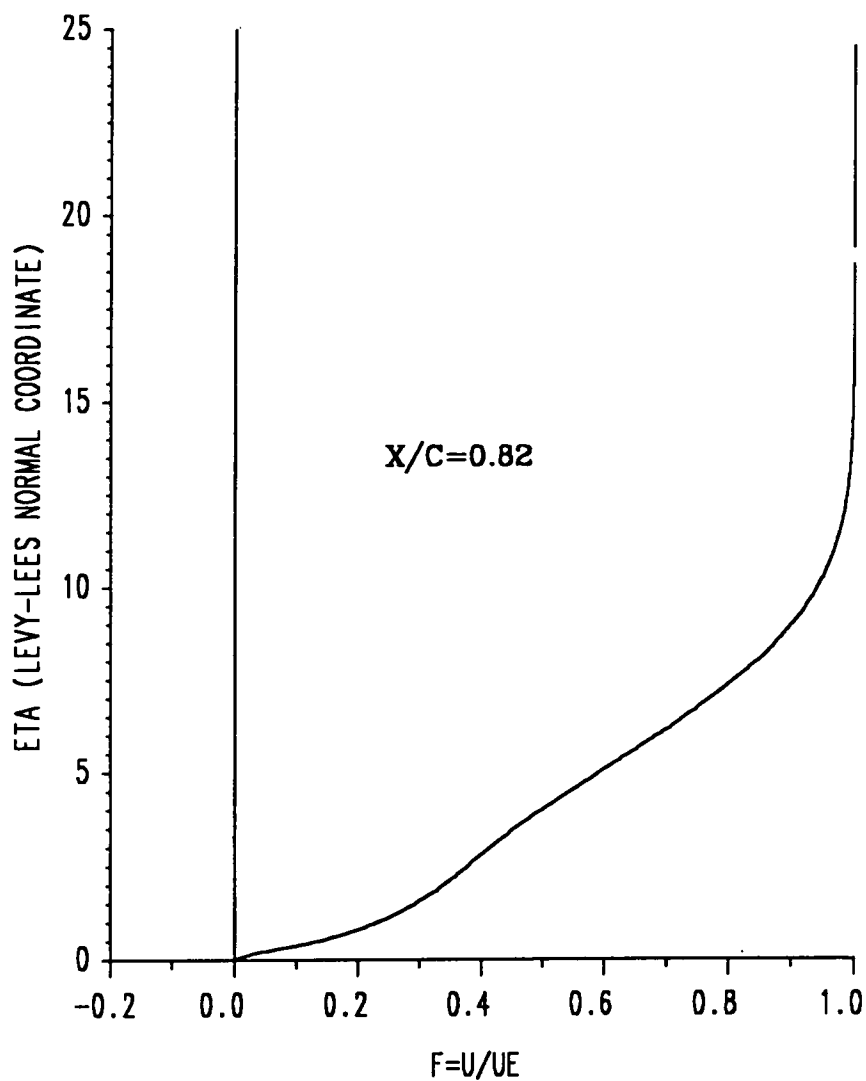


FIGURE 23 GOSTELOW CASCADE TURBULENT FLOW VELOCITY PROFILE

SUCTION SURFACE

MACH NUMBER=0.080

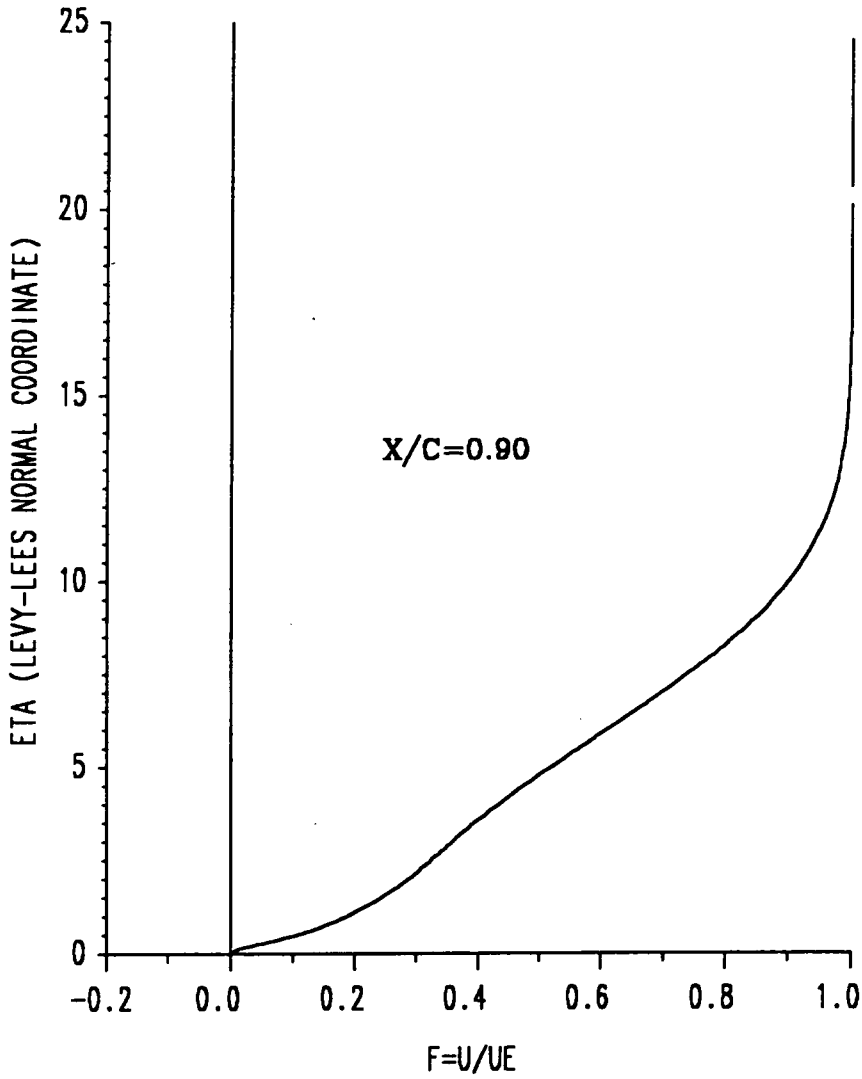


FIGURE 24 GOSTELOW CASCADE TURBULENT FLOW VELOCITY PROFILE

SUCTION SURFACE

MACH NUMBER=0.078

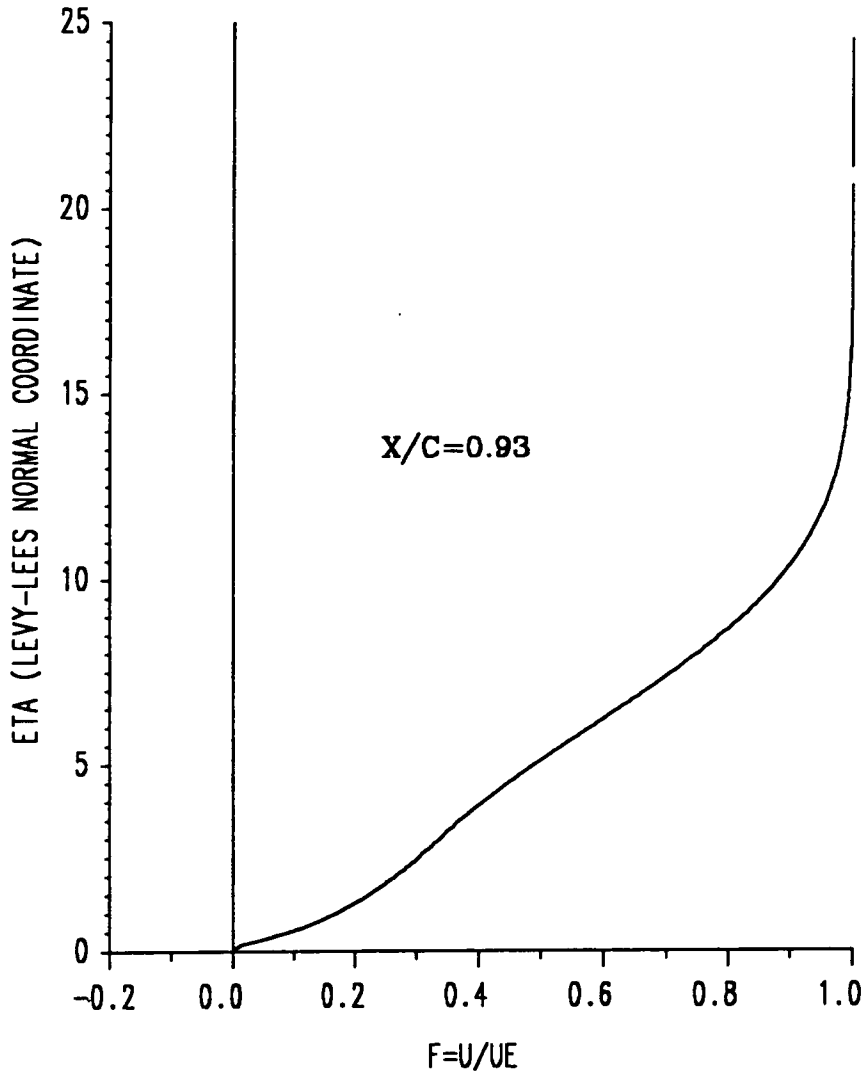


FIGURE 25 GOSTELOW CASCADE TURBULENT FLOW VELOCITY PROFILE

SUCTION SURFACE

MACH NUMBER=0.077

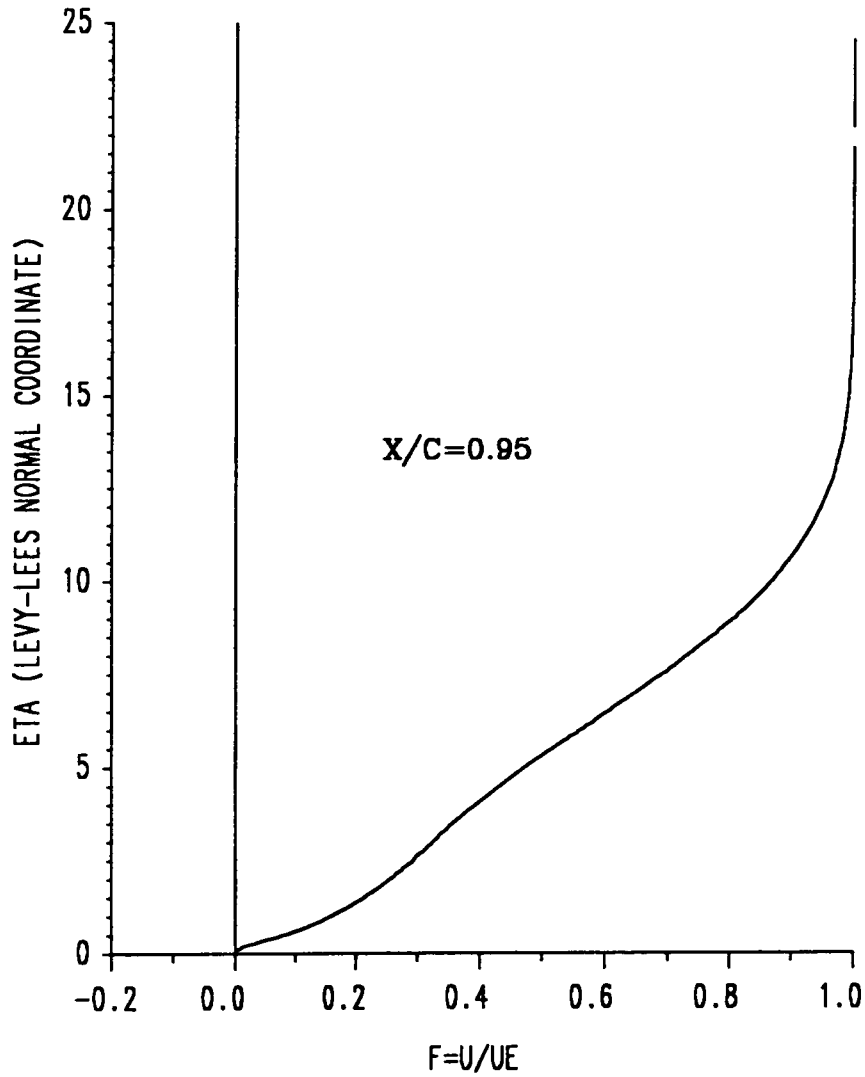


FIGURE 26 GOSTELOW CASCADE TURBULENT FLOW VELOCITY PROFILE

SUCTION SURFACE

MACH NUMBER=0.077

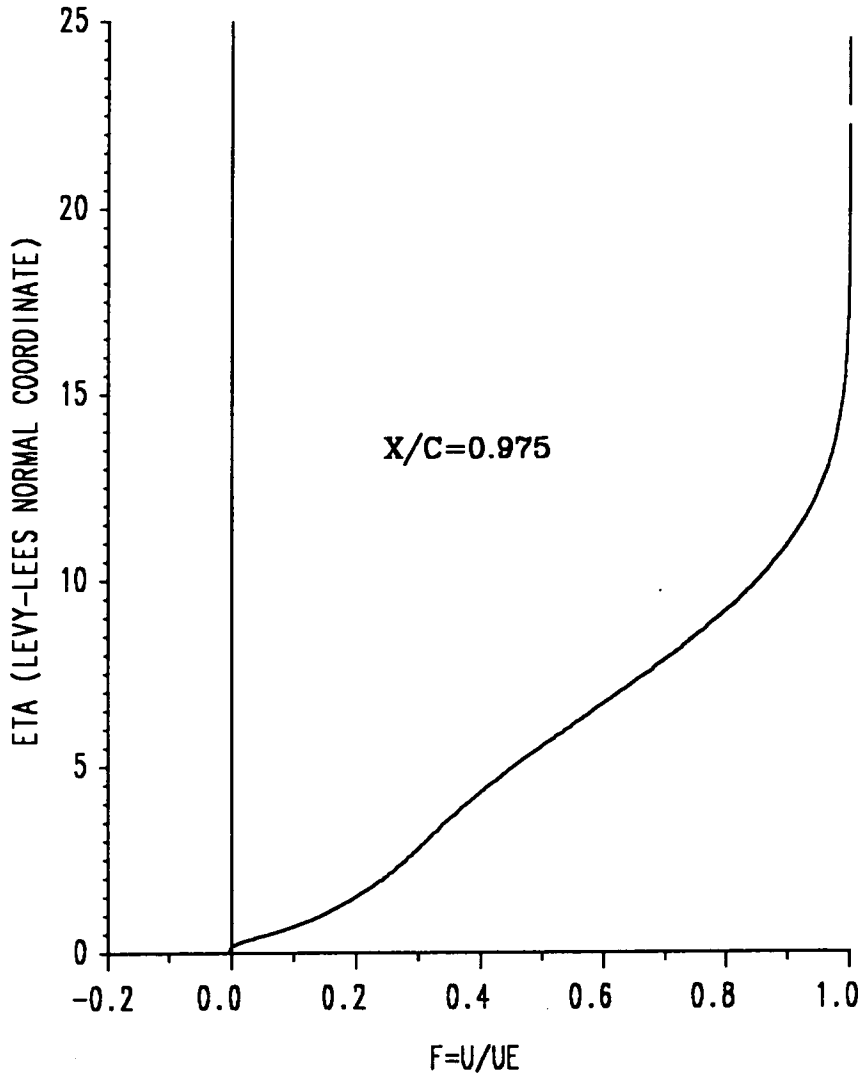


FIGURE 27 GOSTELOW CASCADE TURBULENT FLOW VELOCITY PROFILE

SUCTION SURFACE

MACH NUMBER=0.076

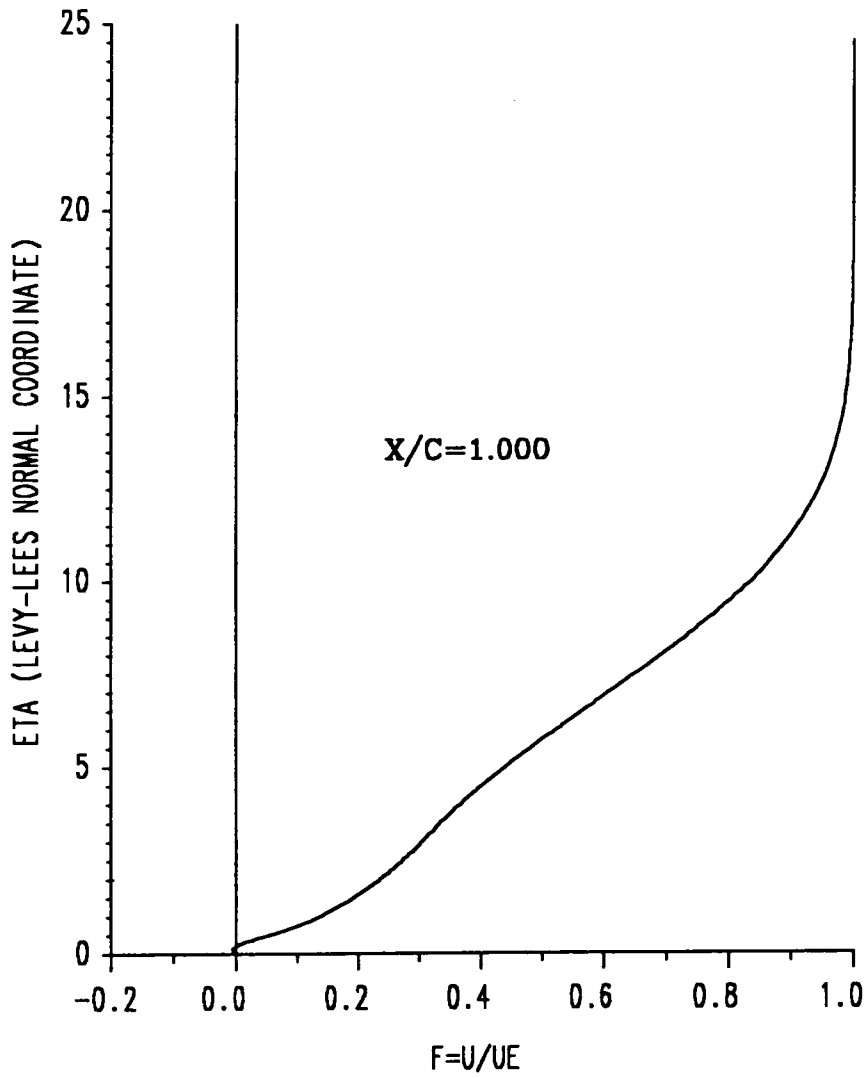


FIGURE 28 GOSTELOW CASCADE TURBULENT FLOW VELOCITY PROFILE

SUCTION SURFACE

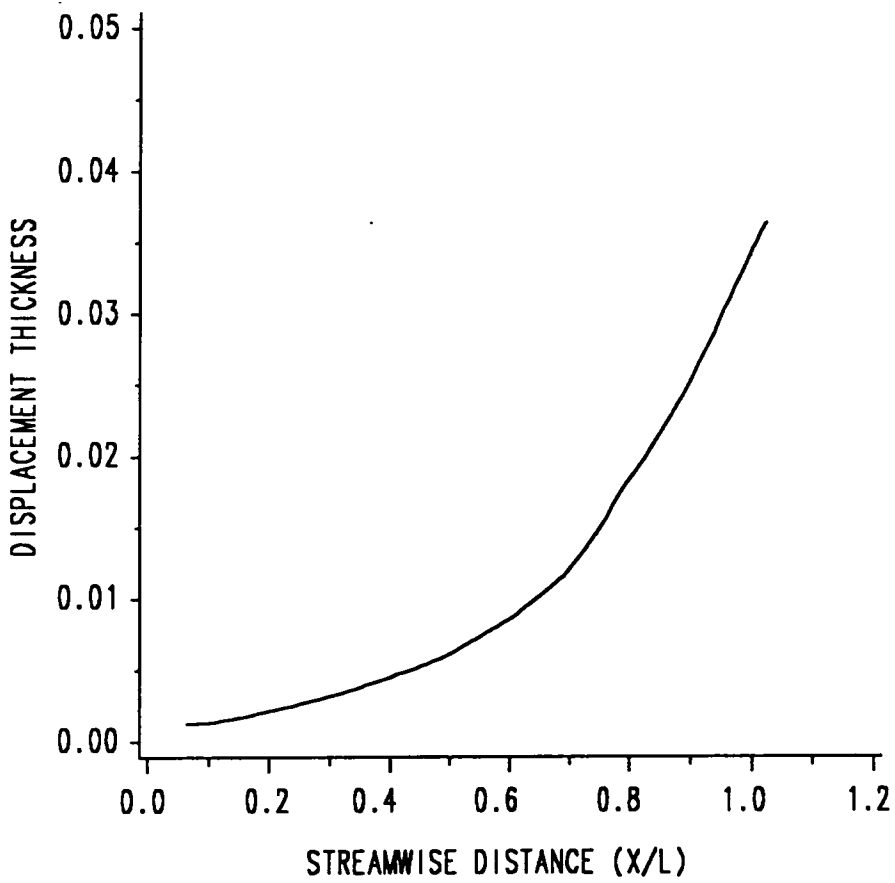


FIGURE 29 GOSTELOW CASCADE DISPLACEMENT THICKNESS DISTRIBUTION

SUCTION SURFACE

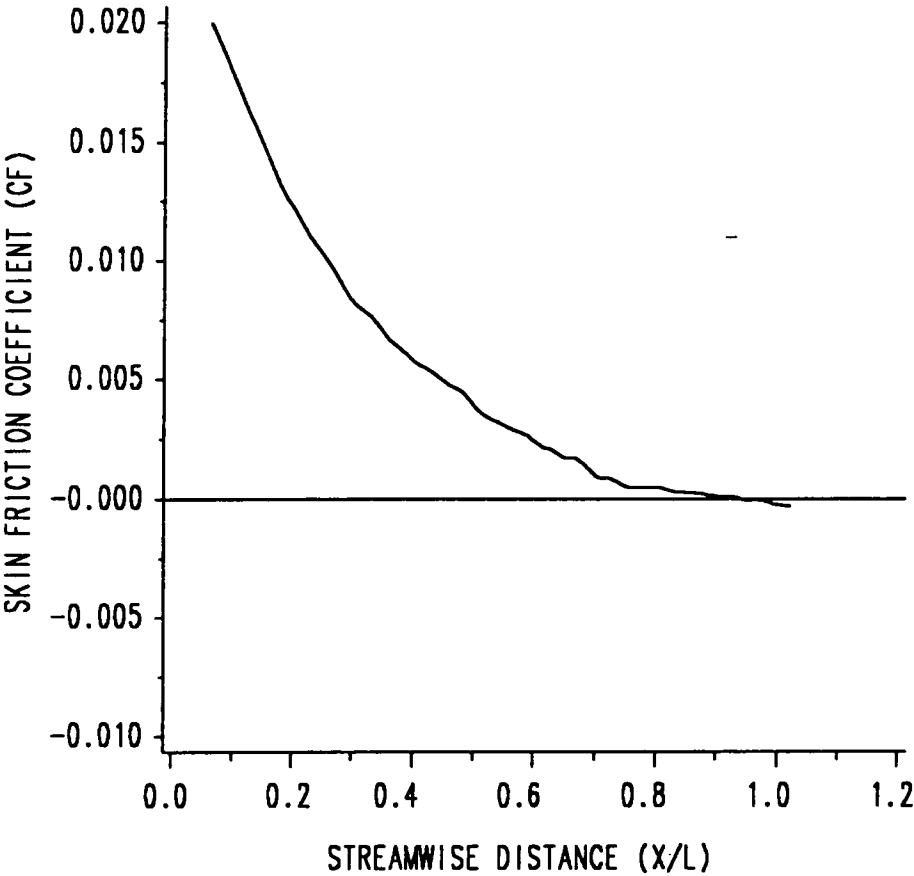


FIGURE 30 GOSTELOW CASCADE SKIN FRICTION COEFFICIENT DISTRIBUTION

PRESSURE SURFACE

----- INVISCID SOLUTION

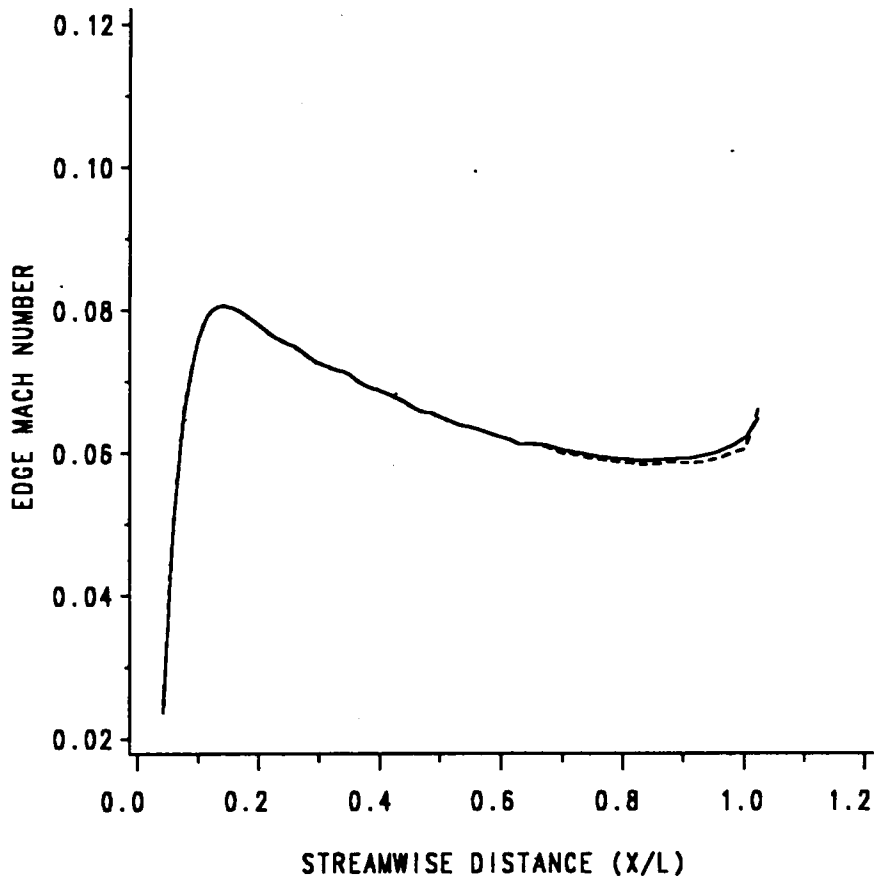


FIGURE 31 GOSTELOW CASCADE EDGE MACH NUMBER

PRESSURE SURFACE

MACH NUMBER=0.066

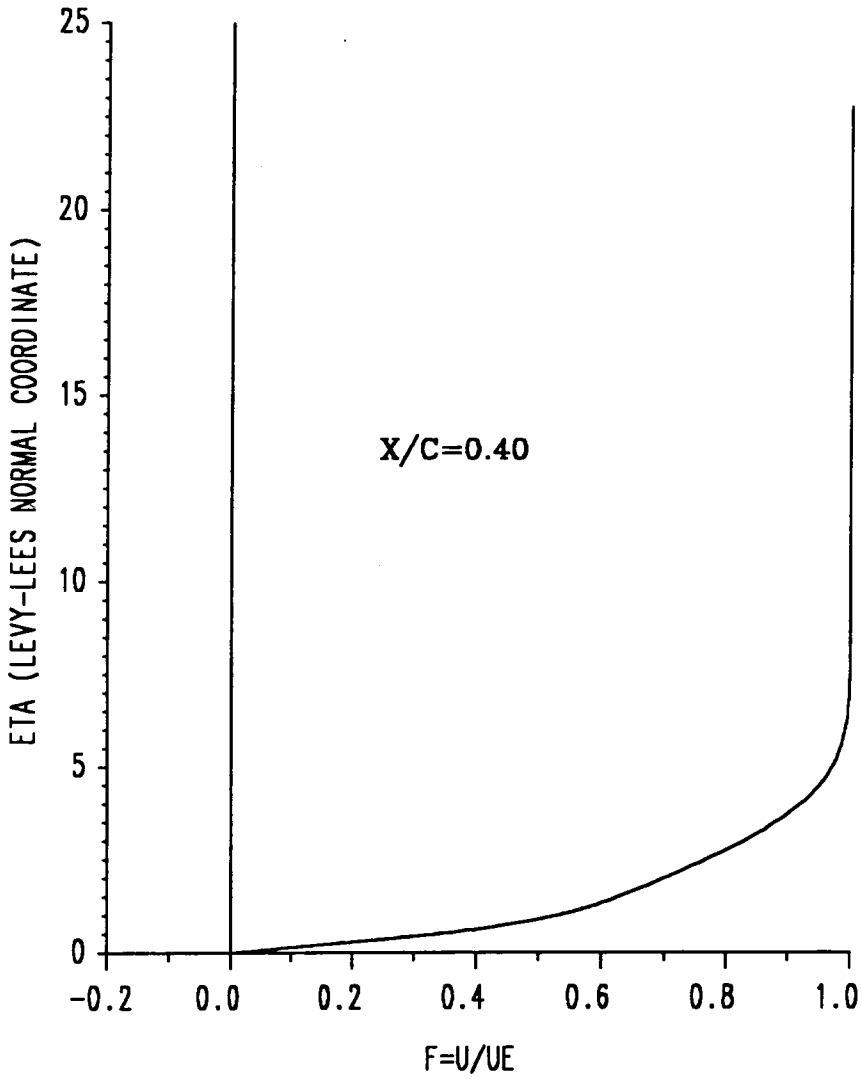


FIGURE 32 GOSTELOW CASCADE TURBULENT FLOW VELOCITY PROFILE

PRESSURE SURFACE

MACH NUMBER=0.064

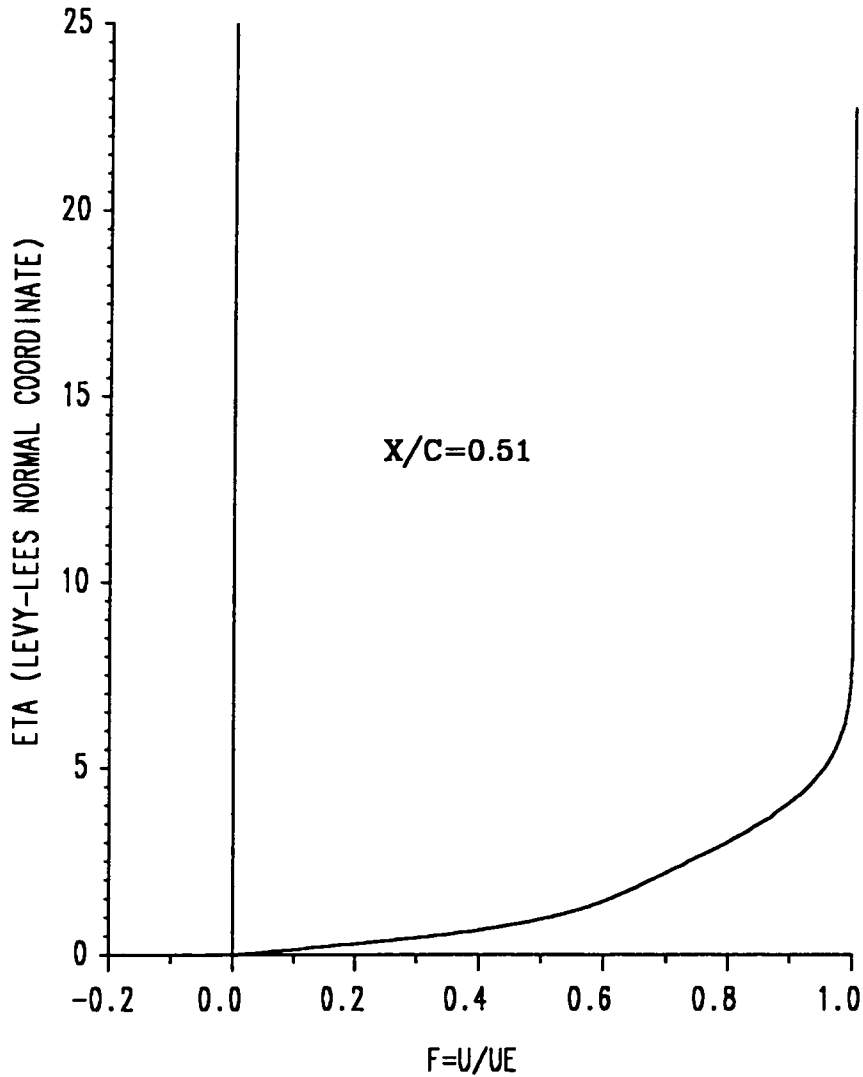


FIGURE 33 GOSTELOW CASCADE TURBULENT FLOW VELOCITY PROFILE

PRESSURE SURFACE

MACH NUMBER=0.061

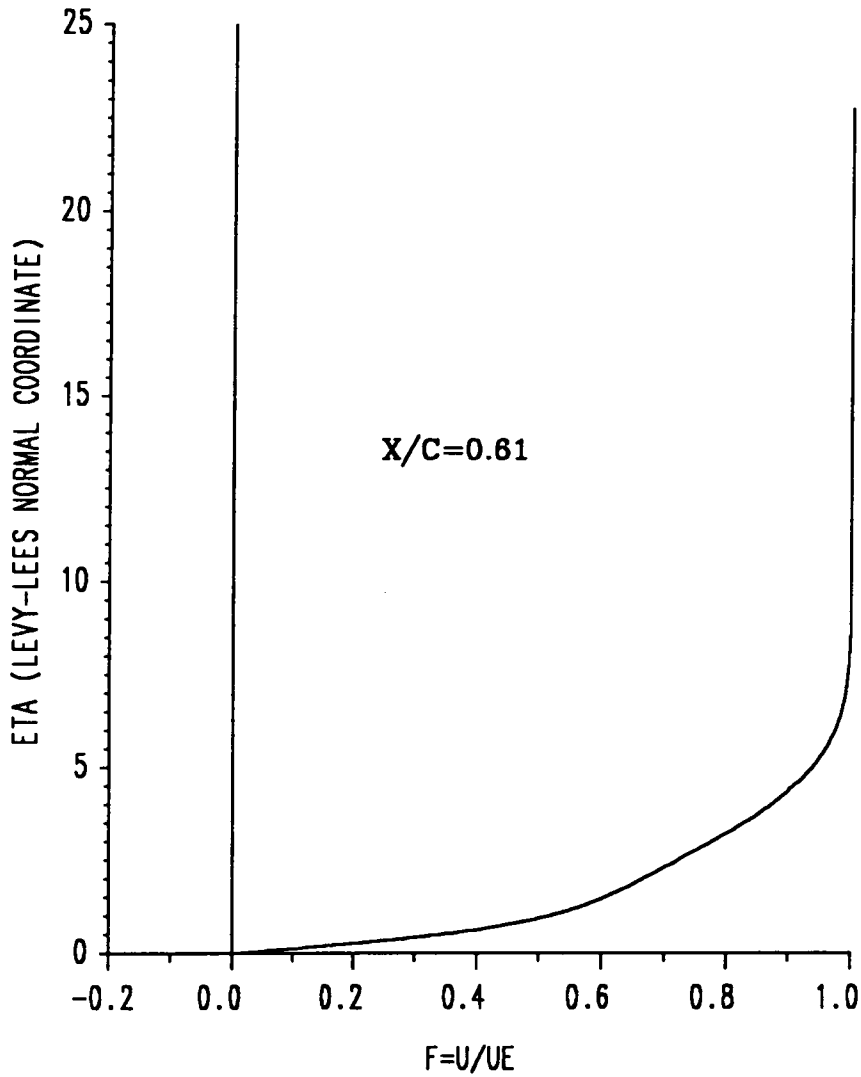


FIGURE 34 GOSTELOW CASCADE TURBULENT FLOW VELOCITY PROFILE

PRESSURE SURFACE

MACH NUMBER=0.060

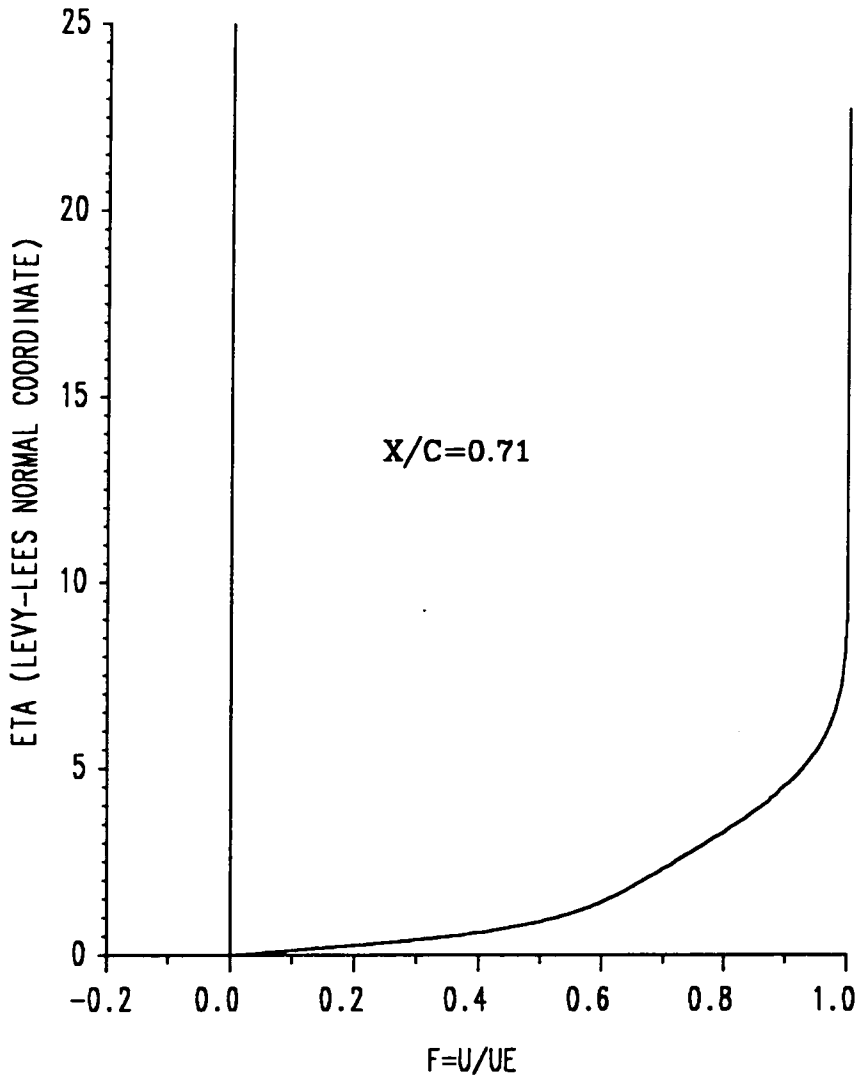


FIGURE 35 GOSTELOW CASCADE TURBULENT FLOW VELOCITY PROFILE

PRESSURE SURFACE

MACH NUMBER=0.059

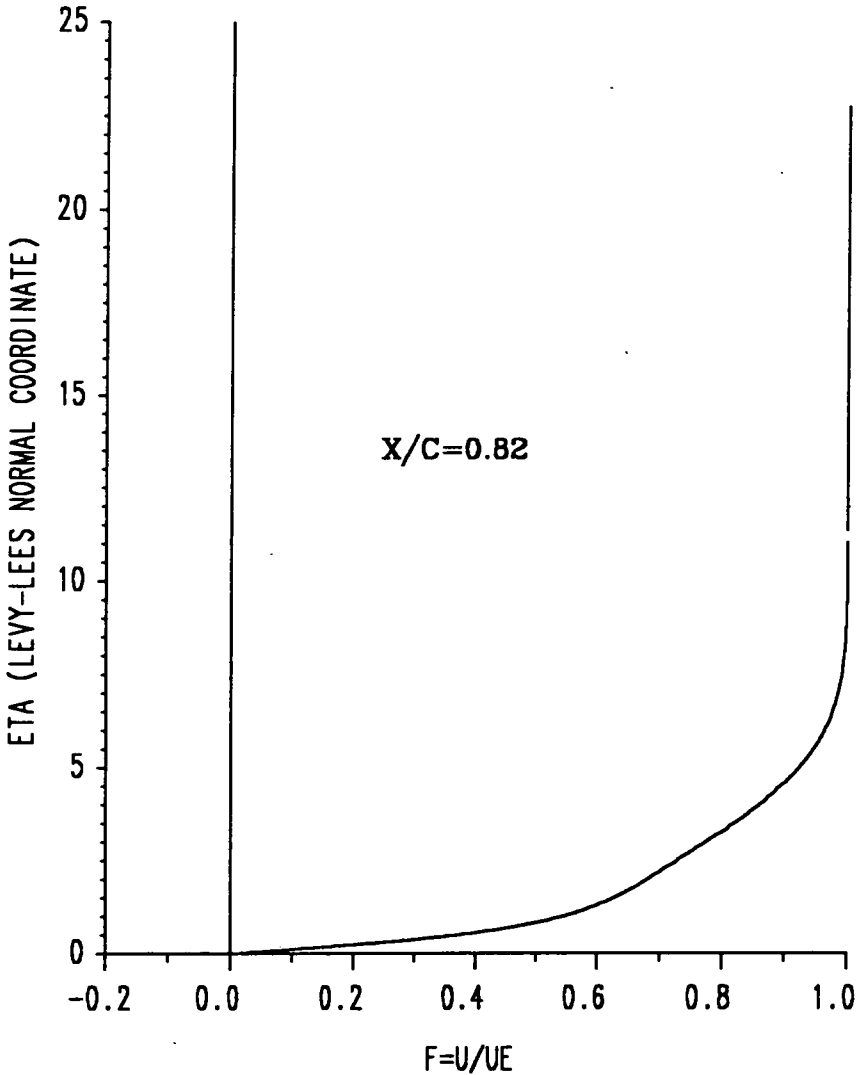


FIGURE 36 GOSTELOW CASCADE TURBULENT FLOW VELOCITY PROFILE

PRESSURE SURFACE

MACH NUMBER=0.060

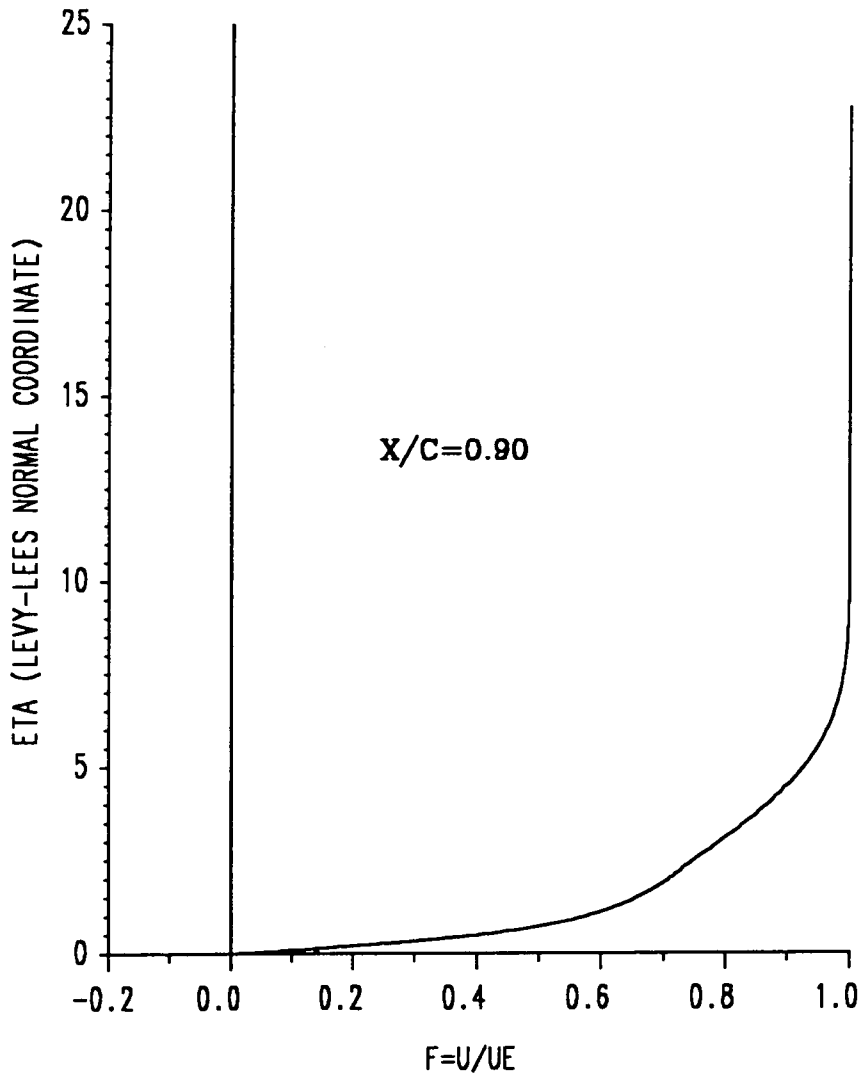


FIGURE 37 GOSTELOW CASCADE TURBULENT FLOW VELOCITY PROFILE

PRESSURE SURFACE

MACH NUMBER=0.065

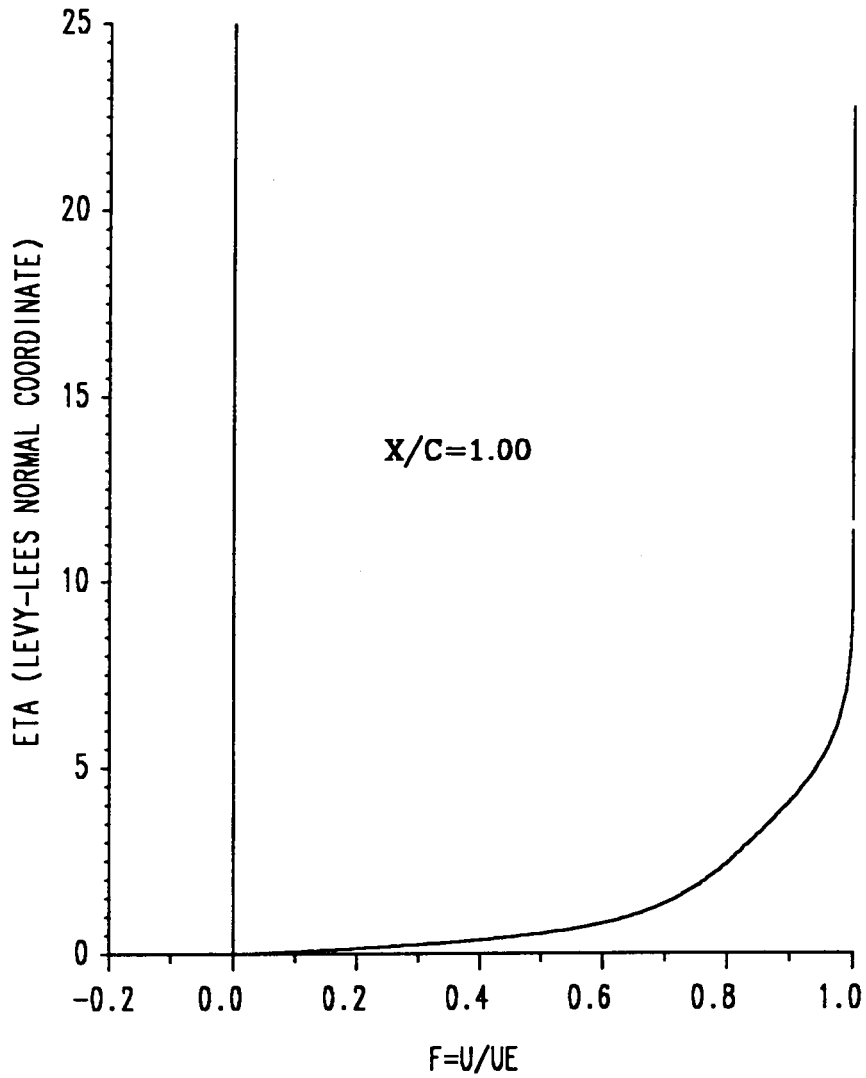


FIGURE 38 GOSTELOW CASCADE TURBULENT FLOW VELOCITY PROFILE

PRESSURE SURFACE



FIGURE 39 GOSTELOW CASCADE SKIN FRICTION COEFFICIENT DISTRIBUTION

PRESSURE SURFACE

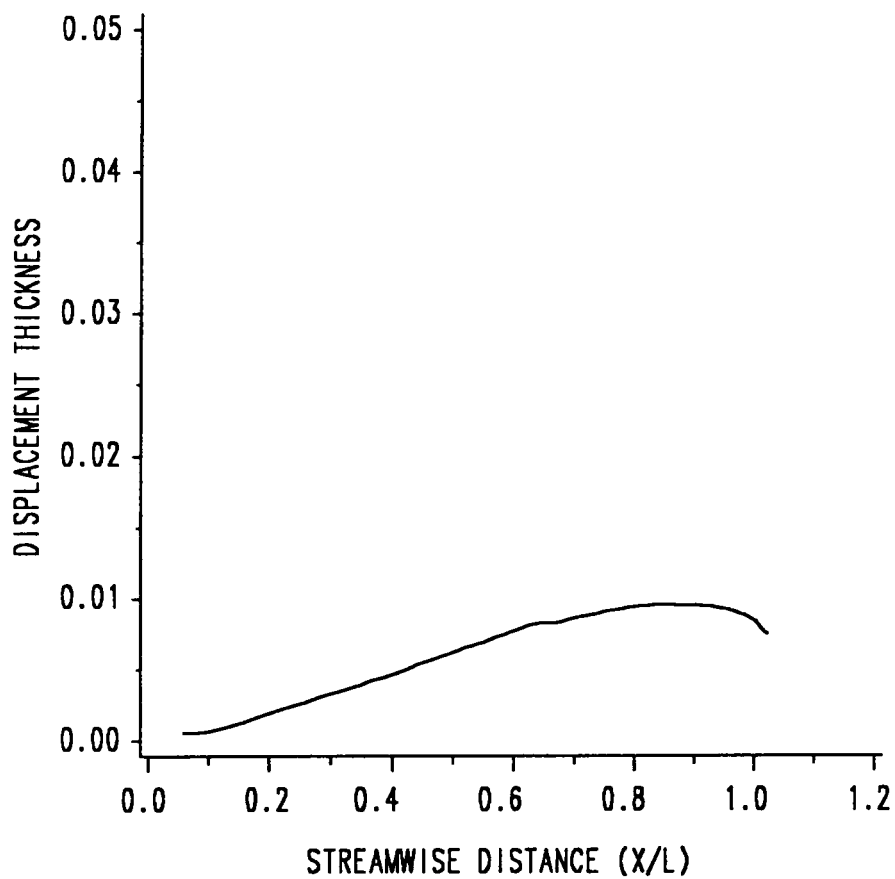
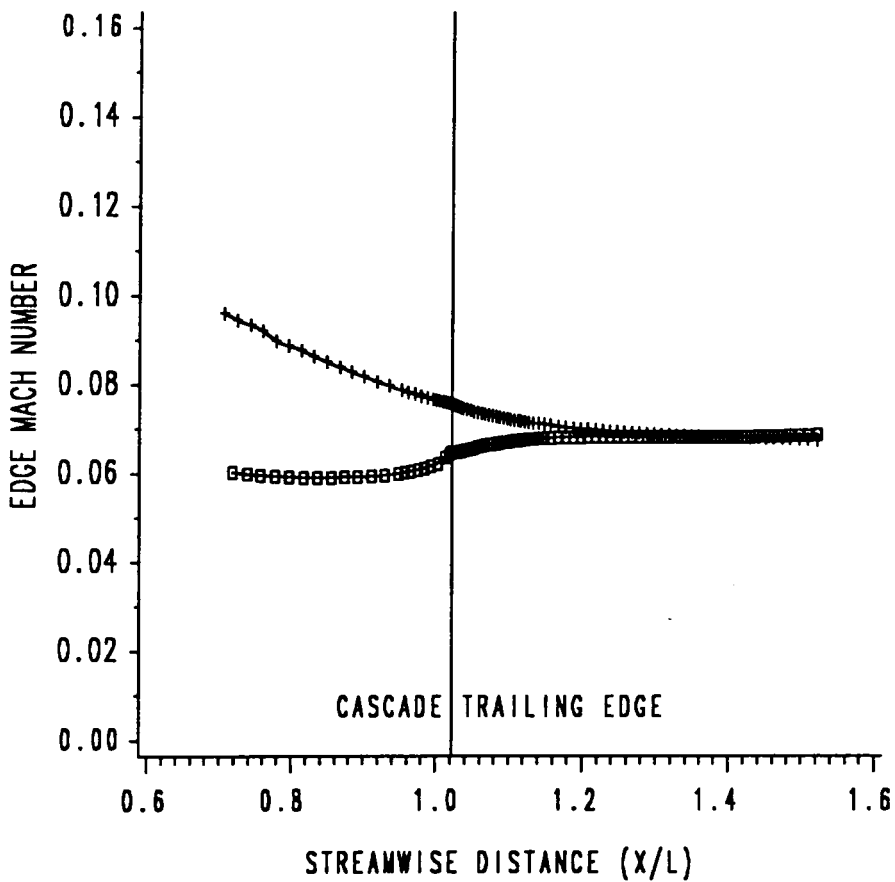
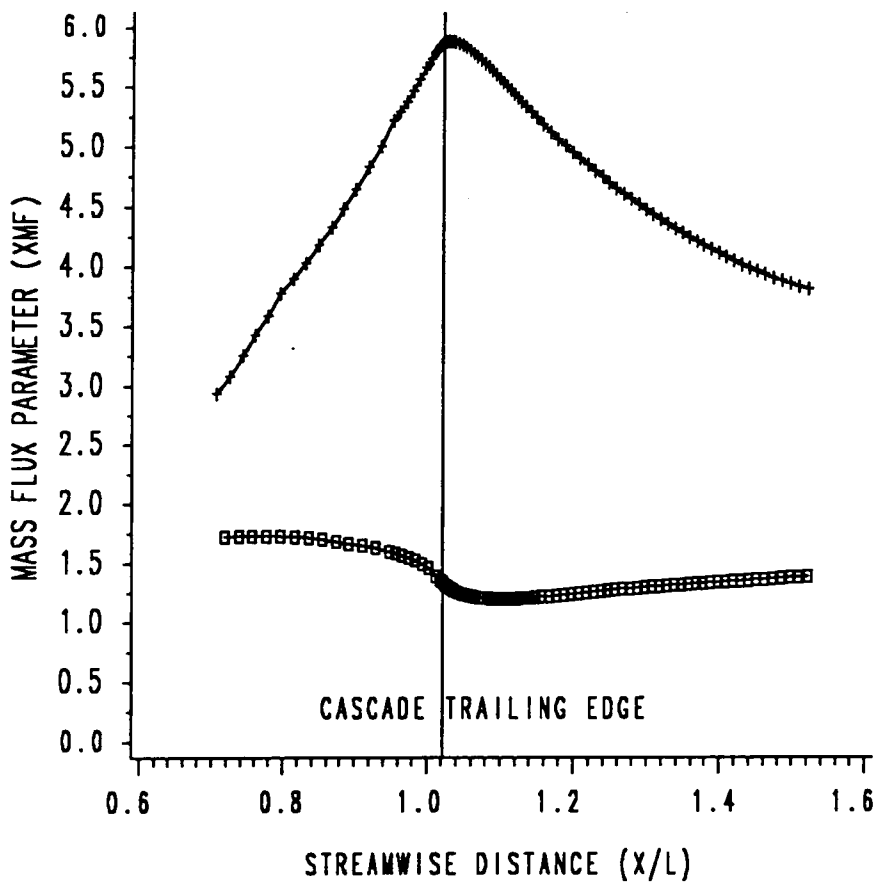


FIGURE 40 GOSTELOW CASCADE DISPLACEMENT THICKNESS DISTRIBUTION



CASE	+ + +	SUCTION SIDE	o - o - o	PRESSURE SIDE
------	-------	--------------	-----------	---------------

FIGURE 41 GOSTELOW CASCADE WAKE EDGE MACH NUMBER



CASE +--+ SUCTION SIDE □-□-□ PRESSURE SIDE

FIGURE 42 GOSTELOW CASCADE WAKE MASS FLUX PARAMETER

SUCTION SURFACE MACH NUMBER=0.075
PRESSURE SURFACE MACH NUMBER=0.065

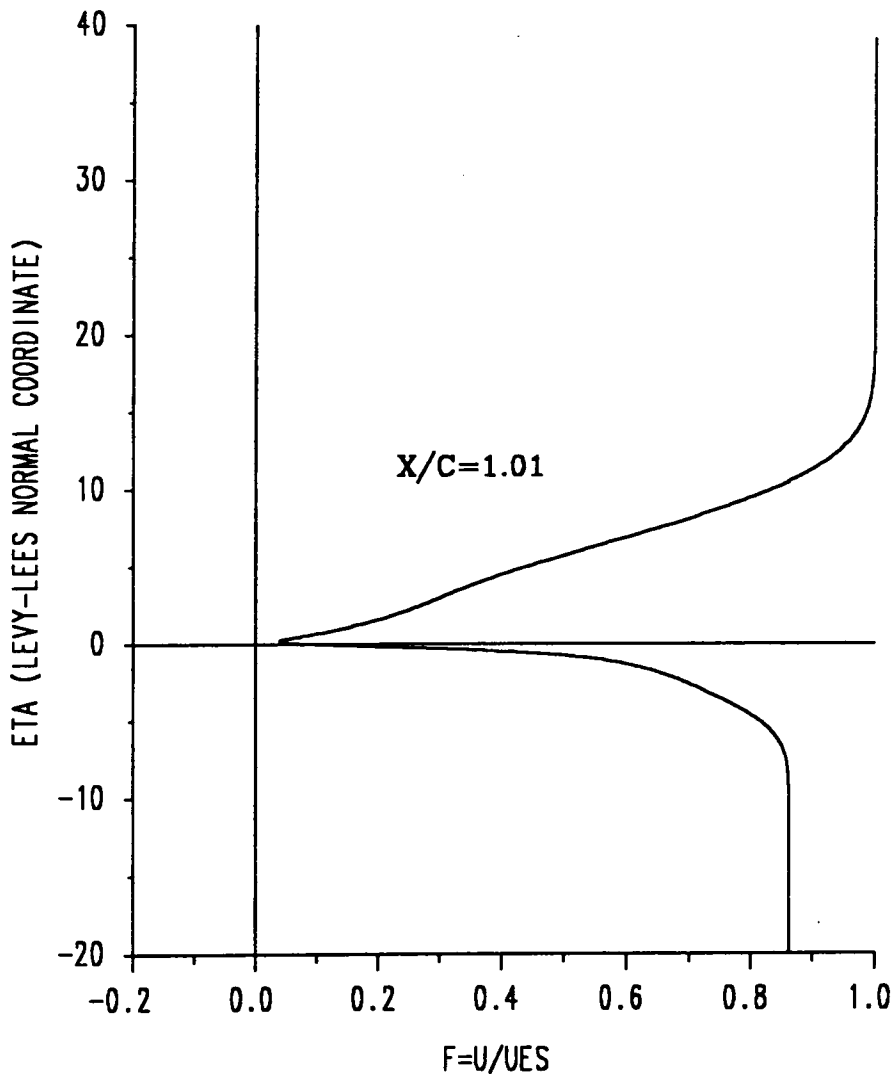


FIGURE 43 GOSTELOW CASCADE TURBULENT FLOW WAKE VELOCITY PROFILE

SUCTION SURFACE WACH NUMBER=0.073
PRESSURE SURFACE WACH NUMBER=0.066

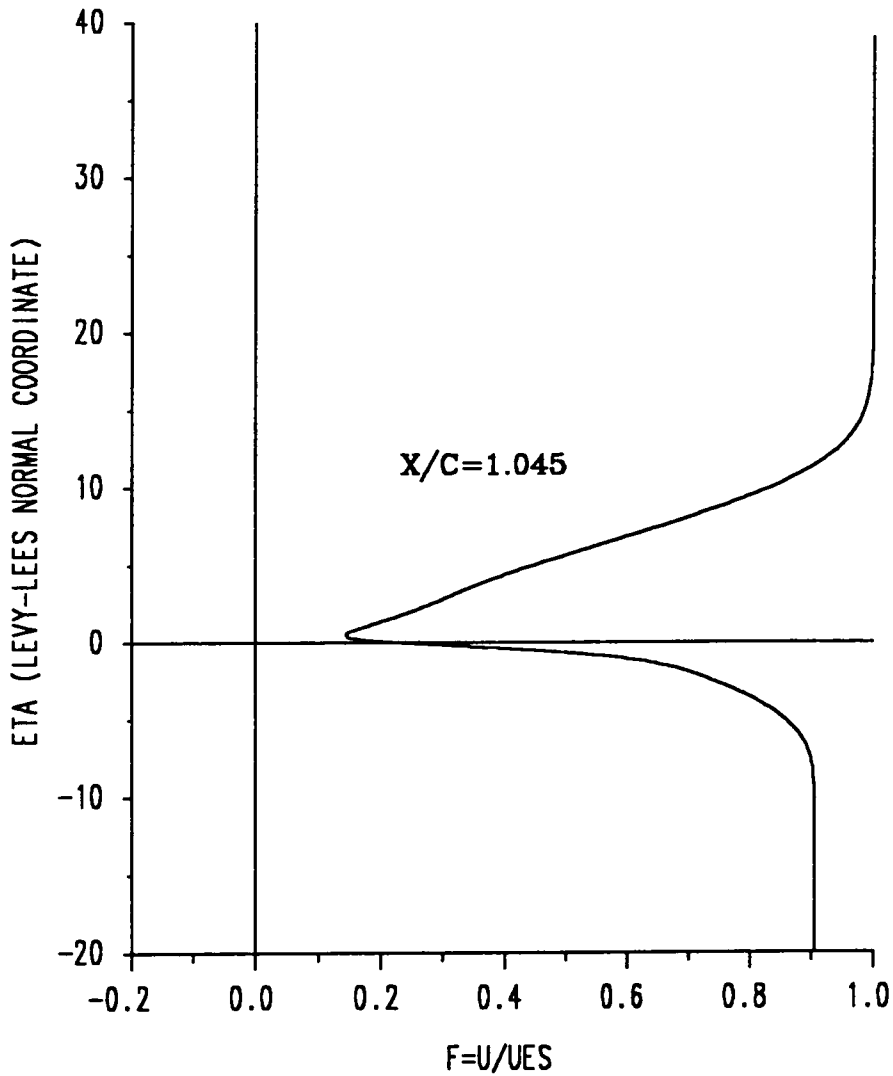


FIGURE 44 GOSTELOW CASCADE TURBULENT FLOW WAKE VELOCITY PROFILE

SUCTION SURFACE MACH NUMBER=0.072
PRESSURE SURFACE MACH NUMBER=0.068

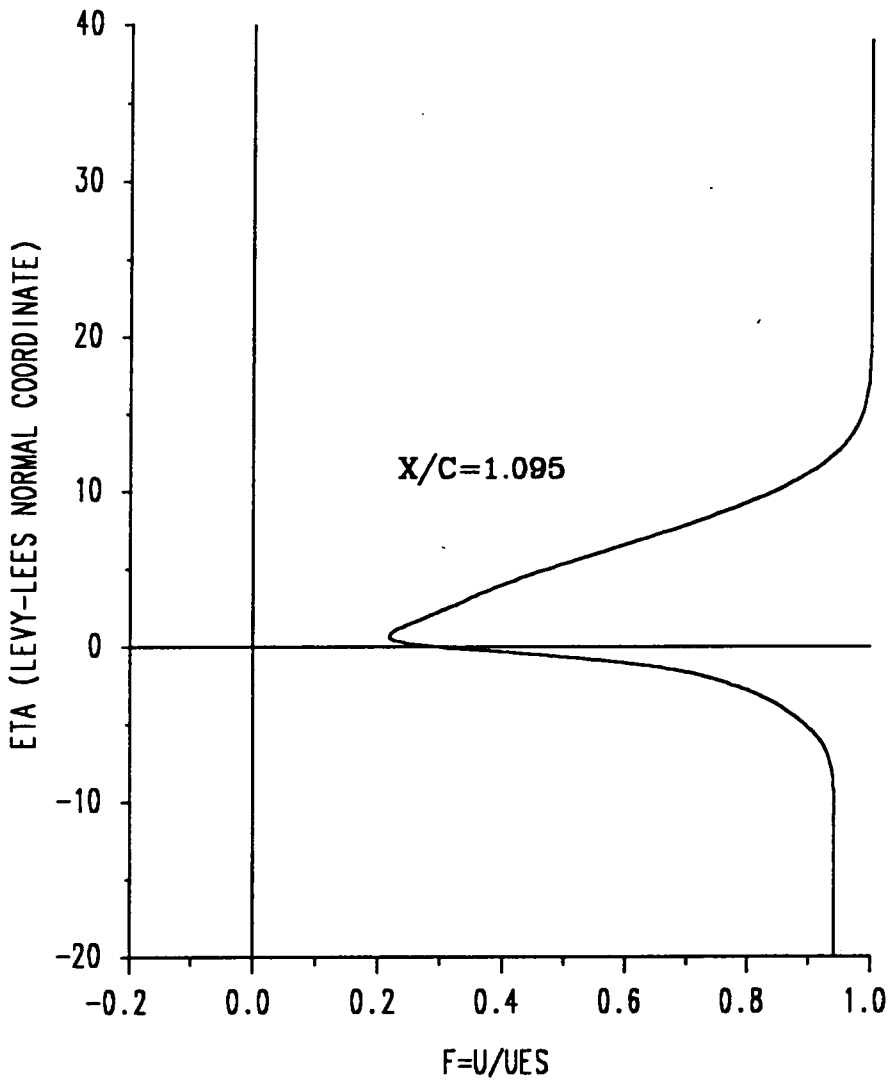


FIGURE 45 GOSTELOW CASCADE TURBULENT FLOW WAKE VELOCITY PROFILE

SUCTION SURFACE WACH NUMBER=0.069
PRESSURE SURFACE WACH NUMBER=0.068

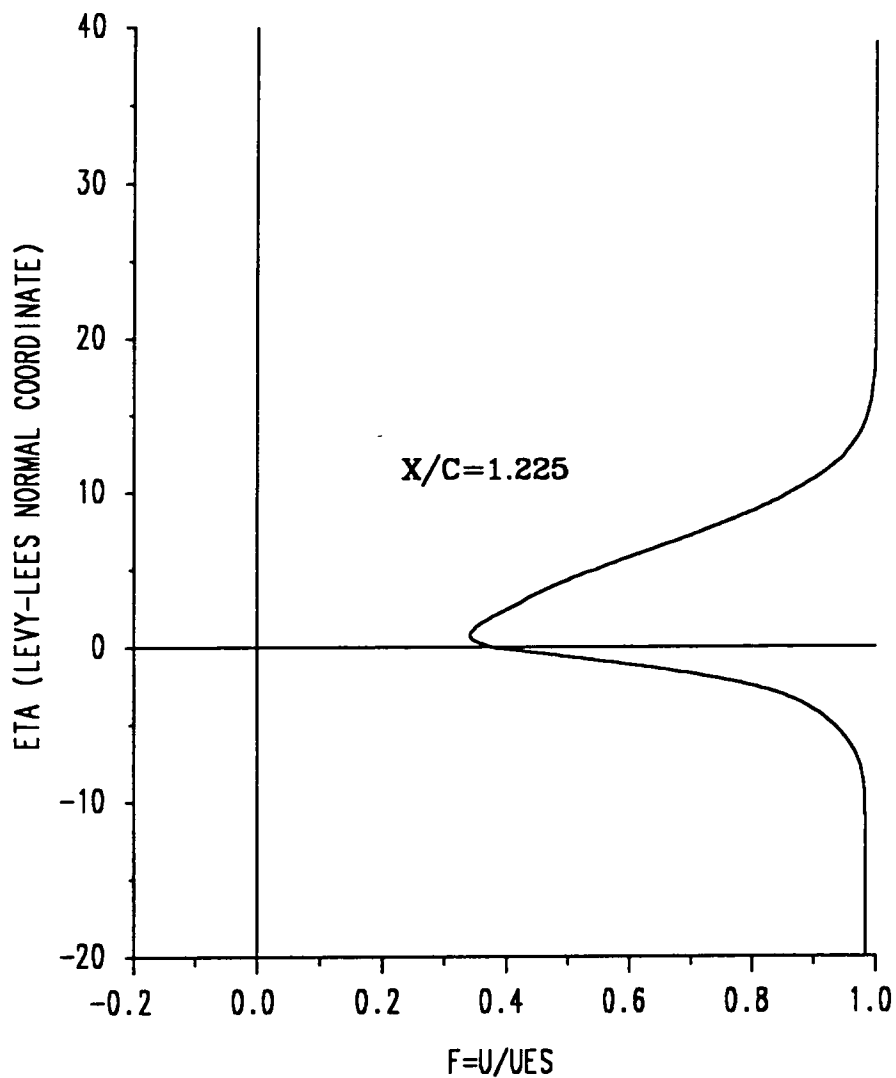


FIGURE 46 GOSTELOW CASCADE TURBULENT FLOW WAKE VELOCITY PROFILE

SUCTION SURFACE MACH NUMBER=0.069
PRESSURE SURFACE MACH NUMBER=0.068

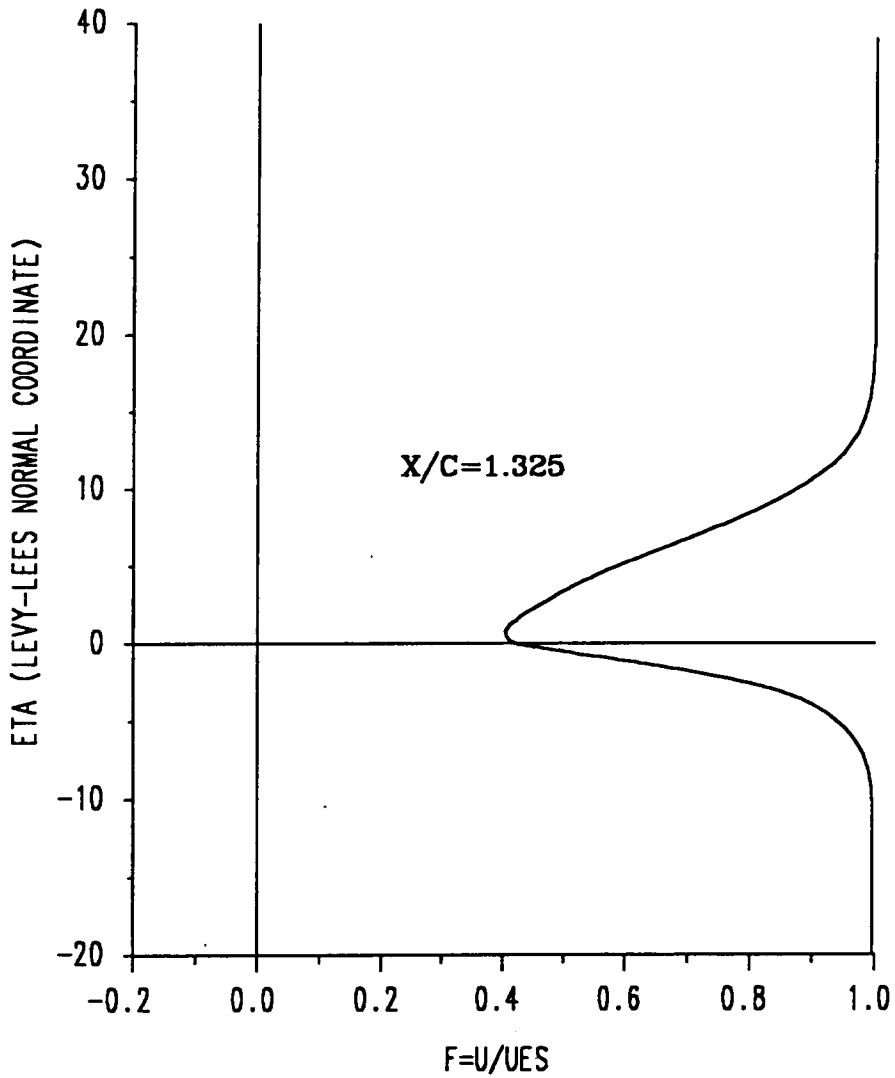


FIGURE 47 GOSTELOW CASCADE TURBULENT FLOW WAKE VELOCITY PROFILE

SUCTION SURFACE MACH NUMBER=0.068
PRESSURE SURFACE MACH NUMBER=0.068

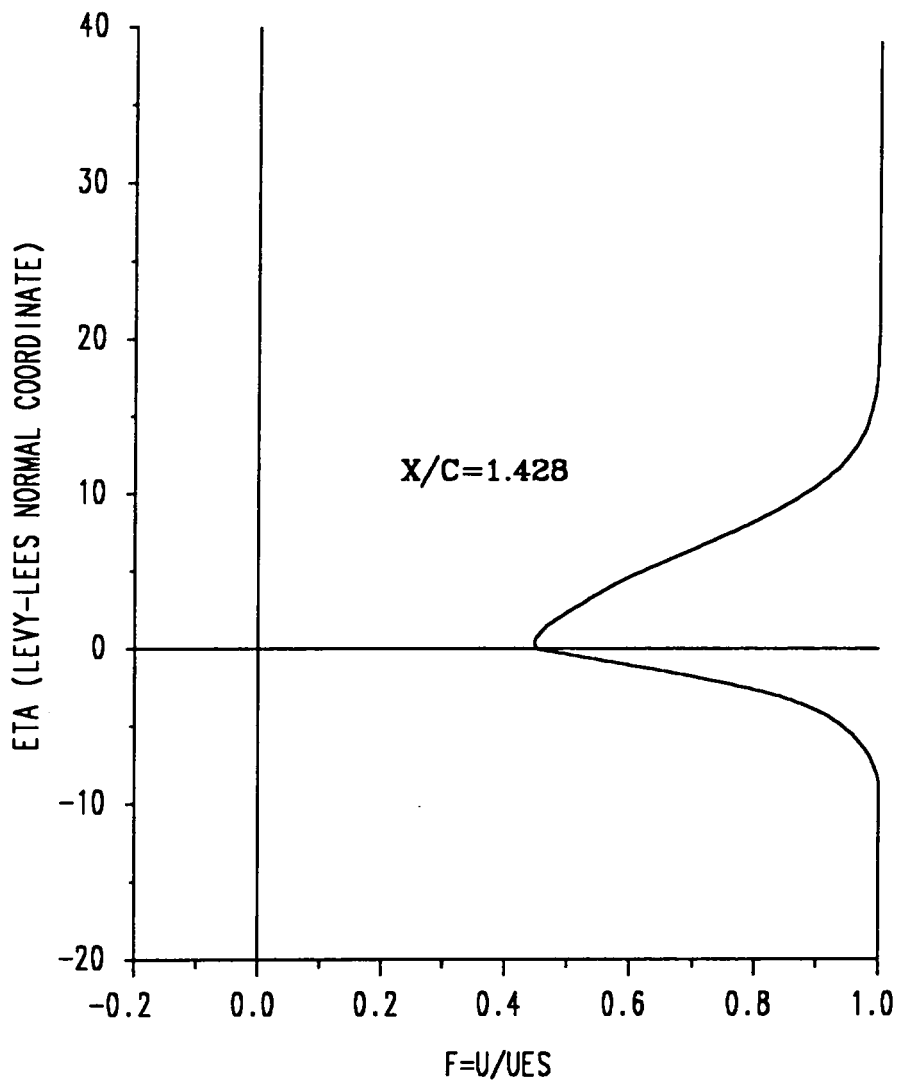


FIGURE 48 GOSTELOW CASCADE TURBULENT FLOW WAKE VELOCITY PROFILE

SUCTION SURFACE MACH NUMBER=0.068
PRESSURE SURFACE MACH NUMBER=0.069

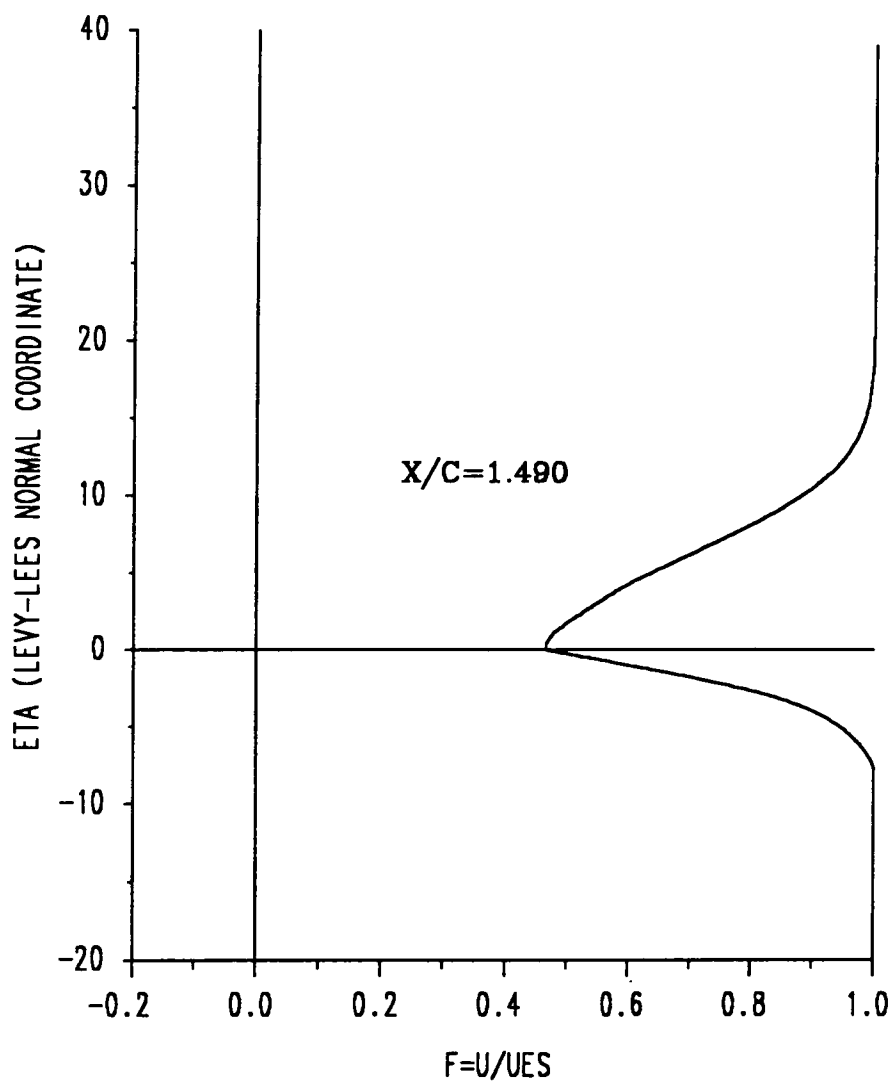


FIGURE 49 GOSTELOW CASCADE TURBULENT FLOW WAKE VELOCITY PROFILE

SUCTION SURFACE MACH NUMBER=0.075
PRESSURE SURFACE MACH NUMBER=0.065

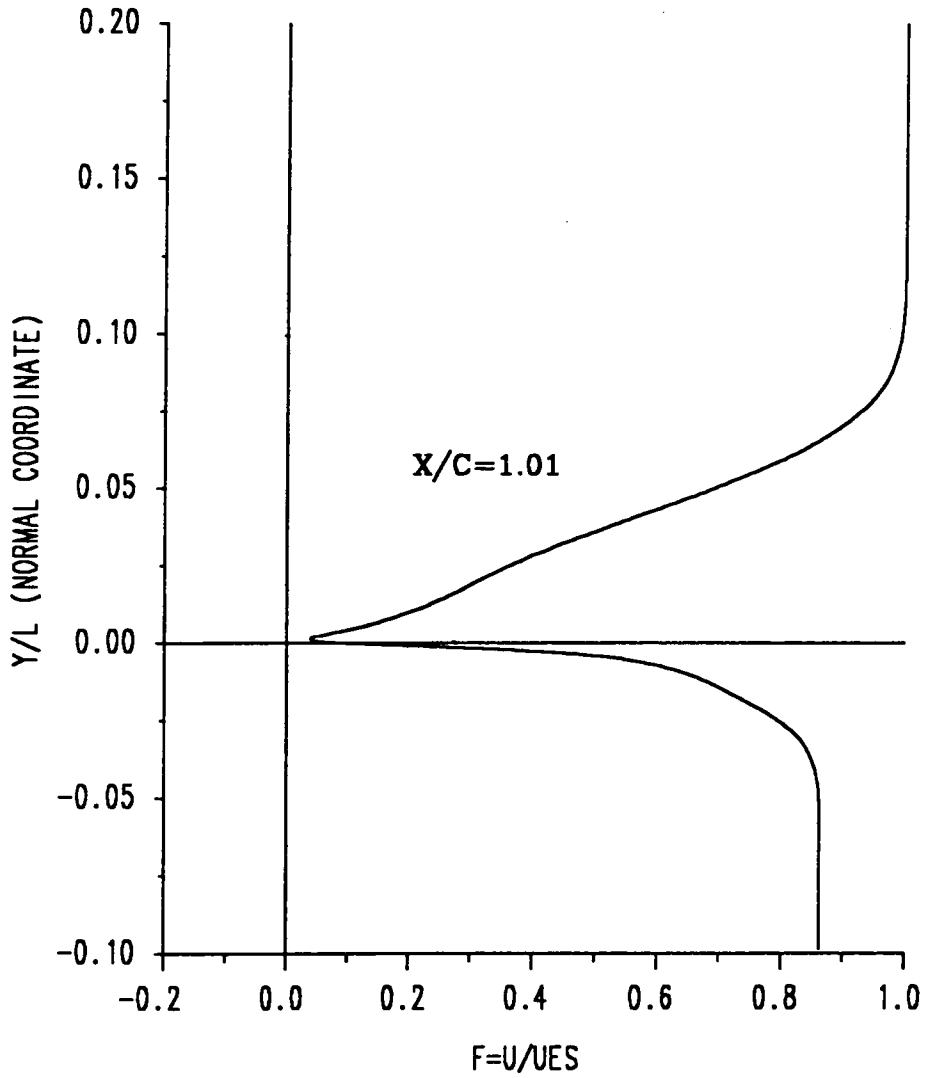


FIGURE 50 GOSTELOW CASCADE TURBULENT FLOW WAKE VELOCITY PROFILE

SUCTION SURFACE MACH NUMBER=0.069
PRESSURE SURFACE MACH NUMBER=0.068

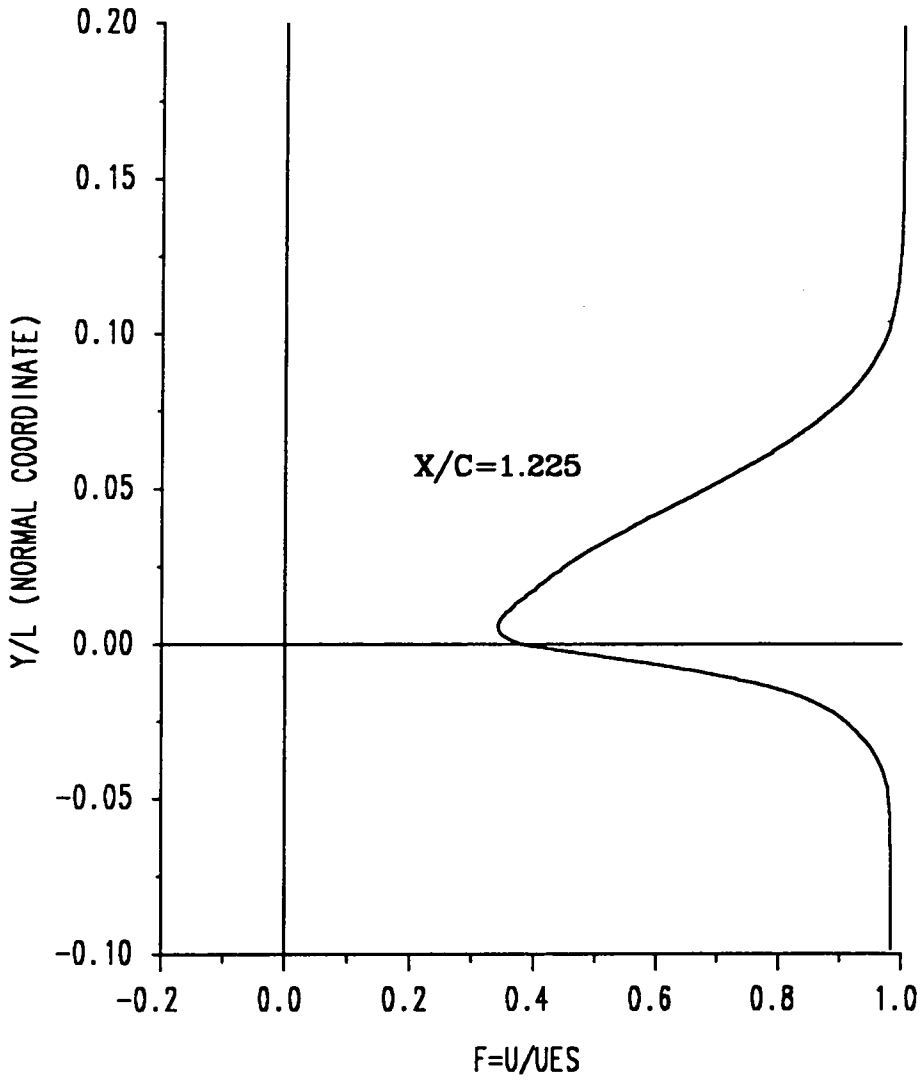


FIGURE 51 GOSTELOW CASCADE TURBULENT FLOW WAKE VELOCITY PROFILE

SUCTION SURFACE MACH NUMBER=0.068
PRESSURE SURFACE MACH NUMBER=0.069

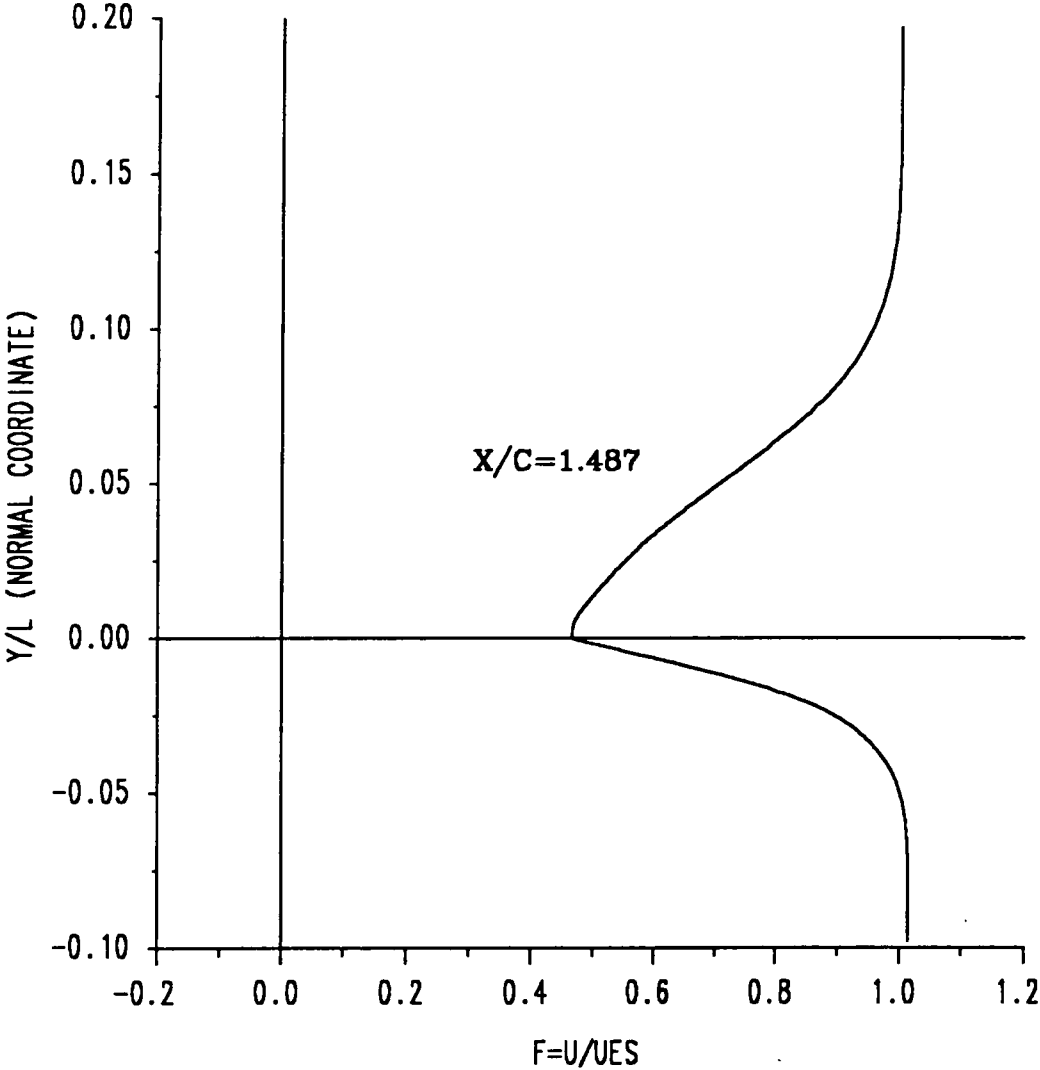
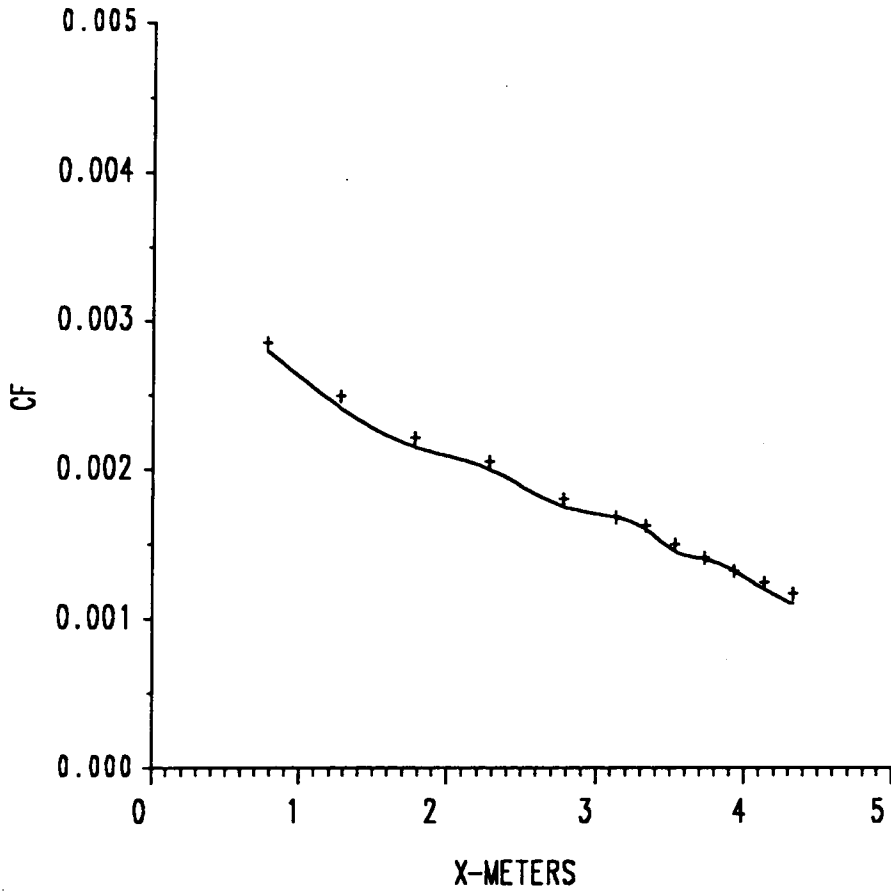


FIGURE 52 GOSTELOW CASCADE TURBULENT FLOW WAKE VELOCITY PROFILE

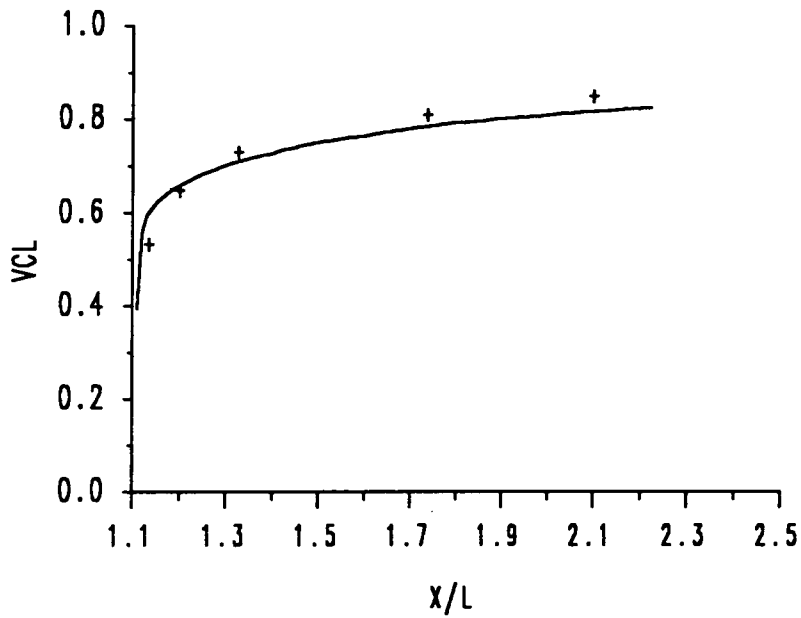
LUDWIG AND TILLMAN DATA
MILD ADVERSE PRESSURE GRADIENT



CASE + + + TEST DATA ——— CURRENT ANALYSIS

FIGURE 53 1968 STANFORD CONFERENCE SKIN FRICTION DATA

CHEVRAY WAKE DATA
SYMMETRIC WAKE



CASE	—	CURRENT ANALYSIS	+	+	+	TEST DATA
------	---	------------------	---	---	---	-----------

FIGURE 54 CENTERLINE VELOCITY FOR FLAT PLATE TURBULENT WAKE

CASCADE DATA

GAP/CHORD=0.700
STAGGER ANGLE=15.7

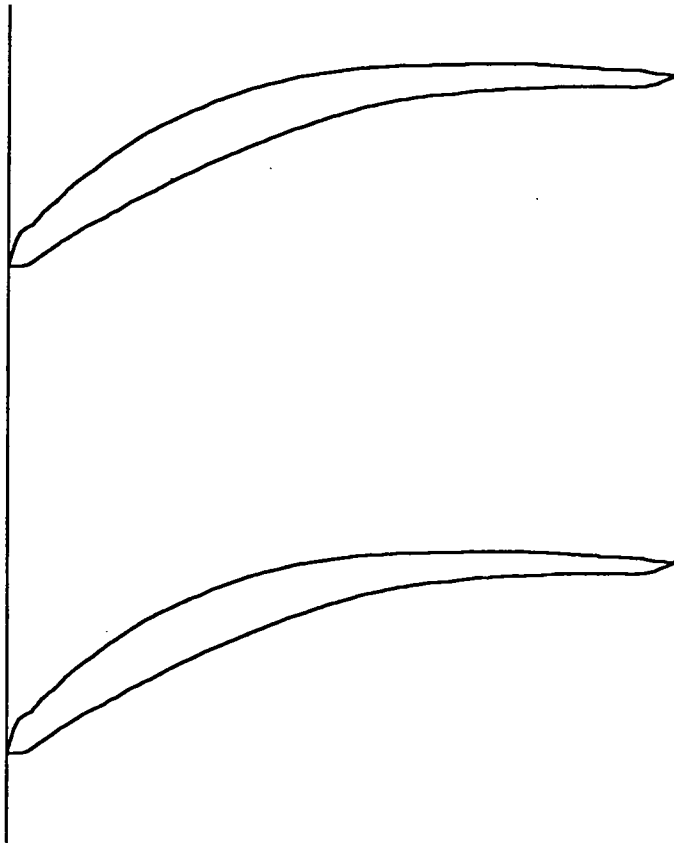


FIGURE 55 SUPERCRITICAL CASCADE BUILD 1

SUCTION SURFACE
EXPERIMENTAL DATA

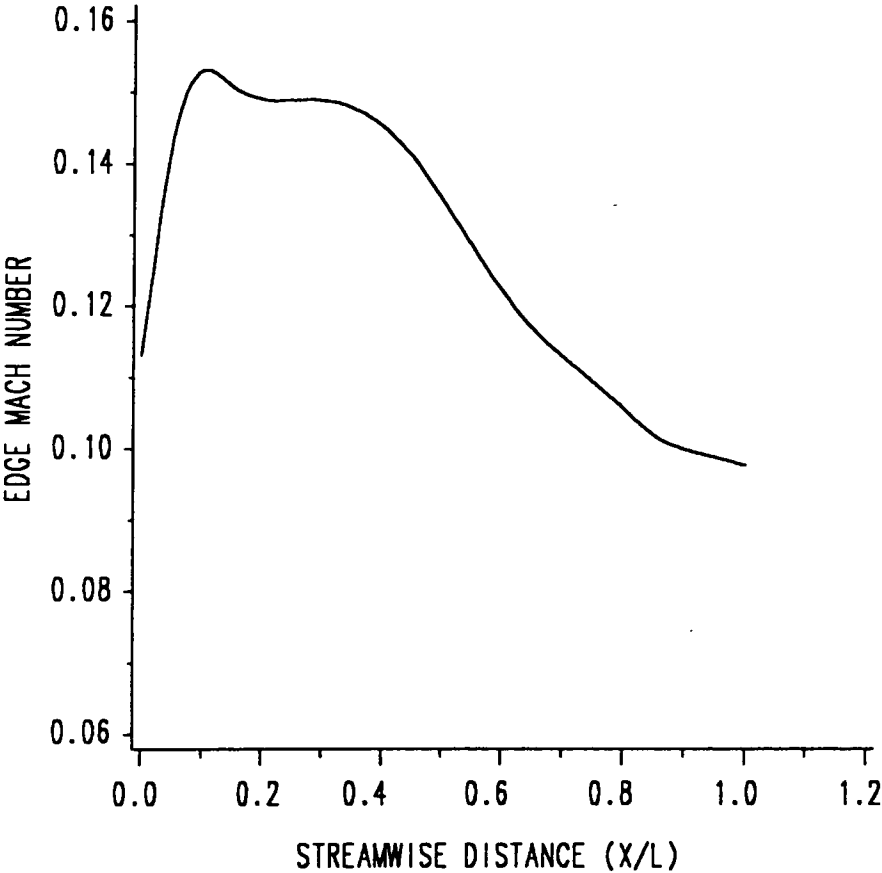


FIGURE 56 SUPERCRITICAL CASCADE BUILD 1 EDGE MACH NUMBER

PRESSURE SURFACE
EXPERIMENTAL DATA

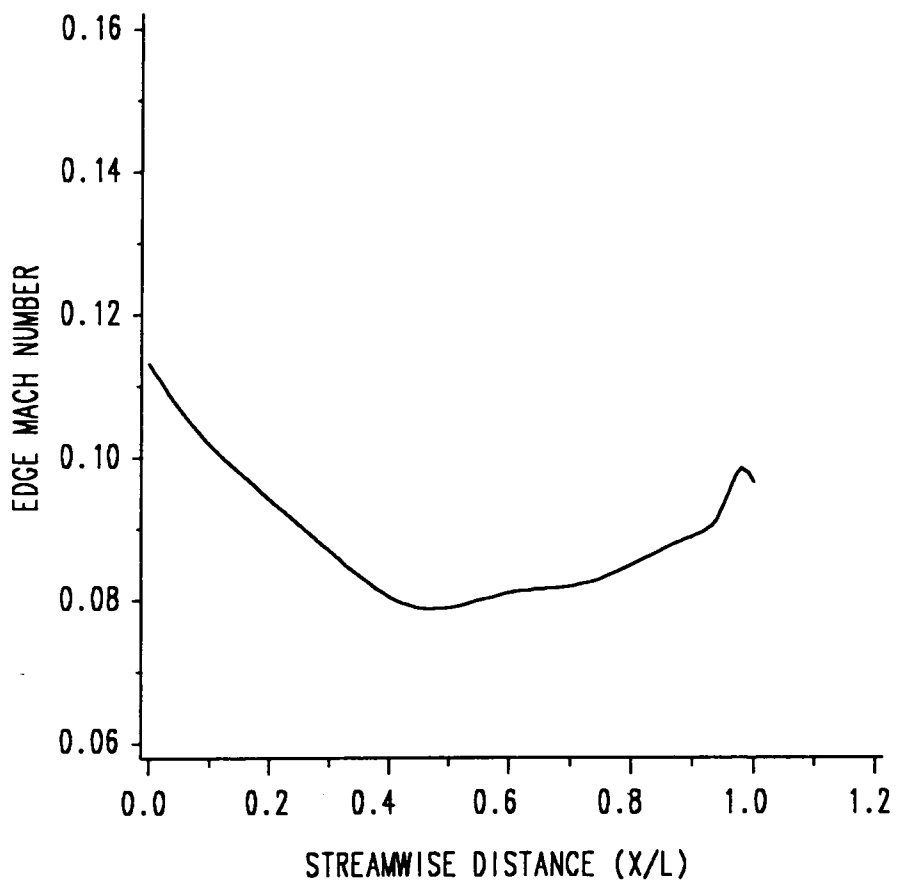
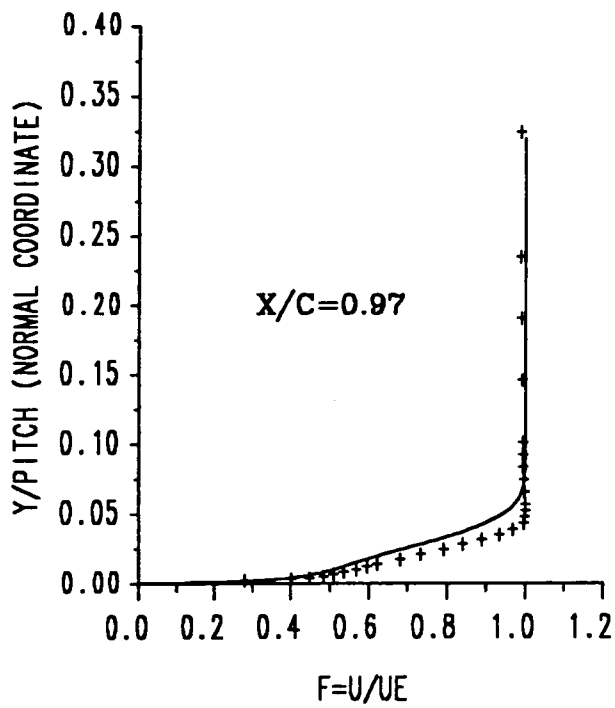


FIGURE 57 SUPERCritical CASCADE BUILD 1 EDGE MACH NUMBER

SUCTION SURFACE

MACH NUMBER=0.099

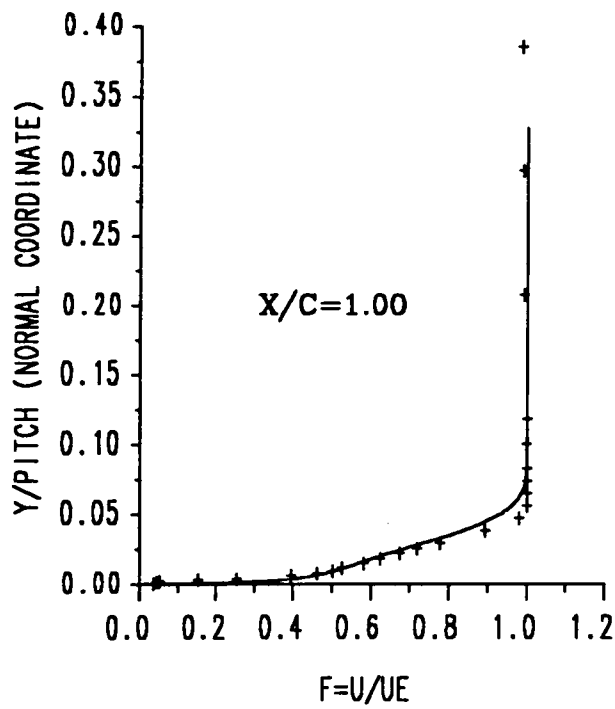


CASE	—	CURRENT ANALYSIS	+++	TEST DATA (REF. 68)
------	---	------------------	-----	---------------------

FIGURE 58 SUPERCritical CASCADE BUILD 1 TURBULENT VELOCITY PROFILE

SUCTION SURFACE

MACH NUMBER=0.098

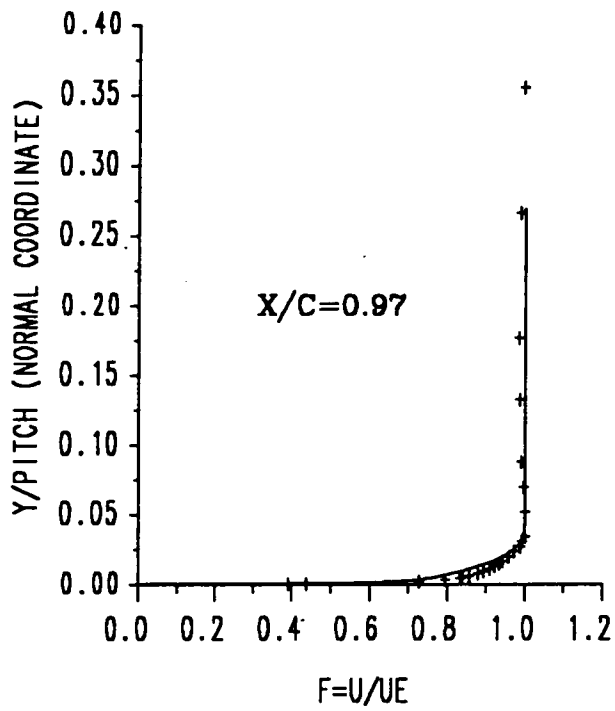


CASE — CURRENT ANALYSIS + + + TEST DATA (REF. 68)

FIGURE 59 SUPERCRITICAL CASCADE BUILD 1 TURBULENT VELOCITY PROFILE

PRESSURE SURFACE

MACH NUMBER=0.095

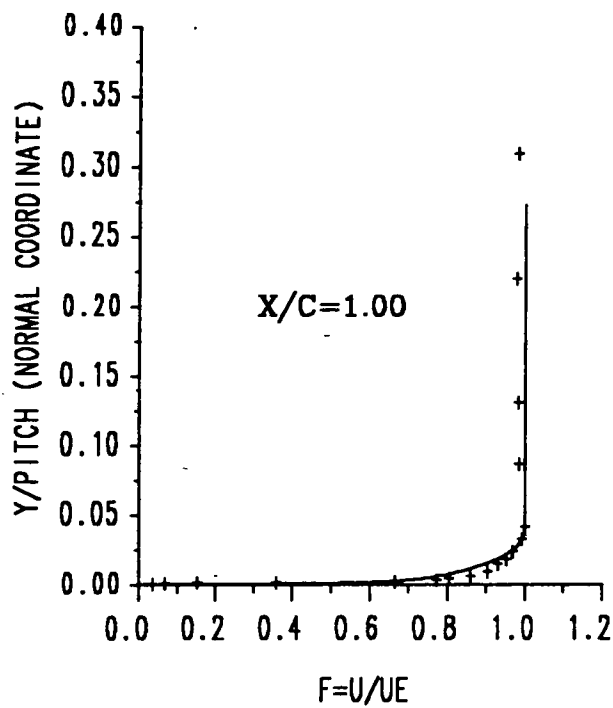


CASE	—	CURRENT ANALYSIS	+	+	+	TEST DATA (REF. 68)
------	---	------------------	---	---	---	---------------------

FIGURE 60 SUPERCRITICAL CASCADE BUILD 1 TURBULENT VELOCITY PROFILE

PRESSURE SURFACE

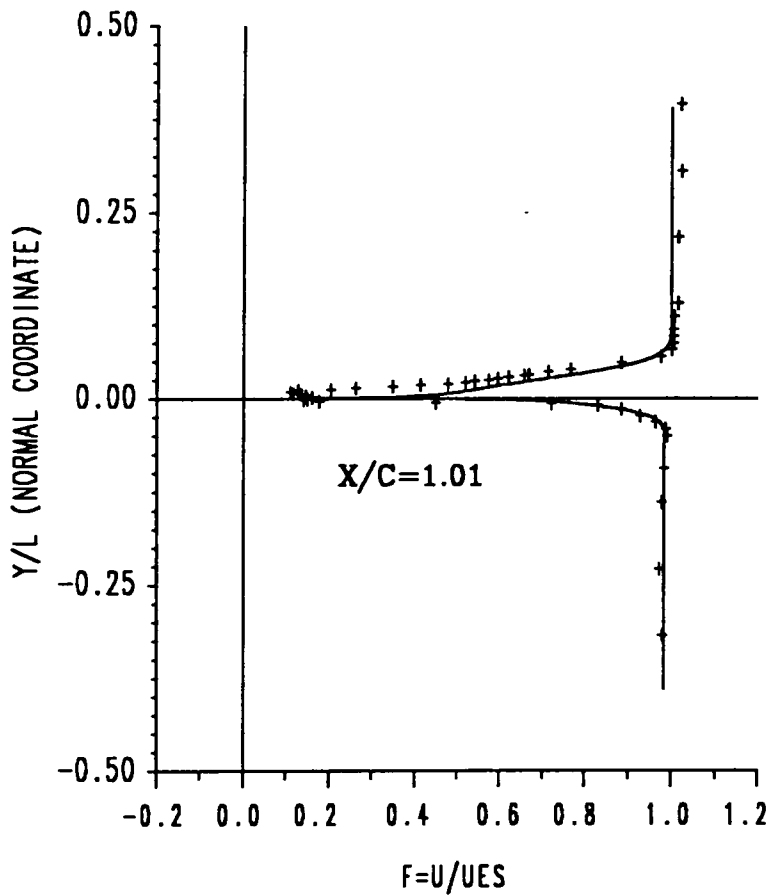
MACH NUMBER=0.097



CASE	—	CURRENT ANALYSIS	+	+	+	TEST DATA (REF. 68)
------	---	------------------	---	---	---	---------------------

FIGURE 61 SUPERCRITICAL CASCADE BUILD 1 TURBULENT VELOCITY PROFILE

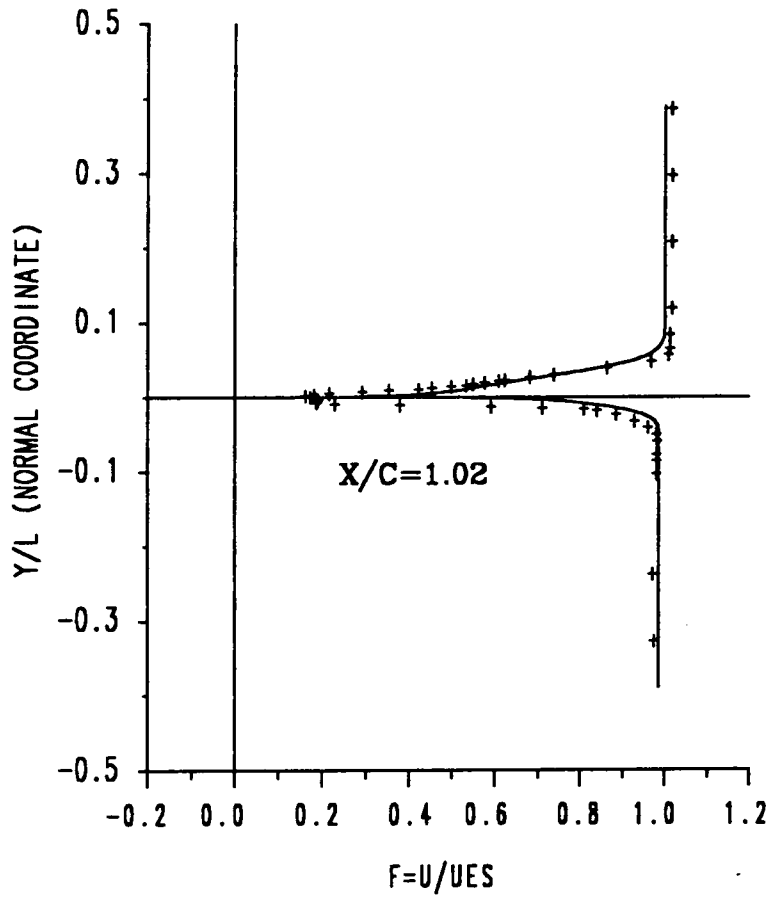
SUCTION SURFACE MACH NUMBER=0.098
PRESSURE SURFACE MACH NUMBER=0.098



CASE	—	CURRENT ANALYSIS	+++	TEST DATA (REF. 68)
------	---	------------------	-----	---------------------

FIGURE 62 SUPERCritical CASCADE BUILD 1 TURBULENT WAKE PROFILE

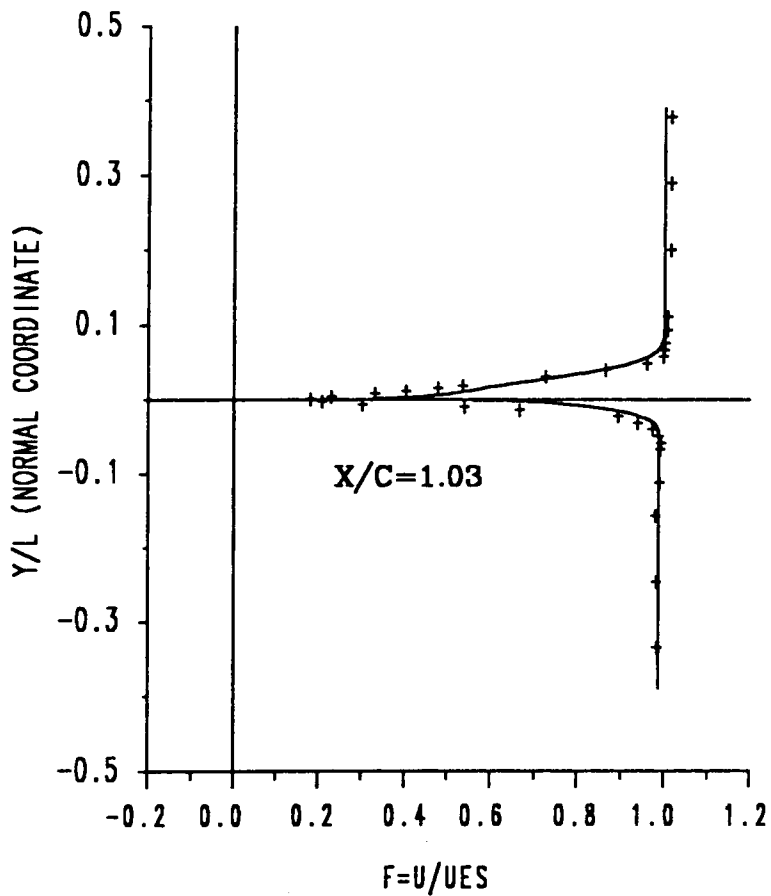
SUCTION SURFACE WACH NUMBER=0.097
PRESSURE SURFACE WACH NUMBER=0.096



CASE — CURRENT ANALYSIS + + + TEST DATA (REF. 68)

FIGURE 63 SUPERCRITICAL CASCADE BUILD 1 TURBULENT WAKE PROFILE

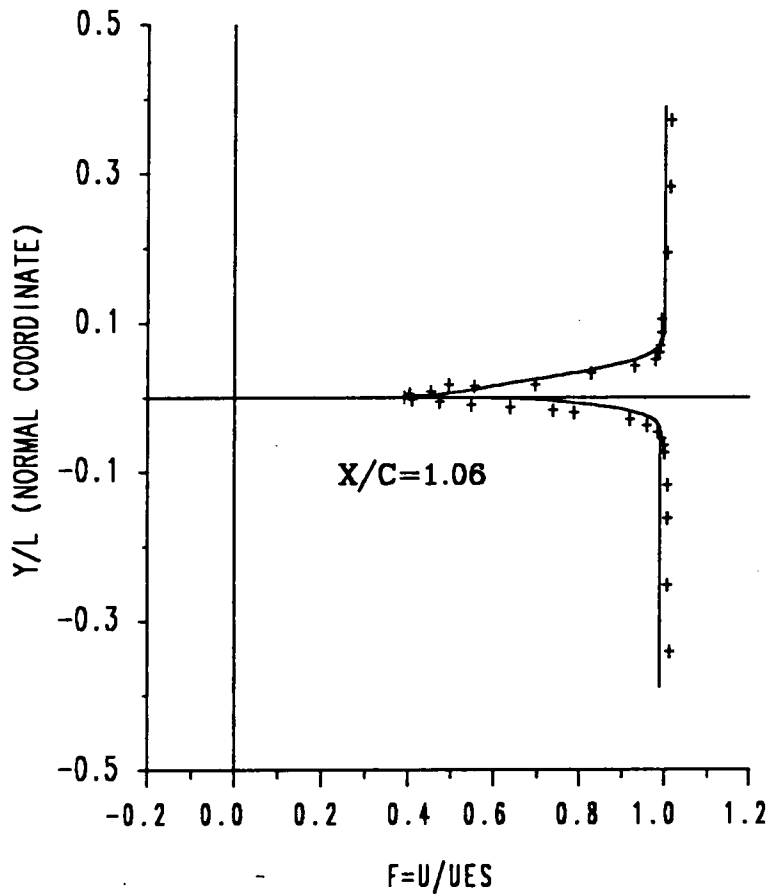
SUCTION SURFACE MACH NUMBER=0.097
 PRESSURE SURFACE MACH NUMBER=0.096



CASE	—	CURRENT ANALYSIS	+++	TEST DATA (REF. 68)
------	---	------------------	-----	---------------------

FIGURE 64 SUPERCritical CASCADE BUILD 1 TURBULENT WAKE PROFILE

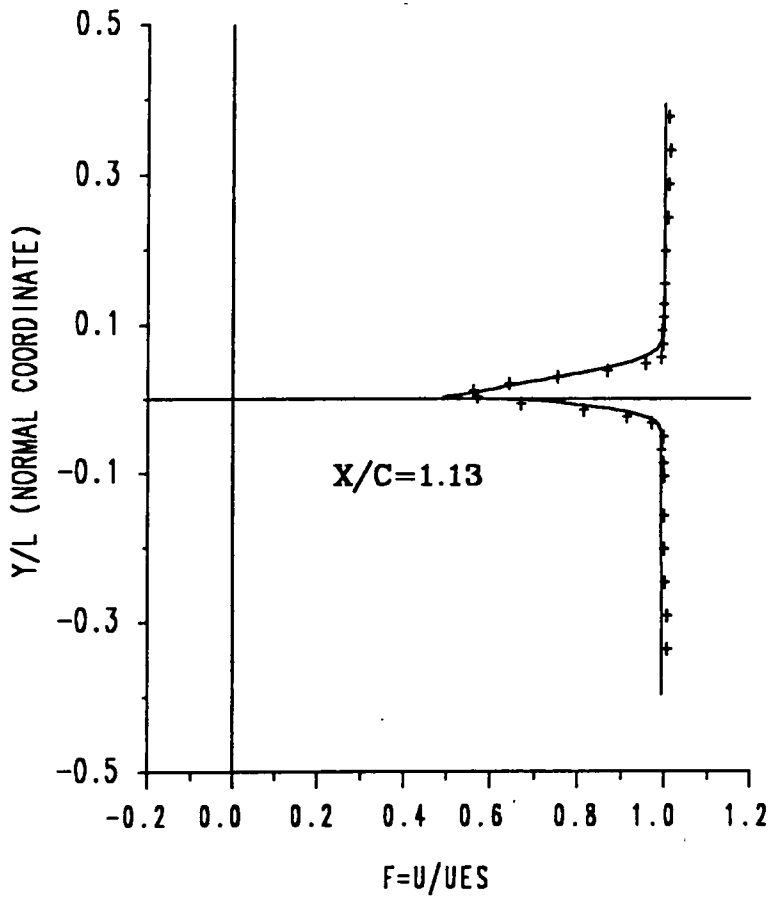
SUCTION SURFACE MACH NUMBER=0.097
PRESSURE SURFACE MACH NUMBER=0.096



CASE — CURRENT ANALYSIS + + + TEST DATA (REF. 68)

FIGURE 65 SUPERCRITICAL CASCADE BUILD 1 TURBULENT WAKE PROFILE

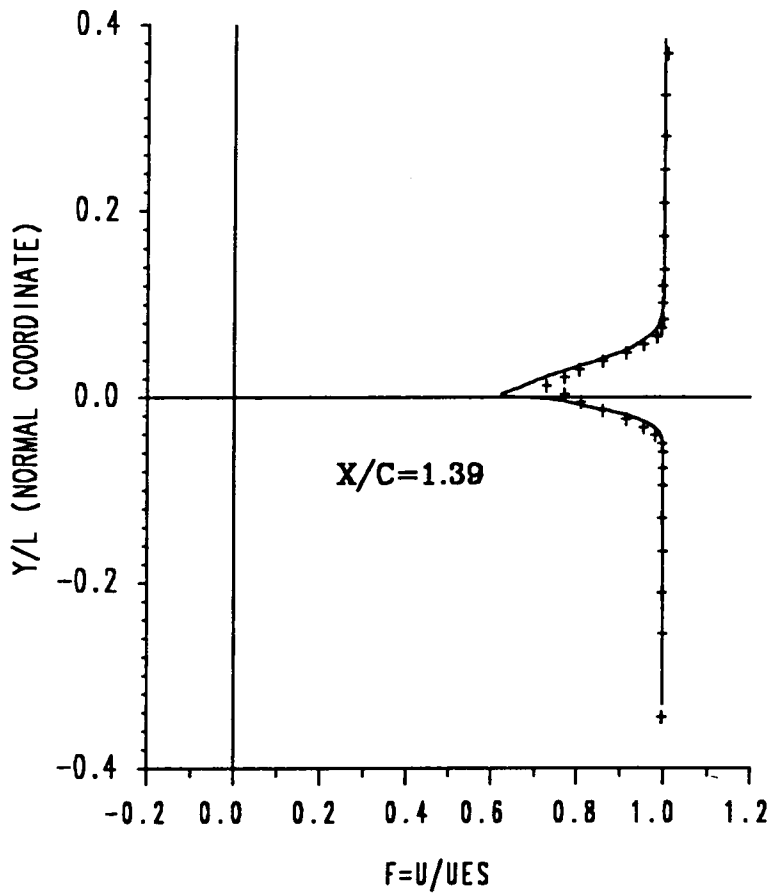
SUCTION SURFACE MACH NUMBER=0.097
PRESSURE SURFACE MACH NUMBER=0.096



CASE — CURRENT ANALYSIS + + + TEST DATA (REF. 68)

FIGURE 66 SUPERCRITICAL CASCADE BUILD 1 TURBULENT WAKE PROFILE

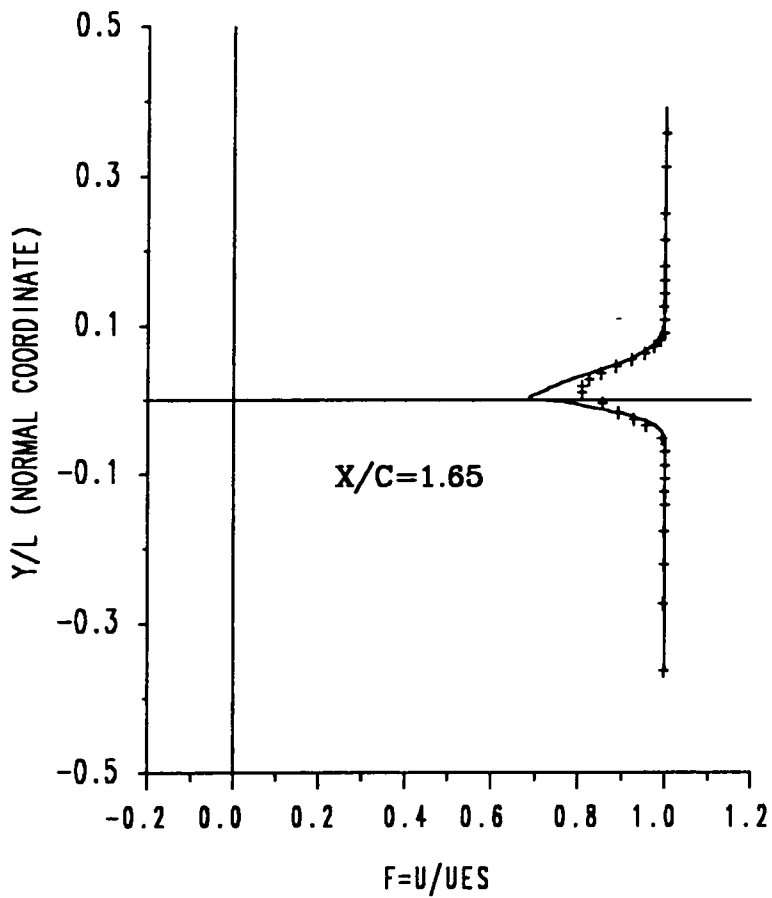
SUCTION SURFACE MACH NUMBER=0.096
PRESSURE SURFACE MACH NUMBER=0.096



CASE	—	CURRENT ANALYSIS	+++	TEST DATA (REF. 68)
------	---	------------------	-----	---------------------

FIGURE 67 SUPERCritical CASCADE BUILD 1 TURBULENT WAKE PROFILE

SUCTION SURFACE MACH NUMBER=0.096
PRESSURE SURFACE MACH NUMBER=0.096



CASE	——	CURRENT ANALYSIS	+++	TEST DATA (REF. 68)
------	----	------------------	-----	---------------------

FIGURE 68 SUPERCritical CASCADE BUILD 1 TURBULENT WAKE PROFILE

CASCADE DATA

GAP/CHORD=0.600
STAGGER ANGLE=20.8

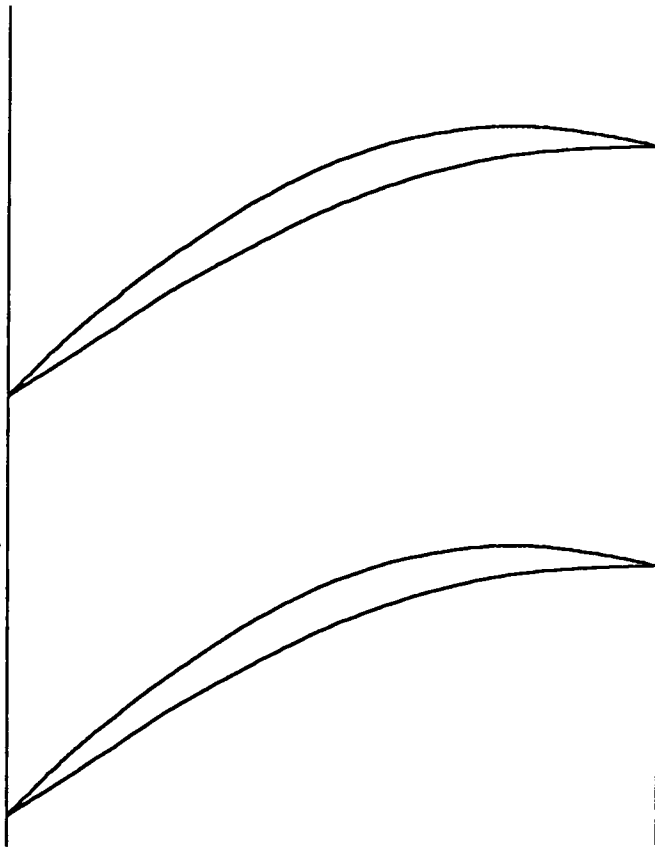


FIGURE 69 SUPERCRITICAL CASCADE BUILD 2

SUCTION SURFACE
EXPERIMENTAL DATA

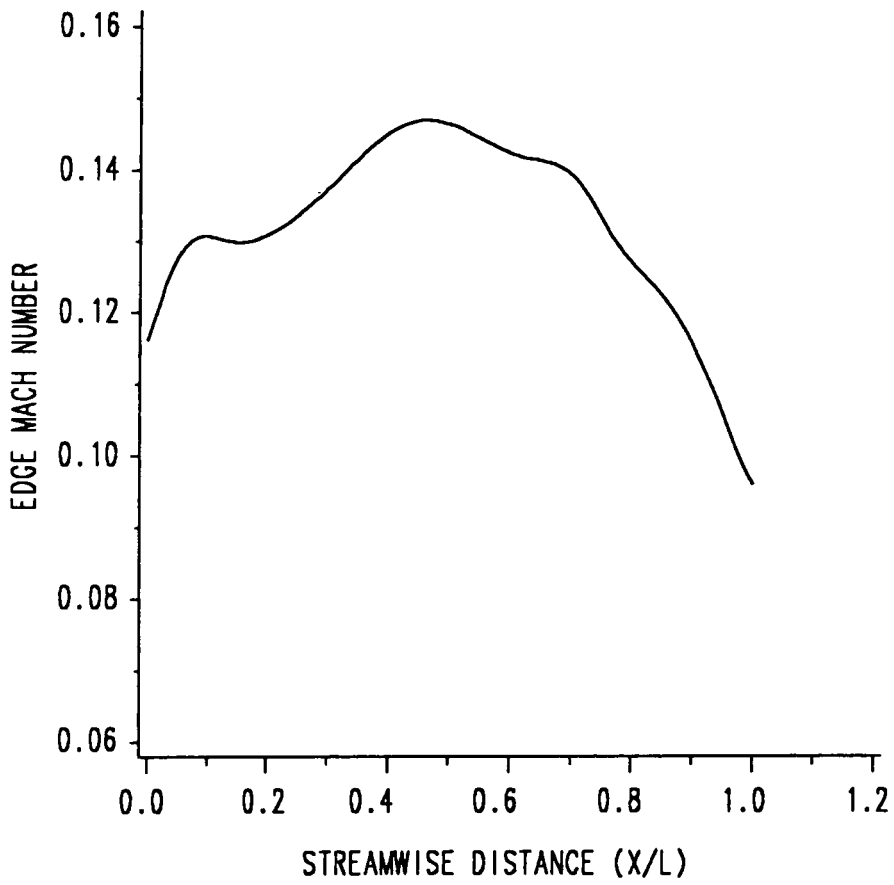


FIGURE 70 SUPERCritical CASCADE BUILD 2 EDGE MACH NUMBER

PRESSURE SURFACE
EXPERIMENTAL DATA

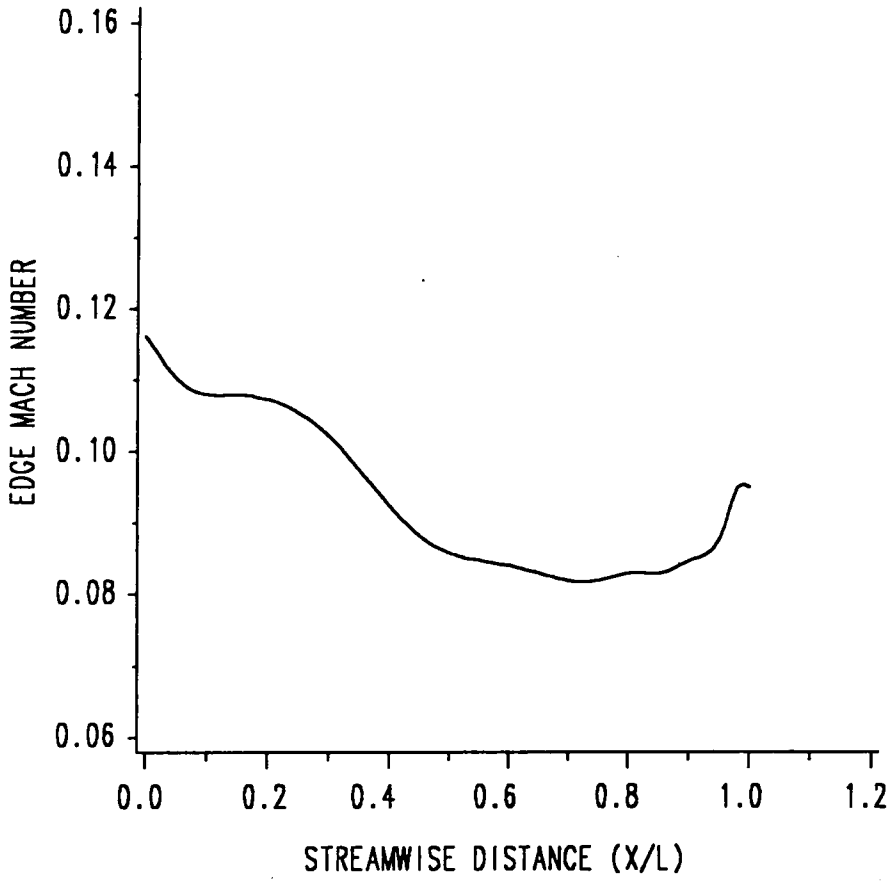
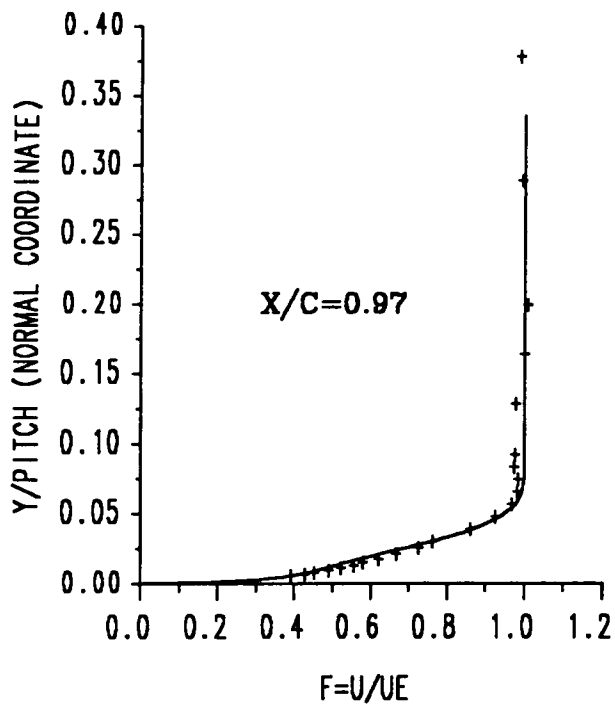


FIGURE 71 SUPERCRITICAL CASCADE BUILD 2 EDGE MACH NUMBER

SUCTION SURFACE

MACH NUMBER=0.102

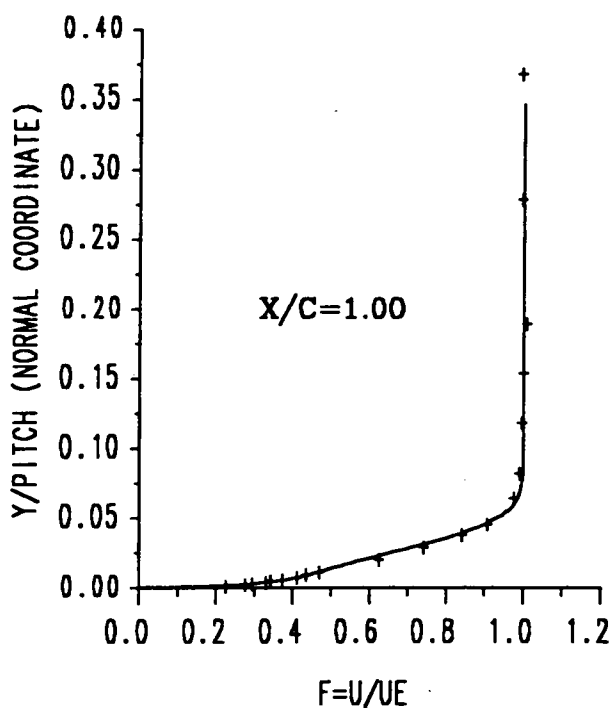


CASE ——— CURRENT ANALYSIS + + + TEST DATA (REF. 68)

FIGURE 72 SUPERCritical CASCADE BUILD 2 TURBULENT VELOCITY PROFILE

SUCTION SURFACE

MACH NUMBER=0.100

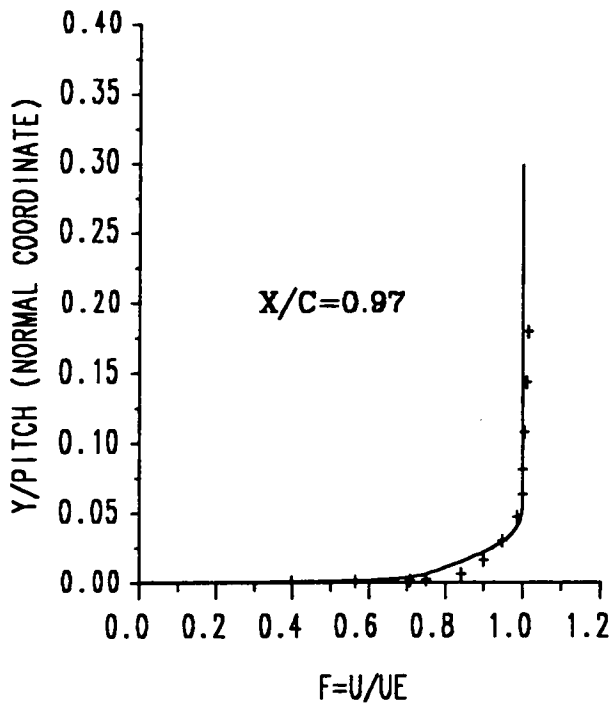


CASE ——— CURRENT ANALYSIS + + + TEST DATA (REF. 68)

FIGURE 73 SUPERCRITICAL CASCADE BUILD 2 TURBULENT VELOCITY PROFILE

PRESSURE SURFACE

MACH NUMBER=0.095

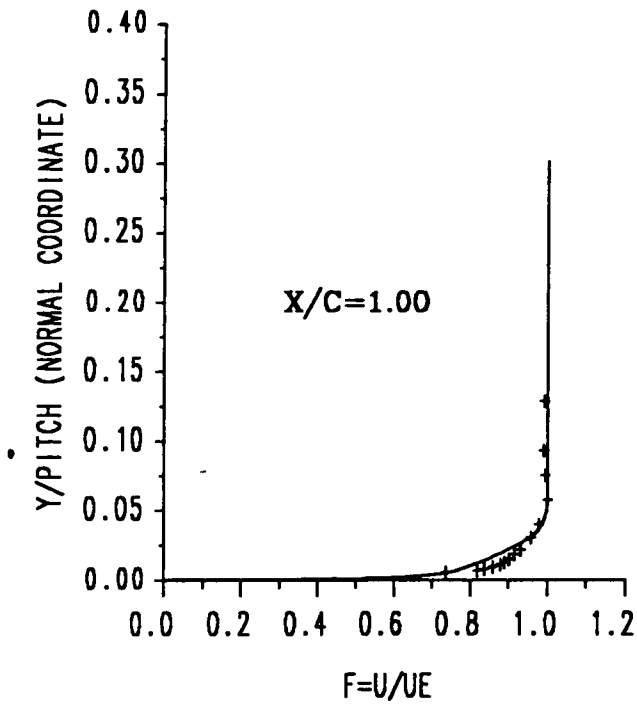


CASE ——— CURRENT ANALYSIS + + + TEST DATA (REF. 68)

FIGURE 74 SUPERCRITICAL CASCADE BUILD 2 TURBULENT VELOCITY PROFILE

PRESSURE SURFACE

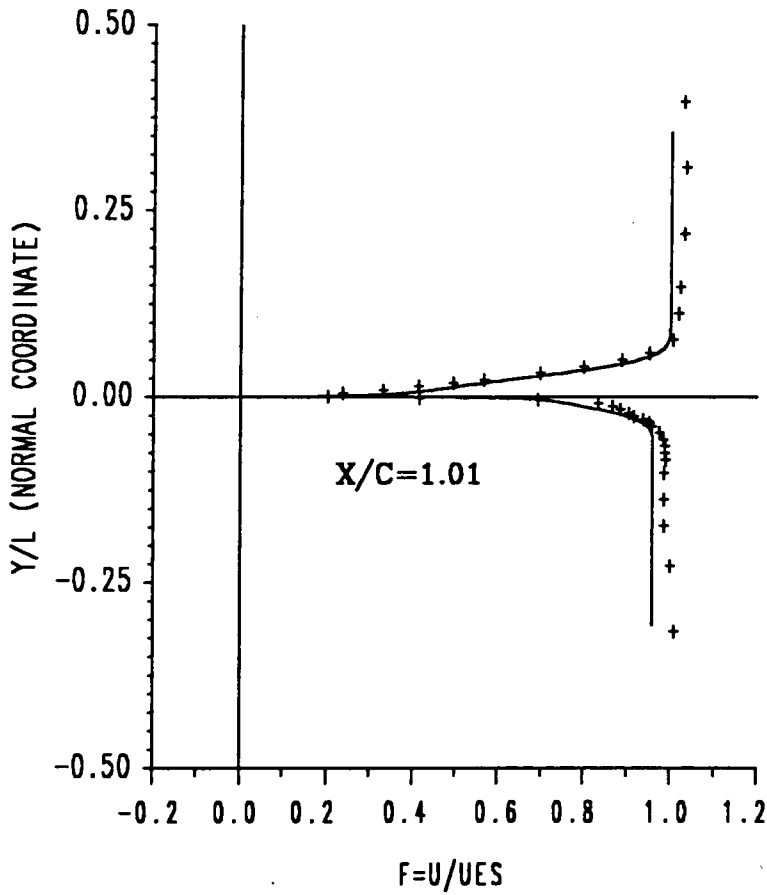
MACH NUMBER=0.095



CASE	—	CURRENT ANALYSIS	+	+	+	TEST DATA (REF. 68)
------	---	------------------	---	---	---	---------------------

FIGURE 75 SUPERCRITICAL CASCADE BUILD 2 TURBULENT VELOCITY PROFILE

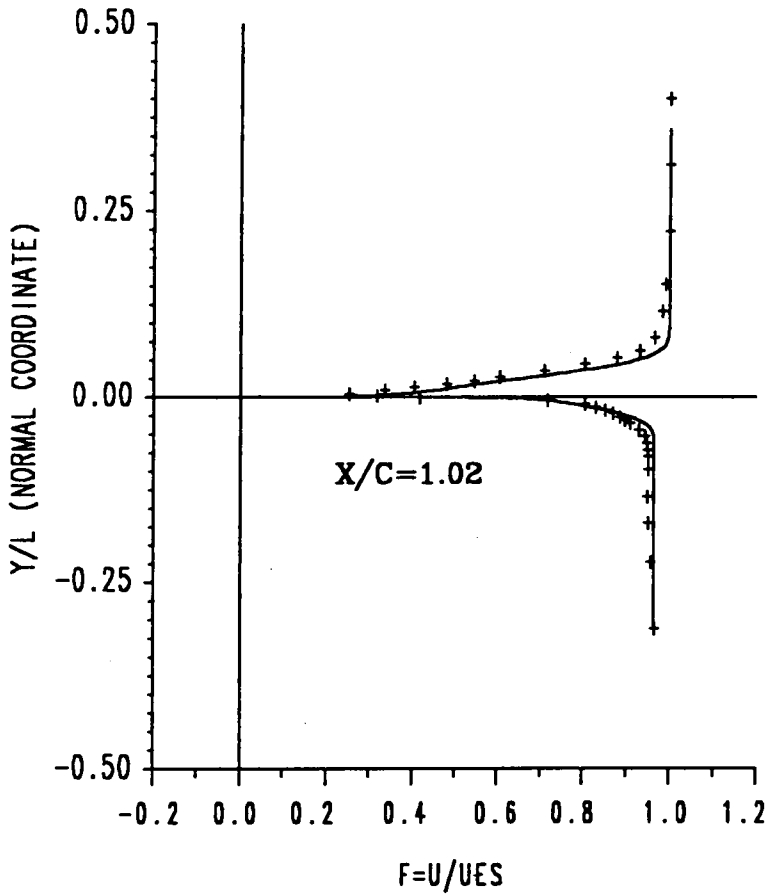
SUCTION SURFACE MACH NUMBER=0.099
PRESSURE SURFACE MACH NUMBER=0.095



CASE ——— CURRENT ANALYSIS + + + TEST DATA (REF. 68)

FIGURE 76 SUPERCritical CASCADE BUILD 2 TURBULENT WAKE PROFILE

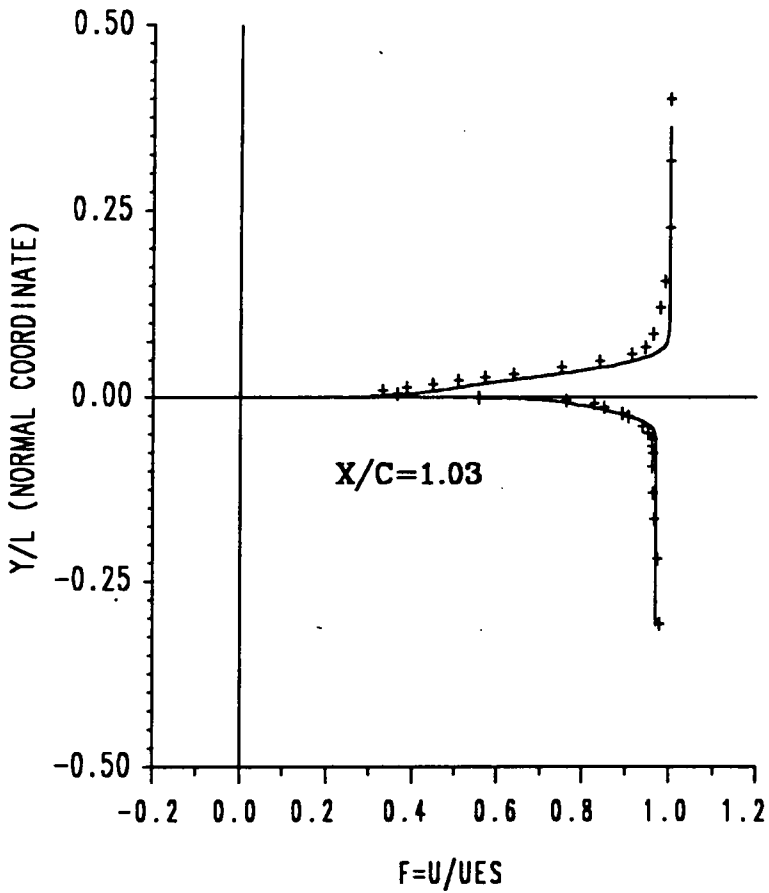
SUCTION SURFACE MACH NUMBER=0.098
PRESSURE SURFACE MACH NUMBER=0.098



CASE ——— CURRENT ANALYSIS + + + TEST DATA (REF. 68)

FIGURE 77 SUPERCritical CASCADE BUILD 2 TURBULENT WAKE PROFILE

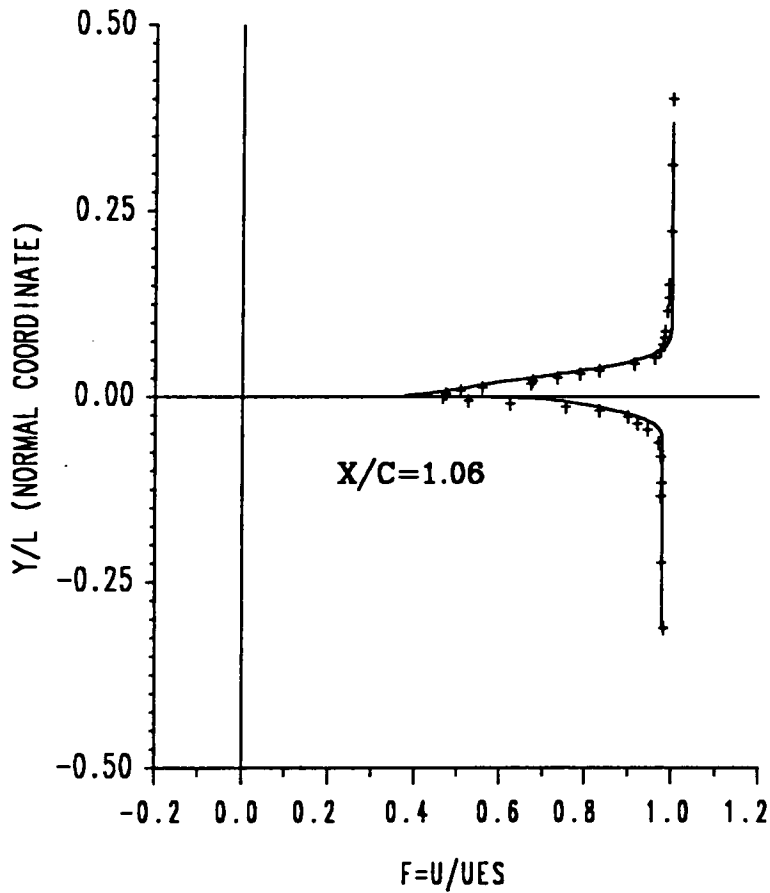
SUCTION SURFACE MACH NUMBER=0.098
PRESSURE SURFACE MACH NUMBER=0.095



CASE	—	CURRENT ANALYSIS	+++	TEST DATA (REF. 68)
------	---	------------------	-----	---------------------

FIGURE 78 SUPERCritical CASCADE BUILD 2 TURBULENT WAKE PROFILE

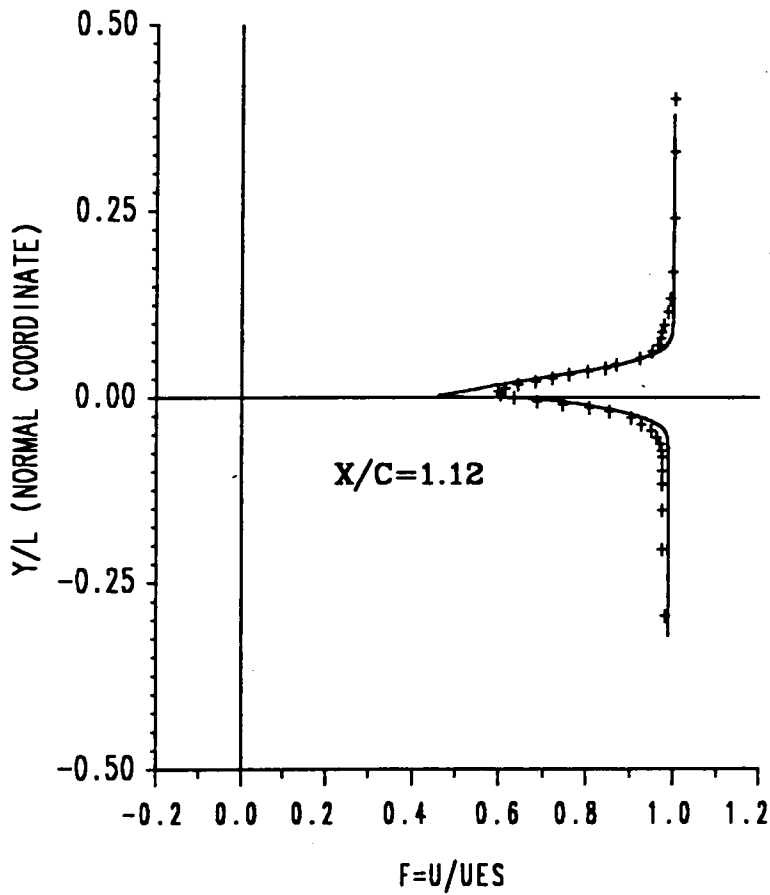
SUCTION SURFACE MACH NUMBER=0.098
PRESSURE SURFACE MACH NUMBER=0.096



CASE ——— CURRENT ANALYSIS + + + TEST DATA (REF. 68)

FIGURE 79 SUPERCRITICAL CASCADE BUILD 2 TURBULENT WAKE PROFILE

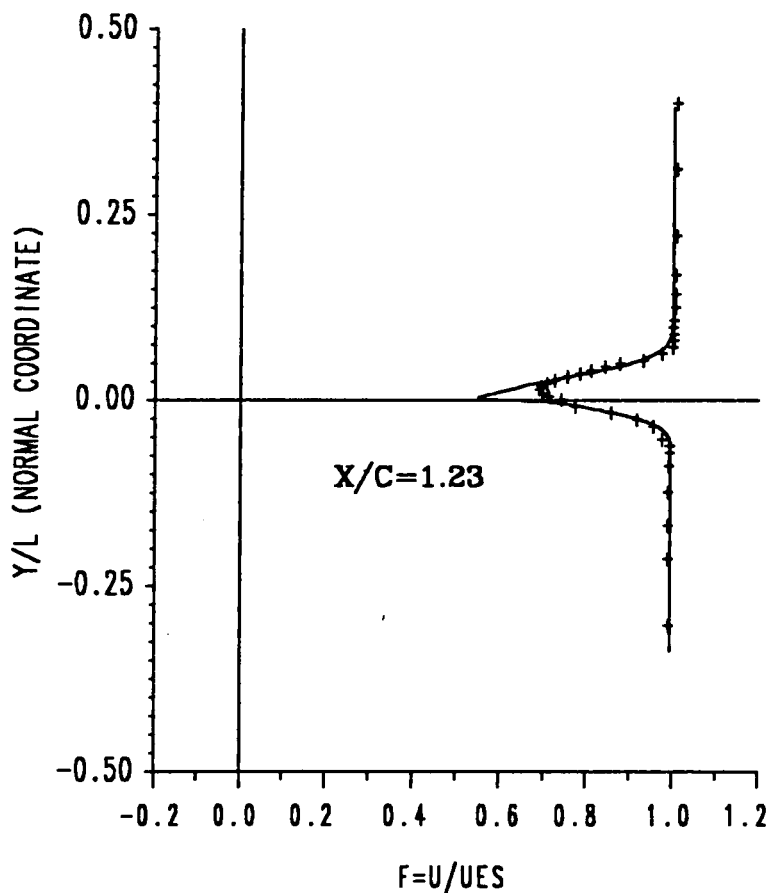
SUCTION SURFACE MACH NUMBER=0.097
PRESSURE SURFACE MACH NUMBER=0.096



CASE ——— CURRENT ANALYSIS + + + TEST DATA (REF. 68)

FIGURE 80 SUPERCRITICAL CASCADE BUILD 2 TURBULENT WAKE PROFILE

SUCTION SURFACE MACH NUMBER=0.096
PRESSURE SURFACE MACH NUMBER=0.096



CASE	—	CURRENT ANALYSIS	+++	TEST DATA (REF. 68)
------	---	------------------	-----	---------------------

FIGURE 81 SUPERCritical CASCADE BUILD 2 TURBULENT WAKE PROFILE

APPENDIX I
Solution of Block Tridiagonal Set of Equations

For the inviscid flow solver, a block tridiagonal set of equations was presented in Chapter 2 as

At $i = 1$

$$\bar{B}_1 \Delta\bar{\phi}_1 + \bar{C}_1 \Delta\bar{\phi}_2 = \bar{d}_1 \quad (2.19)$$

For $i = 2$ to $NGX - 1$

$$\bar{A}_i \Delta\bar{\phi}_{i-1} + \bar{B}_i \Delta\bar{\phi}_i + \bar{C}_i \Delta\bar{\phi}_{i+1} = \bar{d}_i \quad (2.20)$$

$i = NGX$

$$\bar{A}_i \Delta\bar{\phi}_{i-1} + \bar{B}_i \Delta\bar{\phi}_i = \bar{d}_i \quad (2.21)$$

The solution of this set of equations is accomplished by a method presented by Swift [42] as follows;

From Eq. (2.19)

$$\Delta\bar{\phi}_1 = \bar{A}_1^{-1} [\bar{d}_1 - \bar{C}_1 \Delta\bar{\phi}_2] \quad (A.1)$$

At $i = 2$

$$\bar{A}_2 \Delta\bar{\phi}_1 + \bar{B}_2 \Delta\bar{\phi}_2 + \bar{C}_2 \Delta\bar{\phi}_3 = \bar{d}_2 \quad (A.2)$$

Combining Eqs. (A.1) and (A.2) gives

$$\Delta \bar{\phi}_2 = [\bar{B}_2 - \bar{A}_2 \bar{B}_1^{-1} \bar{C}_1^{-1} \{[\bar{d}_2 - \bar{A}_2 \bar{B}_1^{-1} \bar{d}_1 - \bar{C}_2 \bar{\Delta} \phi_3]\} \quad (\text{A.3})$$

If this process is carried out for each row of submatrices in M where

$$\bar{M} \Delta \bar{\phi} = \bar{L}$$

is a description of Eqs. (2.19) through (2.21), the the following set of recurrence formulae arise.

$$\bar{H}_1 = \bar{A}_1$$

$$\bar{H}_2 = \bar{B}_2 - \bar{A}_2 \bar{H}_1^{-1} \bar{C}_1 \quad (\text{A.4})$$

$$\bar{H}_n = \bar{B}_n - \bar{A}_n \bar{H}_{n-1}^{-1} \bar{C}_{n-1}$$

and

$$\bar{Q}_1 = \bar{A}_2 \bar{H}_1^{-1} \bar{d}_1$$

$$\bar{Q}_2 = \bar{A}_3 \bar{H}_2^{-1} [\bar{d}_2 - \bar{Q}_1] \quad (\text{A.5})$$

$$\bar{Q}_n = \bar{A}_{n+1} \bar{H}_n^{-1} [\bar{d}_n - \bar{Q}_{n-1}]$$

The formulae for the back substitution are as follows. Starting at the grid line

$$i = \text{NGX}$$

$$\Delta \bar{\phi}_{\text{NGX}} = \bar{H}_{\text{NGX}}^{-1} [\bar{d}_{\text{NGX}} - \bar{Q}_{\text{NGX-1}}^{\sim}]$$

$$\Delta \bar{\phi}_{\text{NGX-1}} = \bar{H}_{\text{NGX-1}}^{-1} [\bar{d}_{\text{NGX-1}} - \bar{Q}_{\text{NGX-2}}^{\sim}]$$

$$- \bar{C}_{\text{NGX-1}} \Delta \bar{\phi}_{\text{NGX}}^{\sim} \tag{A.6}$$

$$\Delta \bar{\phi}_n = \bar{H}_n^{-1} [\bar{d}_n - \bar{Q}_{n-1} - \bar{C}_n \Delta \bar{\phi}_{n+1}^{\sim}]$$

$$\Delta \bar{\phi}_1 = \bar{H}_1^{-1} [\bar{d}_1 - \bar{C}_1 \Delta \bar{\phi}_2^{\sim}]$$

**The vita has been removed from
the scanned document**